ELECTRICAL CONDUCTION ALONG DISLOCATIONS IN SILICON AND ITS EFFECT ON MIS SOLAR CELLS

by

Weerawanni Mudiyanselage Ranjith Divigalpitiya

B.Sc. (Hon.) University of Sri Lanka, Vidyodaya Campus, 1978

M.Sc. Simon Fraser University, 1982

THESIS SUBMITTED IN PARTIAL FULFILLMENT OF

THE REQUIREMENTS FOR THE DEGREE OF

DOCTOR OF PHILOSOPHY

in the Department

of

Physics

SIMON FRASER UNIVERSITY

DECEMBER, 1986

APPROVAL

Name: Weerawanni Mudiyanselage Ranjith Divigalpitiya

Degree: Doctor of Philosophy

Titile of Thesis: Electrical conduction along dislocations in silicon and its effect on MIS solar cells

Examining Committee:

Chairperson: D.H. Boal

S.R. Morrison
Senior Supervisor

R.F. Frindt

R.H. Enns

M.L.W. Thewalt

K. Colbow

D.L. Pulfrey
External Examiner
Professor
Department of Electrical Engineering
University of British Columbia

Date Approved: January 16, 1987

PARTIAL COPYRIGHT LICENSE

I hereby grant to Simon Fraser University the right to lend my thesis, project or extended essay (the title of which is shown below) to users of the Simon Fraser University Library, and to make partial or single copies only for such users or in response to a request from the library of any other university, or other educational institution, on its own behalf or for one of its users. I further agree that permission for multiple copying of this work for scholarly purposes may be granted by me or the Dean of Graduate Studies. It is understood that copying or publication of this work for financial gain shall not be allowed without my written permission.

Title of Thesis/Project/Extended Essay

Electrical Conduction along Dislocations in Silicon and its Effect on MIS Solar Cells

Author: _____
(signature)

W.M.R. Divigalpitiya
(name)

26 March 87
(date)

ABSTRACT

The current-voltage (J-V) characteristics were measured for a series of metal-insulator-semiconductor (MIS) cells of Al-SiO_x-pSi structure with dislocation loops penetrating different depths into the semiconductor surface. All cell parameters except reverse saturation photocurrent were observed to be degraded with increasing dislocation length. The reverse saturation photocurrent is independent of the extent of damage in the samples. The experimental results are explained in terms of a mathematical model based on conduction of captured carriers along dislocations. The specific conductance of the dislocations studied was found to be in the order of 10^{-15} cm ohm^{-1}. To the first approximation, the bias dependence of the current along a dislocation was shown to be $\exp(qV_o/2kT)$ contrary to the general expectation that such a current is linear in the voltage V_o. To our knowledge, this is the first time that conduction along dislocations has been observed at room temperature.

The photoelectrochemical studies done elsewhere on the same samples lend strong support to the hypothesis of conduction along dislocations.

The effect of atomic hydrogen passivation of dislocations was also studied. Upon passivation, all the solar cell characteristics improve in general.

Occasionally, however, anomalous J-V characteristics were observed indicating the possibility of acceptor neutralization. This complicates the interpretation of the experimental results in terms of the dislocation conductivity model.

The temperature dependence of the solar cell characteristics in the range of 100 to 300 K was studied. Temperature coefficients of open circuit voltage, short circuit current, fill factor and efficiency of the MIS structure closely resemble those of n^+p silicon solar cells indicating the electronic equivalence of Al-SiO_x-pSi structure to an abrupt one sided n^+p junction.

The MIS solar cell characteristics were found to be sensitive to humidity. Possible oxidation of CO at the silicon surface in the presence of a plasma was also observed. Neither of these phenomena was studied in depth.

Dedicated to my dear parents.

ACKNOWLEDGEMENTS

My deepest gratitude and sincere thanks are due to Prof. S.R. Morrison, my senior supervisor, for sparing his valuable time to encourage and guide me in carrying out this study in spite of his busy schedule as the Director of the Energy Research Institute at S.F.U.

Prof. W.P. Gomes and his coworkers at the Physical Chemistry Laboratory, University of Gent, Belgium are specially thanked for conducting the electrochemical measurements of my samples.

All the colleagues in the ERI, specially, Bill Sears, Per Joensen and Bijan Miremadi are gratefully acknowledged for their kind assistance at various instances during the study.

I wish to thank the members of the supervisory committee Profs. R.F. Frindt, M.L.W. Thewalt, R.H. Enns, and K. Colbow. The external examiner Prof. D.L. Pulfrey of U.B.C is also gratefully acknowledged.

The assistance of Bob Anglim at Microtel Pacific Research at Discovery Park in Burnaby in carrying out the ellipsometric measurements is thankfully acknowledged. I thank Onkar Rajora for obtaining the SEM micrographs. The technical staff of the Physics Department, the machine shop and the electronics shop are gratefully acknowledged for the help they gave me on numerous occasions, specially,

Siva Chinniah for his moral support as well.

The financial support from my supervisor through a research grant from the Natural Sciences and Engineering Research Council of Canada, the scholarships, President's stipend and the teaching assistantships from S.F.U are also gratefully acknowledged.

Finally, I wish to thank my wife, Kanthi, for the unfailing support she gave me throughout the study, and specially for conducting the SAM/AES surveys of the samples and helping me in the preparation of the diagrams.

TABLE OF CONTENTS

APPROVAL II

ABSTRACT III

DEDICATION V

ACKNOWLEDGEMENTS VI

TABLE OF CONTENTS VIII

LIST OF TABLES XI

LIST OF FIGURES XII

CHAPTER I INTRODUCTION 1

1.1 Dislocations 1

1.2 Objective of this thesis 6

1.3 Organization 7

CHAPTER II REVIEW OF DISLOCATIONS AND MIS SOLAR CELLS 12

2.1 Physics of dislocations 12

2.1.1 Half Filled Band (HFB) model 13

2.1.2 Dislocation conductivity 15

2.2 Grain boundary studies 17

2.3 Effect of dislocations on devices 19

2.4 The MIS solar cell 21

2.4.1 Current-voltage characteristics 23

2.4.2 The capacitance of the MIS structure 28

CHAPTER III EXPERIMENTAL 42

3.1 Generation of dislocations 42

3.1.1 The depth of damage 43

3.1.2 Determination of depth of damage 44

3.1.3 Experimental 44

3.2 Sample preparation 46

3.2.1 The insulator and its thickness measurement 46

3.2.2 Ellipsometry: theory 47

3.2.3 Thickness measurement 49

3.2.4 Metal evaporation 49

3.2.5 The MIS fabrication 51

3.3 I-V, C-V measurement 52

3.3.1 Theory 52

3.3.2 Experimental 54

3.3.3 Light source and sample holder 55

3.4 Hydrogen passivation 56

3.4.1 Experimental 57

CHAPTER IV RESULTS AND ANALYSIS 67

4.1 MIS cell characteristics 67

4.1.1 Use of HF for etching 67

4.1.2 Oxidation time 68

4.1.3 General cell characteristics 69

4.1.4 Damaged samples 71

4.2 Density of dislocations 73

4.3 Analysis and model 73

4.3.1 Recombination model 74

4.3.2 Dislocation conductivity model 76

4.3.3 Results and discussion 84

4.5 Conclusions 90

CHAPTER V FURTHER STUDIES OF DISLOCATIONS 125

5.1 Photoelectrochemical data 125

5.1.1 Discussion 129

5.1.2 Conclusions 131

5.2 Hydrogen passivation of dislocations 132

5.2.1 Model 133

5.2.2 Results and discussion 136

5.2.3 Conclusions 140

CHAPTER VI TEMPERATURE DEPENDENCE OF CELL PARAMETERS 155

6.1 MIS structure as an n^+p junction 155

6.1.1 Results and discussion 155

6.2 Effect of temperature on damaged cells 159

6.3 Sensitivity of MIS to humidity 161

6.4 Passivation in the presence of CO 162

6.5 Conclusions 163

CHAPTER VII CONCLUSIONS 175

APPENDIX 1 177

BIBLIOGRAPHY 182

LIST OF TABLES

TABLE		PAGE
4-1	The change in cell parameters with oxidation	96
4-2	Parameters of undamaged and damaged solar cells	103
4-3	Parameters used in calculations	114
6-1	Diode parameters of Al-SiO_x-pSi cells	165
6-2	Temperature coefficients of n-p and MIS cells	167

LIST OF FIGURES

FIGURE		PAGE
1-1a	A pure edge dislocation	8
1-1b	A pure screw dislocation	8
1-2	A part of a dislocation loop with both edge and screw components	9
1-3	Burgers vectors and Burgers circuits	10
1-4	Diamond structure and an edge dislocation therein	11
2-1a	The line charge and cylindrical space charge region of a dislocation	32
2-1b	The potential near a dislocation	32
2-2	The half filled band model	33
2-3	The variation of mobility of deformed and undeformed Ge	34
2-4	The results of Osip'yan's experiment	35
2-5	The band diagram of p-type polysilicon showing the relative positions of the redox couples	36
2-6	Reverse bias I-V curves for p-type poly Si with and without $Fe^{III}EDTA$ in solution	37
2-7	The structure of MIS solar cell	38
2-8	The band diagram for an Al-SiO_x-pSi structure	39
2-9	The current-voltage characteristics of a solar cell	40
2-10	The equivalent circuit for an MIS structure	41
3-1	Surface dislocation loops	58
3-2	Determination of the depth of damage	58

3-3	Formation of an etch pit at a dislocation	59
3-4a	The change in polarization after reflection	60
3-4b	Schematic of the rotating analyzer ellipsometer	60
3-5	Schematic of the vacuum evaporator and the rotatable mask holder	61
3-6a	Schematic of the electrical circuit used for measuring I-V and C-V of MIS samples	62
3-6b	Measurement of capacitance with constant Va.c.	63
3-7	The spectral distribution of Oriel light source	64
3-8	Schematic of the system used for measuring the dark and illuminated characteristics of MIS cells	64
3-9	Schematic of the cryostat	65
3-10	Schematic of the passivation apparatus	66
4-1a	Auger survey spectrum on an unstained Si	92
4-1b	Auger survey spectrum on a stained area of Si	93
4-2a	J-V curves of samples where planar etch was used	94
4-2b	J-V curves of samples where 10% HF was used	95
4-3a	J-V characteristics of an MIS solar cell	97
4-3b	The top view of the MIS cell	98
4-4a	The variation of short circuit current density with illumination intensity	99
4-4b	The variation of cell parameters with illumination or short circuit current density	100
4-5	Mott-Schottky plot of an MIS cell	101
4-6a	Illuminated J-V characteristics of cells damaged with alumina powder of various grit sizes	102
4-6b	The net photocurrent density of MIS cells of various damage sizes vs. reverse bias	104

4-7 J-V curves of a 1 μm damaged cell after successively etching it several times 105

4-8a SEM photo of a damaged sample after a 20s etch 106

4-8b SEM photo of a damaged sample after a 1 min etch 107

4-9 Calculated J-V curves using recombination theory 108

4-10a The MIS structure with mechanical damage (model) 109

4-10b The band diagram of the cell with the dislocation in the plane of the paper 110

4-10c The cross-sectional view of the band diagram perpendicular to the surface of the cell 111

4-11a Calculated variation of the current along dislocation with its length: $s = 1 \times 10^{-15}$ cm ohm^{-1} and $E_i - \mu = 0.3$ eV 112

4-11b Calculated variation of the current along dislocation with its length: $s = 1 \times 10^{-15}$ cm ohm^{-1} and $E_i - \mu = 0.5$ eV 113

4-12a Effect of specific conductance on J-V characteristics of a 1 μm damaged cell: $E_i - \mu = 0.3$ eV 115

4-12b Effect of specific conductance on J-V characteristics of a 1 μm damaged cell: $E_i - \mu = 0.5$ eV 116

4-13a Variation of the total J-V of the MIS cell with the length of dislocation when $E_i - \mu = 0.3$ eV 117

4-13b Variation of the total J-V of the MIS cell with the length of dislocation when $E_i - \mu = 0.5$ eV 118

4-14a Variation of the total J-V of 1 μm damaged MIS cell with specific conductance when $E_i - \mu = 0.3$ eV 119

4-14b Variation of the total J-V of 1 μm damaged MIS cell with specific conductance when $E_i - \mu = 0.5$ eV 120

4-15a Variation of short circuit current density and efficiency with length of dislocations: theory and experimental data 121

4-15b Variation of fill factor and open circuit voltage with length of dislocations: theory and experimental data 122

4-16a Calculated variation of short circuit current density and efficiency with density of dislocations 123

4-16b Calculated variation of fill factor and open circuit voltage with density of dislocations 124

5-1 Scanning Laser Spot maps at two different bias voltages on a damaged sample 142

5-2 The net photocurrent vs. bias voltage curves for both MIS and PEC cells: undamaged, 0.05 μm and 0.1 μm 143

5-3 The net photocurrent vs. bias voltage curves for both MIS and PEC cells: undamaged, 0.3 μm and 1 μm 144

5-4 Illuminated J-V curves of PEC and MIS solar cells with "no oxide" 145

5-5 The dark J-V of PEC cells with various damage sizes indicating hole injection by ferricyanide 146

5-6 Calculated J-V curves according to dislocation conductivity model showing the effect of passivation 147

5-7 Dark J-V curves of MIS cells with 1 μm damage 148

5-8 The effect of passivation on J-V characteristics of damaged MIS cells 149

5-9 The effect of passivation of 1 μm damaged MIS cells

at various temperatures 150

5-10 The net photocurrent vs. voltage of MIS and PEC cells fabricated from unpassivated and passivated Si samples 151

5-11 The dark current of PEC cells with 1 μm damage 152

5-12 The anomalous J-V curves of passivated samples 153

5-13 Scanning Laser Spot map of a damaged sample 154

6-1 The dark current-voltage curves of an MIS cell at different temperatures 164

6-2 Variation of cell parameters with temperature 166

6-3 The dark current-voltage curves of a 1 μm damaged MIS cell at different temperatures 168

6-4 Variation of parameters of 1 μm damaged MIS cell with temperature 169

6-5 Temperature variation of differential resistance of an undamaged and damaged MIS cell 170

6-6 Calculated variation of the current along dislocations at $V >> V_{oc}$ with temperature 171

6-7 Variation of the reverse dark current due to exposure to room air after evacuating 172

6-8 The response of a 1 μm damaged cell vs. humidity 173

6-9 The illuminated J-V curves of 1 μm damaged cell that has undergone repeated cycling of exposure to room air and vacuum 174

A-1 The band diagram of the damaged MIS cell in one-sided-abrupt junction approximation 181

CHAPTER I

INTRODUCTION

Modern solid state theory is based on the concept of the space lattice or Bravais lattice. Atoms in a solid are thought of as being distributed on the imaginary lattice points. The periodicity of this atomic arrangement makes the theoretical understanding of the solids possible. However, this concept faced a major problem in the early days of its development when it was confronted with the mechanical strength of real crystals. The experimentally observed critical shear stress of a crystal (the force necessary to deform the crystal plastically) was about four orders of magnitude lower than the theoretically predicted value for a perfect crystal[1]. A way out of this problem was proposed by Taylor[2], Orowan[3] and Polanyi[4] in 1934 resorting to the concept of linear lattice imperfections called dislocations (DLs) which accounted for the discrepancy. Since then spectacular progress has been made in the material science area where whiskers almost devoid of any DLs, and consequently, of nearly perfect mechanical strength have been grown. Apart from their fascinating mechanical properties[5,6] DLs exhibit a variety of electrical properties as well.

1.1 Dislocations

Dislocations are best described geometrically using a cubic crystal. There are two basic types of dislocations,

one called edge type and the other called screw type. An edge dislocation can be visualized by slipping or gliding one atomic plane above another in only a part of the crystal by a unit lattice vector (Fig.1-1a) and rejoining the broken bonds on either side of the slip plane. The resulting boundary between the slipped part and the unslipped part of the crystal is a line of atoms (AD) with their valency only partially satisfied. This line is called an edge dislocation (denoted by ⊥, AD can also be conceived to be produced by inserting or removing a semi-infinite plane of atoms). Slip can occur in another way also as shown in Fig.1-1b where the atomic planes are twisted. This is called a screw dislocation. In a screw dislocation the boundary between the slipped and unslipped part, line AD, is parallel to the direction of slip. In an edge type DL the boundary line is perpendicular to the direction of slip. In practice one may encounter DLs of mixed character in addition to these two types. Fig. 1-2 shows such a DL with both edge and screw types. It should be noted that in the neighborhood of a DL the atomic positions are substantially different from the original sites, while away from this region regular crystallinity is preserved. Since a DL is a boundary between slipped and unslipped part of the crystal a DL line must either intersect the surface or close upon itself within the crystal forming a loop.

A dislocation is quantitatively characterised by an entity called the Burgers vector which is defined as follows[4-7]. A closed curve in the perfect crystal generated

by a series of Bravais lattice vectors is called a Burgers circuit. If such a curve is generated in a test path elsewhere by the same sequence of atom-by-atom displacements and fails to bring one back to the original position then the path has surrounded a DL. The Bravais lattice vector $\vec{b}$, required to complete the path is called the Burgers vector of that DL (Fig.1-3). The Burgers vector indicates how much the lattice has slipped and in which direction. Therefore, $\vec{b}$ is perpendicular to an edge DL while it is parallel to a screw DL. The angle between b and DL will vary between 0 and 90 when the DL is of mixed character.

Any kind of stress which brings a cystal into its plastic state will produce DLs. Thermal stress, mechanical stress and stress due to impurity diffusion etc., are sources of DL generation[8]. Unless precautions are taken, DLs are usually produced during crystal growth in the presence of the above mechanisms. A grain boundary is an array of DLs with a two dimensional character, and these defects are often produced during crystal growth.

Usually, the number of DLs intersecting a unit area of the crystal surface, called dislocation density (D_{dl}) and expressed in units of cm^{-2}, is used to describe the physical quality of the crystal. Generally, D_{dl} between 10^2 and 10^{12} are found in practice. Traditionally, DLs were detected by decorating them with metallic impurities and observing them with an infra-red microscope[9]. With the advent of the electron microscope, IR microscopy has been relegated to a

secondary status regarding this purpose, and it is only in the last decade that DLs have been observed directly using the transmission electron microscope (TEM). However, even with the TEM, the topological details of DLs are not revealed completely due to the size of atomic dimensions involved.

Technologically most important semiconductors, today, (Si, Ge, GaAs and GaP etc.,) have a tetrahedral atomic arrangement. Ge and Si have diamond structure while GaAs has zinc-blende structure, and each of these structures are considered to consist of two interpenetrating face centered cubic lattices. The cleavage plane of Si is (111). It is generally believed that slipping a (111) plane along a [110] direction produces pure edge type DLs by rupturing the covalent bonds between two adjacent (111) planes in Si and similar semiconductors (see Fig. 1-4a and b).

In 1953, Shockley suggested the possibility of having a one dimensional degenerate electron gas in the DLs of semiconductors having the diamond structure, which could give rise to electrical conduction along them[10]. In tetragonally coordinated crystals like Si, electrons form four sp^3 hybridized orbital per atom and they take part in covalent bonding with the four nearest neighbors[11]. The ruptured bonds along a DL can be represented by an array of atoms each having one electron in the unsaturated sp^3 orbital. These unsaturated electron orbitals are called dangling bonds, and these dangling bonds can produce energy states in the forbidden gap analogous to the well known case

of surface states. Similar to surface states such dislocation states in the gap should be able to act as donors by giving up the electron or as acceptor states by accepting an electron. In addition, owing to the periodicity of the arrangement along a DL, the overlap between these orbitals could, in principle, produce a 1D band which is half filled when neutral as Shockley discussed. Consequently, such a DL should exhibit the properties analogous to a 1D metal. This is theoretically a very attractive idea although practically, it is a device manufacturer's nightmare.

It is known generally that the presence of defects such as dislocations and grain boundaries in semiconductor materials used in device fabrication adversely effect their performance. After considerable activity in the field in the early days of semiconductor technology, the interest in the impact of such defects on device performance has become less, due to technological developments which have enabled the production of dislocation free silicon. However, when the cost is a large factor, such as with silicon solar cells, one needs to use the materials of lowest cost possible. The low cost materials, such as polycrystalline silicon, invariably are less perfect i.e, they contain defects such as dislocations and grain boundaries. On the other hand, even with dislocation free starting materials, the chances of introducing mechanical damage in device processing are not negligible[12]. Thus there are many practical reasons for improving our understanding of

electrical effects due to dislocations. Furthermore, if the compound semiconductors become technologically more important in future, the understanding of the electrical activity of DLs will be of value. Apart from the technological importance of the study of their effects, recent theoretical interest[13] in one dimensional conduction along dislocations is another motivation for studying them.

However, despite the research activity generated by Shockley's model a d.c. conductivity along DLs has not been observed up to now, although evidence for conduction along grain boundaries has been gathering for sometime[14]. Such evidence for grain boundary conductivity involves low temperature solid state measurements or room temperature electrochemical measurements[13,14,15]. Recent reviews of grain boundary conductivity[14] and low temperature DL conductivity[13] are available in the literature.

1.2 Objective

The basic objective of this thesis is to investigate and verify the existence of a d.c. conductivity along DLs in Si at room temperature, with an emphasis on the effect on the performance of solar cells. The direct observation of DL conductivity at room temperature is extremely difficult owing to the dominance of the high conductivity of the bulk. Using an MIS (metal-insulator-semiconductor) structure as the tool, the electrical properties of surface DL loops introduced to the semiconductor (Si) will be examined by monitoring the

current-voltage characteristics under both dark and illuminated conditions. The experimental results will be shown to be best explained in terms of a mathematical model based on conduction of captured carriers along DLs.

1.3 Organization

A brief review of the electrical properties of DLs in semiconductors is given in the next chapter along with the currently accepted theoretical model. The effect of DLs on semiconductor devices such as pn junctions, Schottky barriers, and the evidence for defect conduction will also be discussed. The basic characteristics of the MIS structure is also presented here. In chapter 3, the experimental techniques, the apparatus and their basic principles and relevant methodology will be presented. The experimental results obtained and the proposed model for explaining them are discussed in chapter 4 where data and model calculations are compared. In chapter 5 we discuss the corroborating results of electrochemical measurements on our samples carried out at the University of Gent in Belgium in a cooperative program, together with results of hydrogen passivation of dislocations. Moreover, the general observations of others are shown to be consistent with the DL conductivity model. Chapter 6 contains the results obtained for the temperature dependence of the MIS characteristics along with other interesting observations made throughout the study followed by the major conclusions of the thesis in chapter 7.

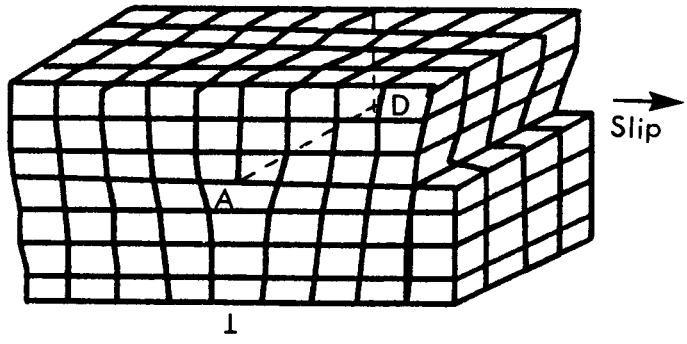

Fig.1-1a A pure **edge dislocation** (line AD) is formed by slip. AD is a row of atoms with unsaturated bonds in a cubic lattice.

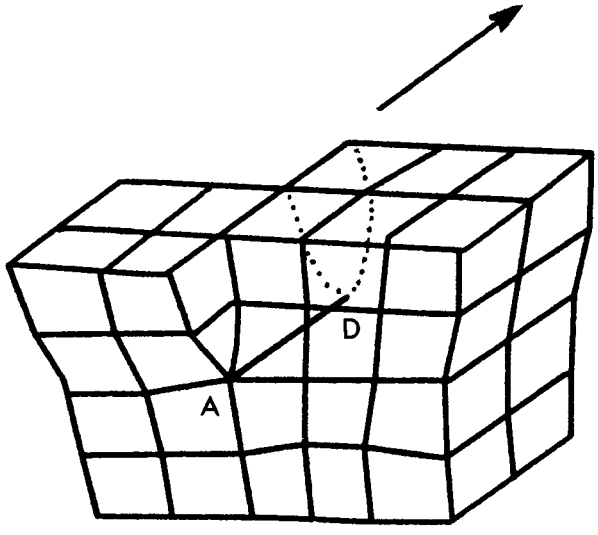

Fig.1-1b A pure screw dislocation (AD) formed by twisting the atomic planes.

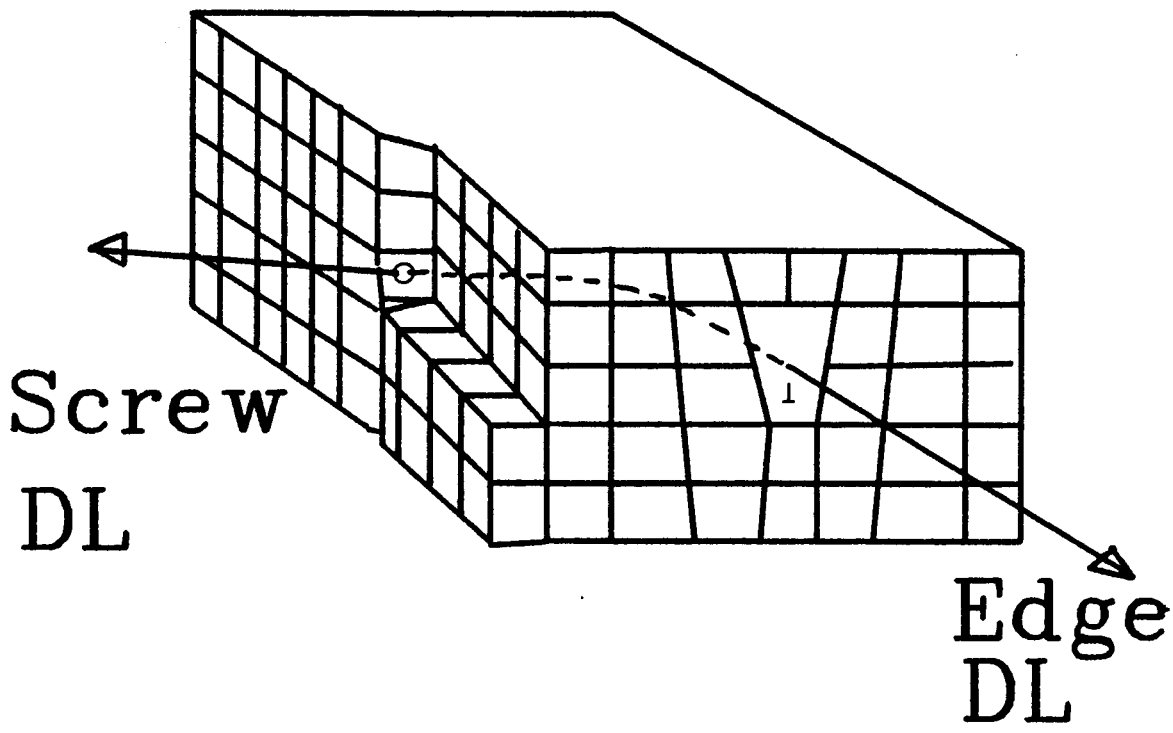

Fig.1-2 A part of a dislocation loop consisting of both edge and screw components. This is the general case.

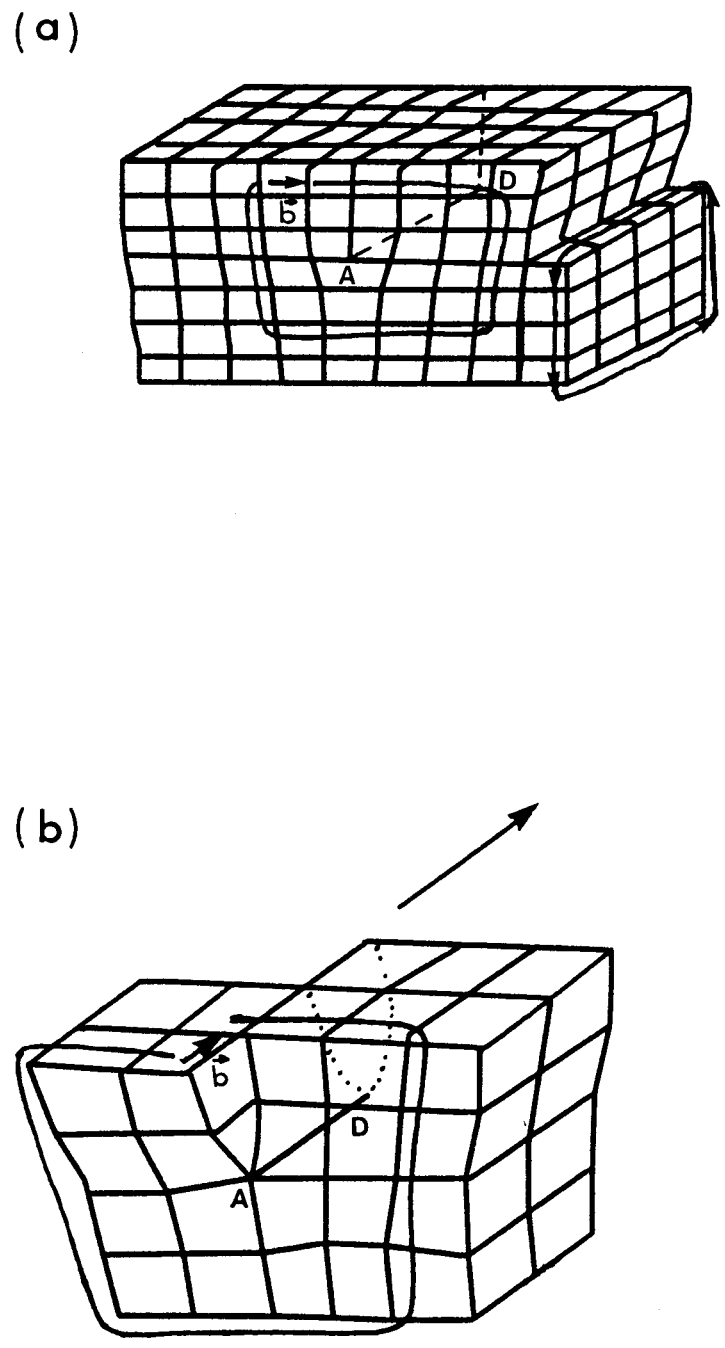

Fig.1-3 Burgers vectors and Burgers circuits of
(a) an edge dislocation.
(b) a screw dislocation.

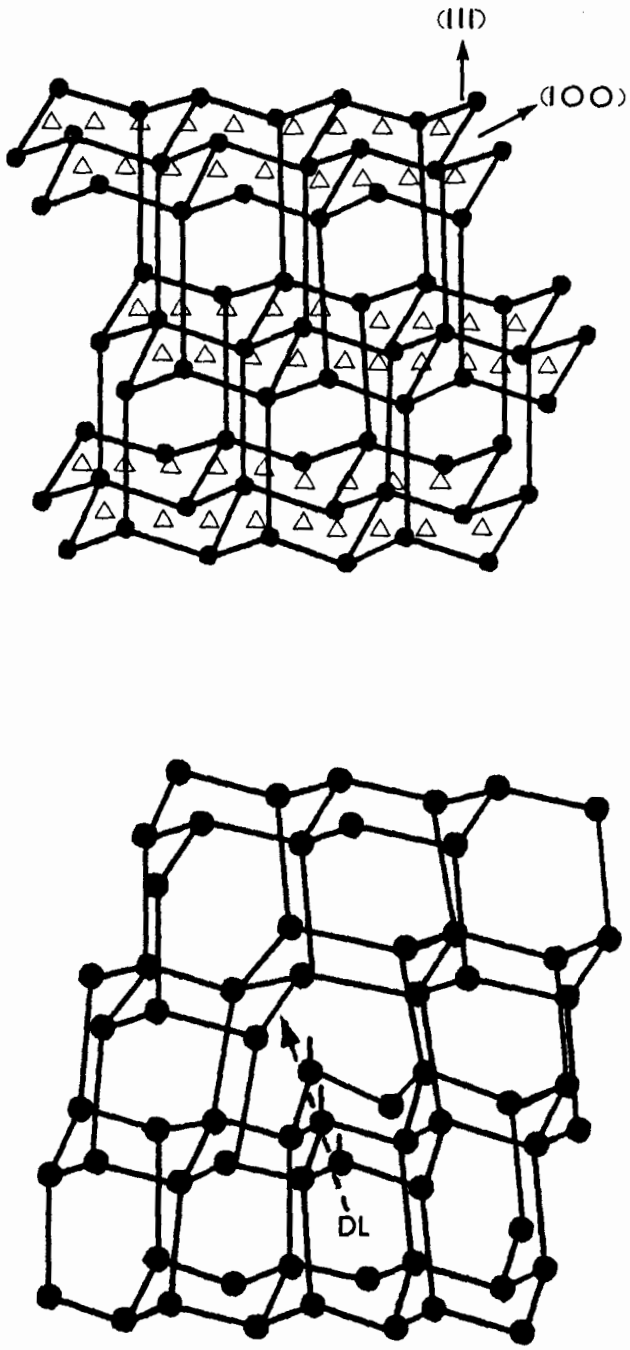

Fig.1-4 (a) The diamond structure showing {111} planes and the tetrahedral structure.
(b) An edge dislocation produced in the diamond structure where {111} planes have slipped. The dislocation is a line of dangling bonds.

CHAPTER II

REVIEW OF DISLOCATIONS AND MIS STRUCTURE

2.1 Physics of Dislocations

In a series of pioneering papers, Read suggested for the first time the existence of a space charge region (SCR) around a dislocation due to the charge associated with the dangling bonds[16,17,18]. As the dislocation is a line defect, the space charge forms a cylinder around it. Even though he assumed only a negative charge can be imparted to the dislocations, based on then available data on dislocated Ge, now it is well established that both positive and negative line charges can be associated with DLs giving rise to SCR cylinders[19,20] (Fig.2-1a).

There are many implications of the line charge and the SCR for carrier transport in semiconductors. For instance, the celebrated Shockley-Read-Hall (SRH) theory[21,22] of recombination was found to be inadequate for explaining experimental data on Si and Ge showing a slower decay rate of injected carriers than predicted by theory. Once it was recognized that the Coulombic interaction between the carriers and the line charge plays an important role in determining the recombination kinetics, the slow decay phenomena and the generation of 1/f noise associated with DLs could be explained. The effect of the SCR of DLs on recombination was first recognized by Morrison[23,24] and this basic idea was later extended by others to accomodate both types of line charges[25,26]. The electrostatic field around

DLs has been analysed by several authors[27] by solving the Poisson equation under various assumptions. In all the analyses the basic field variation around a DL is found to be given by a logarithmic potential with an inner cut off point determined by the spacing between the dangling bonds (Fig.2-1b). It is usually argued that the electrons which contribute to the line charge are not distributed along DL at random but at equal distances because of their mutual repulsion.

2.1.1 Half Filled Band (HFB) Model

Following Shockley[10], Shroeter and Labusch[28,29] developed the presently accepted theory called the half filled band (HFB) theory for the electrical properties of DLs in semiconductors (Fig.2-2). Read's original theory[16,17,18] assumes that DL states can be represented by a single level which is empty when the DL is in the neutral state while the HFB theory assumes the DL state is half filled when neutral. Since the two theories start from two different assumptions the final results are also different and obviously, the HFB theory enjoys the advantage of accomodating both types of line charges. Read's theory was outdated by the experimental evidence for the existence of both positive and negative line charges indicated by respective barriers[19,20] associated with them.

The experimental evidence for the HFB theory is mainly from the Hall effect data where the carrier density in a sample is determined by measuring the Hall coefficient

R_H. Upon deformation the carrier density changes due to filling of DL states. The carrier density (n or p depending on the type of semiconductor) is simply given by, $n,p = \mp 1/qR_H$. Measurements carried out on dislocated Si and Ge samples to study the temperature dependence of carrier density have been compared with the theoretically calculated values based on the HFB model. Theoretically, the average values for carrier densities $\langle n \rangle$ or $\langle p \rangle$ are found by minimizing the free energy of the system with respect to the filling factor f (the fraction of occupied states of the DL states) and the Fermi energy E_F. Very good agreement is obtained between the experimental data and theoretical predictions[28,29].

However, it has to be mentioned that there is no comprehensive theory of the DL core states due to the lack of experimental data regarding the atomic configuration at the core of the dislocations. This is a major obstacle for realistic band structure calculations[30].

In addition to the effect on the free carrier density DLs in semiconductors strongly reduce the mobilities[31] at low temperatures. The effect is shown schematically in Fig.2-3 (after Labusch and Shroeter[24]) where the temperature variation of the mobility for a Ge sample is given before and after deformation which introduces DLs. The undeformed sample shows phonon scattering as the predominant mechanism while the curve for the deformed sample is reminiscent of impurity scattering, and in fact the variation in mobility data is explained in

terms of scattering by DLs[31].

2.1.2 Dislocation conductivity

Experimental indications for electrical conduction along dislocations come from many areas of physics. Most of the significant evidence is due to groups working on microwave conductivity measurements on dislocated samples[32,33,34,35]. Si samples with DLs up to 10^9 cm^{-2}, introduced by plastic deformation, have exhibited high anisotropies in microwave conductivity (at 9.5 GHz)[36]. Anisotropies up to a ratio of 10 between the a.c. conductivities parallel to and perpendicular to the dislocation directions have been reported[29]. The variation of d.c. conductivity of these samples with temperature shows an activation energy of about 0.44 eV, and the results are interpreted as having DL levels 0.44 eV above the valence band. Mantovani and Pennino[37] have shown that the dislocations produced by bending (plastic deformation) introduce an energy level at 0.52 eV above the valence band in Si. However, there is some controversy regarding the exact values for the energy levels of DL states in Si and Ge, and values between 0.3 to 0.52 eV above the valence band have been reported[29,35].

A parameter called the specific conductance s is used in literature to describe the conductivity of the DLs, which is defined as $s = l / R$ where l is the length of the DL and R is its resistance[13]. Using low temperature microwave conductivity data s has been estimated to be

about 10^{-12} cm ohm^{-1} for Si at 4.2 K. This is the only such value available in the literature[15].

In an elegant experiment performed recently by Yu.A. Osip'yan it was shown that that the microwave conductivity of dislocated samples is due to capture of carriers at DLs[35]. Starting with highly pure undoped Ge crystals he measured the microwave conductivity of undeformed as well as deformed samples where great care had been taken in for not introducing impurities. No significant a.c. conductivity was found in either one of the samples at 4.2 K. A neutron doping technique was then used to initiate the production of impurity (doping) atoms through the following reaction with thermal neutrons.

1. Ge^{74} (n, γ) $\longrightarrow Ge^{75} \longrightarrow As^{75}$ (donor, 82 min)

2. Ge^{76} (n, γ) $\longrightarrow Ge^{77} \longrightarrow As^{77} \longrightarrow Se^{77}$ (donor, 35 hrs)

3. Ge^{70} (n, γ) $\longrightarrow Ge^{71} \longrightarrow Ga^{71}$ (acceptor, 12 days)

Knowing the isotropic composition of the original sample, and the production period of each final product species (indicated above within brackets), one can correlate the conductivity with carrier concentration. Starting with an undoped sample at 4.2 K he was able to turn it into n-type first, and then into p-type, while in between the transition it underwent a state where no free carriers were found. Fig.2-4 shows the results schematically. At the

onset, no significant microwave conductivity is observed because there are no free carriers available for capturing at DL states, and thereafter the conductivity follows the carrier profile available for capturing.

2.2 Grain boundary studies

As it was mentioned earlier, a grain boundary can be considered as an array of dislocations distributed on a plane. Hence, most probably, the properties of grain boundaries may reflect the electrical behavior of dislocations.

By electrochemical means, Morrison and Loo[14,38] have obtained experimental evidence which is very much indicative of carrier transport along grain boundaries in polycrystalline silicon. They employed chemical species having suitable energy levels in an electrolyte so that holes can be injected selectively into the sub-band gap grain boundary states while avoiding injection into the valence band. Such "tuning in" to the energy levels in the band gap was made possible by their previous work regarding the position of band edges in silicon with respect to a standard calomel electrode (SCE).

Following Morrison and Loo, Sears[39] used the same method to confirm their findings and showed that similar results are obtained with a mechanically damaged (abraded with a polishing powder) sample[39]. This same technique has been used by the group in University of Gent, Belgium for confirming the findings of this thesis, and their results

are discussed in Chapter 6.

The basis of the electrochemical technique is as follows. It has been established that the flat band potential of p-silicon with respect to the SCE is given by E_{fb}= 0.35 - 0.035P in eV at a given pH value P of the electrolyte. So, by knowing the pH value of the electrolyte and using a couple of chemical species (a so-called redox couple) of known electrode potential (E_o) with respect to SCE, one can construct a band diagram where the energy levels of the reactive species can be indicated relative to the band edges of Si (Fig. 2-5).

Examining Fig.2-5 one can expect that Fe^{+3}(aquo) should inject holes, i.e. capture electrons from the valence band, into the valence band but, Fe^{+3}EDTA (ethylene diamine tetraacetic acid) should not, and all the species should be able to inject holes into grain boundary levels. Results of measuring the reverse current (cathodically biassed with respect to SCE) of a polycrystalline silicon electrode are shown in Fig.2-6 with and without Fe^{+3}(EDTA) in the electrolyte. As Morrison and Loo[38] argue there are two possible causes for the origin of the extra current observed in curve b) compared to a). One is the space charge generation of minority carriers at grain boundaries while the other is the hole injection into the grain boundary levels from the solution. By the low reverse current observed in the single crystal one can rule out the possibility of hole injection from protons in solution to the valence band. In the presence of Fe^{+3}(EDTA) in the

solution an additional current component is observed. Since the mere presence of Fe^{+3}(EDTA) can not increase the SCR generation, and since with single crystal Fe^{+3}(EDTA) does not inject holes into the valence band, it is concluded that a) holes are injected into grain boundary levels and b) these holes are conducted along grain boundaries to the bulk and c) they are thermally activated into the valence band.

Direct electrical conductivity measurements by Miremadi and Morrison[40] on polycrystalline silicon samples (four probe measurements parallel to and perpendicular to grain boundaries) with Fe precipitated on to the boundaries also indicated the possibility of grain boundaries having an electrical conductivity that decreased with iron concentration in the defects. This type of conductivity has been suggested by several authors previously[43,44], and has been reviewed recently by Matare[45,46]. A similar situation could justifiably be expected from DLs in silicon.

2.3 Effect of DLs on Devices

The most studied effect of DLs on semiconductors, judging from the volume of publications, is recombination of carriers. Minority carrier lifetime in semiconductors has been found to be inversely proportional to the density of DLs[47,48]. This adversely affects the performance of most optoelectronic devices. The efficiency of $Ga_{1-x}Al_xAs$ light emitting diodes (LEDs) has been found to be lowered by the presence of DLs[49], and recombination at DLs has been shown

to explain the behavior by analyzing the data in terms of a detailed model[50]. Scanning electron microscopic techniques such as electron beam induced current (EBIC) and cathode luminescence (CL) have been used to show that there is a 1:1 correspondence between the observed dark spots in electroluminescence maps and dislocations in GaP[51] which confirms carrier recombination at such defects. Recombination at DLs created at the interfaces due to lattice mismatch between the substrate and the epitaxially grown GaAs was recently shown to reduce the conversion efficiency of thin film solar cells[52,53].

Other major deleterious effects associated with DLs which have received much attention are the electrical breakdown of junction devices at DLs[54,55], higher leakage currents in pn junctions[56,57,58] (usually explained in terms of recombination/generation centers), lowering of transistor gain[59] and poor performance of solid state lasers[59]. A much less studied effect is the shunting of pn junction (or a solar cell) due to a DL threading through it. In a recent study on silicon diodes where DLs have been introduced by plastic deformation, Nitecki and Pohoryles[15] assumed the possibility of conduction along DLs to explain their photocapacitance and dark current-voltage data at liquid nitrogen temperature. Since the line defects were introduced by deformation they were distributed through out the samples and, according to the authors, consisted of short loops or segments (about 1000 Å).

The shunting of such a junction by grain

boundaries has been analysed by Morrison[60]. A model was presented to show that the solar cell performance can be degraded due to carriers conducting along grain boundaries if they possess a suitable sheet conductivity. A similar approach will be adapted in the course of the analysis in this thesis. However, the mathematical model will be quite different here partly due to the different physical conditions that give rise to different boundary conditions. The major difference will be the finite length of the defects considered which are primarily concentrated at the surface of the cell. As will be shown, comparing the studies of Nitecki and Pohorolyse and that of Morrison, this imparts an added advantage both experimentally and theoretically for observing carrier conduction along dislocations.

2.4 The MIS Solar Cell

Metal-insulator-semiconductor structures have become technologically very important during the past decade due to the diverse possible applications, for instance, solar cells and photodiodes[61,62,63,64], surface oxide transistors[65], imaging devices[66], switching devices[67] and gas detectors[68,69]. Consequently, the properties of the MIS structures have been under study for some time by a large number of workers. A major incentive for the use of the MIS structure is its simplicity of fabrication, where only low temperature processes are involved, compared to conventional pn junction solar cells where high temperature diffusion

processes have to be employed.

As the name implies the structure consists of a thin (< 30 $\mathring{A}$) insulator sandwiched between a metal and a semiconductor. Fig.2-7 shows a typical physical structure of such a cell. As with any other type of solar cell the operation of an MIS cell rests on the existence of a built in electric field which can separate photoproduced electron-hole pairs before they recombine. Fig.2-8a shows the band diagram for an Al-SiO_x-pSi cell at zero bias. The electric field (or the band bending) is created by to the difference between the work functions of the metal and the semiconductor, and the region where the field exists is called the space charge region (SCR). However, the fixed charges in the insulator also play an important role in the electrostatic configuration of the device. In fact, it is now accepted that the positive charges in SiO_x layer augment the field, enhancing the voltage that can be developed across the structure when illuminated. The fact that one obtains a lower voltage in an n-Si structure than in a p-Si is explained by the presence of these charges in the insulator[63].

In the particular structure that we are interested in, the low work function of Al, ϕ_{Al} (=3.2 eV) induces an inversion layer at the p-Si surface near zero bias (at equilibrium) where the Fermi level of Si (E_{FS}) coincides with that of Al (E_{FM}) (Fig.2-8a). The electron affinity of Si (χ_{Si}) is also 3.2 eV, hence the metal Fermi level is almost aligned with the edge of the conduction band of

Si[61]. The electron concentration, which is given by the Fermi-Dirac distribution in that it depends on the energy difference between the conduction band and the Fermi level of the semiconductor, is high at the surface. This induced inversion layer acts like a source of electrons so that the MIS structure can be effectively considered as an n^+p junction provided that the insulator is thin enough for electrons to tunnel through it without hindrance[61,62,70].

2.4.1 Current-Voltage Characteristics

The carrier transport in MIS solar cells has received wide attention and has been analysed by many workers emphasising different phenomena. The effect of the surface states[71,72,73], the effect of the oxide charges[74], recombination in the space charge region[75], multi-step tunnelling through defects in the insulator[76], back surface field effects[77] and inversion layer effects[78,79] are some among them.

However, it is well established that the carrier transport between the metal and the semiconductor is by quantum mechanical tunneling, and generally, it is treated using the WKB approximation[80,81]. The current transport in the structure is indicated in Fig.2-8 where b) at a small forward bias (p-Si positive with respect to Al), c) at a high forward bias and d) at reverse bias (p-Si negative with respect to Al). The electron particle current is always opposite to the direction of the conventional current shown in Fig.2-8. The difference between the metal Fermi energy,

E_{FM} and the edge of the valence band, known as the barrier height ϕ_{bo} (for majority carriers) is relatively high in this structure. Similarly a barrier height for the minority carrier also can be defined as the difference between E_{FM} and the edge of the conduction band E_{CB}. The majority carrier tunnel current J_p is given by

$$J_p = A_v^* T^2 \exp(-q\phi_{bo}/kT)\exp(-x_p^{1/2}d)(\exp(qV/kT) - 1) \quad (2-1)$$

where $A_v^* = 4\Pi m_p qk^2/h^3$, m_p is the effective hole mass, k is the Boltzmann constant, x_p is the hole affinity of Si, d is the thickness of the insulator, V is the applied voltage and T is the temperature[80].

By studying the current transport properties of Al-SiO_x-pSi structure both theoretically and experimentally Green et. al.[81] have shown that when d < 20 A the minority carrier current dominates the dark current-voltage characteristics similar to the case of a n^+p junction. This can be seen by the expression for the majority carrier current too. Since the barrier height for majority carriers is relatively high the corresponding current will be suppressed due to the exponential terms in Eq.2-1.

If the insulator is sufficiently thin the current will be predominantly carried by minority carrier electrons, and will be limited by the rate at which they diffuse in the p-Si, hence termed semiconductor limited current. This will be given by the ideal Shockley formula for a one sided junction as

$$J_n = J_o \, (\exp(qV/kT) - 1) \qquad (2\text{-}2)$$

where $J_o = qD_n n_o/L_n$, D_n and L_n are the minority carrier diffusion constant and the minority carrier diffusion length in p-Si, respectively, and n_o is the equilibrium electron concentration. n_o can be expressed as $n_o = n_i^2/N_A$ where n_i is the intrinsic carrier concentration in p-Si at room temperature and N_A is its acceptor concentration.

An MIS structure can be classified either as a minority carrier structure or a majority carrier structure according to which type of carriers dominates the transport in the dark[7e]. By selecting a low work function metal and p-Si or high work function metal with n-Si one obtains a minority carrier device while, conversely, a high work function metal with p-Si or low work function metal with n-Si renders a majority carrier device. It is of interest to note that the resulting minority carrier devices are electronically quite similar to conventional pn junctions.

The dark current has two other parasitic components: one being the recombination/generation current in the space charge region, J_{rg}, given by the Shockley-Noyce-Sah theory[82] as

$$J_{rg} = J_{ro} \, (\exp(qV/2kT) - 1) \qquad (2\text{-}3)$$

where $J_{ro} = qn_i W/ 2t$, W is the width of the SCR, and t is

the minority carrier life time. The other component is the recombination current due to surface states J_s which can be generally expressed as[73,83]

$$J_s = q\sigma v_t N_t n_i^2 / n_s \qquad (2-4)$$

where σ_t is the carrier capture cross section of the surface states, v_t is the thermal velocity of carriers, N_t is the density of the surface states per unit area and n_s is the surface concentration of electrons. $_t$ and v_t for both electrons and holes are assumed to be the same here.

The total dark current, J_d can be written as

$$J_d = J_n + J_{rg} + J_s \qquad (2-5)$$

and usually this is expressed as one exponential term by incorporating a quantity called the device quality factor, n where $n > 1$. Then we have

$$J_d = J_{od} (\exp (qV/nkT) - 1) \qquad (2-6)$$

where J_{od} is the saturating dark current density.

When light shines on the device the photocurrent due to minority carriers will flow in the opposite direction to the forward dark current (Fig.2-9). To obtain good performance the forward current of the cell should be kept minimum. The total current under illumination, J_L is then obtained using the superposition principle which

states that the illumination current density of a solar cell at a given bias (voltage) is given by superposing the short circuit current (J_{sc}) of the device to the dark current (J_d) at the same bias. The validity of this principle has been examined by several authors and has been found to be good even in the presence of recombination in the SCR[84]. Then it follows that

$$J_L = J_{sc} - J_d \qquad (2\text{-}7)$$

or

$$J_L = J_{sc} - J_{od}(\exp(qV/nkT) - 1) \qquad (2\text{-}8).$$

Usually, four parameters are defined for characterizing solar cell output. They are the short circuit current density (J_{sc}), the open circuit voltage (V_{oc}), the fill factor (FF) and the efficiency (η). The J_{sc} is the current density under illumination at short circuit conditions which should ideally be equal to the photogenerated current density (J_{PH}), the voltage measured at open circuit conditions is V_{oc} and is expressed by

$$V_{oc} = (nkT/q)\ \ln(J_{sc}/J_{od}) \qquad (2\text{-}9)$$

which is obtained by setting $J_L = 0$ in Eqn.(2-8). The FF is defined as

$$FF = (V_{MP}J_{MP}/V_{oc}J_{sc}) \qquad (2\text{-}10)$$

where V_{MP} and J_{MP} are the voltage and the current density at the particular point on the current-voltage characteristics where maximum power is generated (Fig.2-9). The maximum conversion efficiency, η of the device is then given by

$$\eta = (V_{MP}J_{MP})/P_{IN} \qquad (2\text{-}11)$$

or

$$\eta = (V_{OC}J_{SC}FF)/P_{IN} \qquad (2\text{-}12)$$

where P_{IN} is the power density of the incident light on the cell.

Very highly efficient MIS cells have been fabricated using Si, the highest reported so far being 17.6% at AM0 illumination by Godfrey and Green[85]. The term AM0 refers to solar illumination. It is customary to express solar illumination in air mass numbers (AM) to describe the attenuation by the atmosphere. The AMn illumination corresponds to an average solar illumination when the sun is at an angle θ to overhead where $n = 1/\cos\theta$. Hence, AM2 is when the sun is at 60° to overhead. The term AM0 is defined as the illumination just out side the atmosphere.

2.4.2 The capacitance of MIS structure

The differential capacitance of an n^+p junction is given by[85]

$$C = dQ_{SCR}/dV = (qe_sN_A / 2(V_{bi} - V - kT/q))^{1/2} \quad (2-13)$$

where e_s is the permittivity of the semiconductor and N_A is the acceptor density in the semiconductor. Eqn.(2-13) can be rewritten as

$$1/C^2 = (2 /qe_sN_A)(V_{bi} - V - kT/q) \quad (2-14)$$

A plot of $1/C^2$ vs. V (called a Mott-Schottky plot) will, therefore, be a straight line with a slope inversely proportional to N_A and an intercept of $-V_{bi} + kT/q$. Therefore, capacity measurement will enable determination of the barrier height V_{bo} since it is related to V_{bi} by

$$V_{bo} = V_{bi} + \mu \quad (2-15)$$

where $\mu = E_{FS} - E_{VB}$[94].

In an actual MIS structure the oxide and surface states will add complications to this simple picture. Fig.2-10a shows the equivalent circuit for an MIS structure which takes both of these into account. C_{ox} is the capacity due to the oxide (insulator), C_{SCR} is the capacity due to the SCR, C_s and R_s are the capacity and resistance associated with the surface states which are used to define a life time characterizing them by $t_s = R_sC_s$. By choosing a frequency, f which is large compared to $1/t_s$ one can avoid

the effects of the surface states in practice (Fig.2-10b). This can be easily shown by calculating the equivalent values for a parallel combination of a resistance and a capacitance and then examining their behavior at high frequency. The capacitances given above for the systems can be expressed as follows:

$$C_{SCR} = e_S / W_{SCR} \qquad (2\text{-}16)$$

and

$$C_{ox} = e_o / d \qquad (2\text{-}17)$$

where e_S and e_o denote the permittivities of the semiconductor and the oxide, respectively, d is the thickness of the oxide and W_{SCR}, the SCR thickness given by

$$W_{SCR} = ((2e_S/qN_A)(V_{bi} - V - kT/q))^{1/2} \qquad (2\text{-}18).$$

For a thin (20 Å) oxide the impedence due to C_{ox} is negligible compared to that of C_{SCR}. Hence, at high frequency ($\sim$100 kHz) the Mott-Schottky plot can be used to determine the barrier height.

Charlson and Lien[61] have used three independent methods including the Mott-Schottky plot to evaluate the barrier height in an MIS structure with d = 20 - 40 Å, and they have shown that they all yield nearly the same value.

In the presence of an inversion layer, as mentioned earlier, Shewchun et. al.[62] have shown that Eqn.2-14 takes the form

$$1/C^2 = (2/q\varepsilon_s N_A)(V_c - V - kT/q) \qquad (2\text{-}19)$$

where $V_c = qN_AW_o/\varepsilon_s$ with W_o being the width of the SCR at thermal equilibrium (at zero bias). Furthermore, they show that the total width of the SCR at a bias V is given by

$$W = (W_o^2 - 2\varepsilon VN_A)^{1/2} \qquad (2\text{-}20)$$

The value of the surface potential needed to invert the surface, V_{inv} is given by[88]

$$V_{inv} = (2kT/q)\ln(N_A/n_i) \qquad (2\text{-}21).$$

And since it has been shown that the conduction band and the metal (Al) Fermi level are aligned with each other, an applied bias will mainly appear as an increment of the width of the space charge region. Moreover, it is generally known that the thickness of the inversion layer is quite small compared to that of the SCR[89]. Hence, the contribution of the inversion layer to the device capacitance can be neglected. In this approximation, if the experimentally determined V_c is larger than V_{inv} (given by Eqn.2-21) one can ascertain that the surface is inverted.

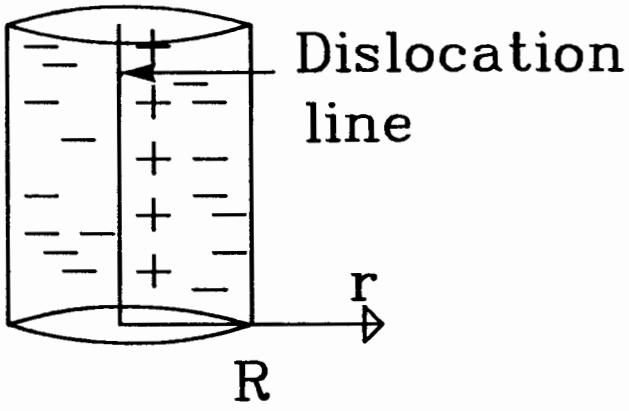

Fig.2-1a The line charge of a dislocation and the cylindrical space charge region (DSCR) around it. R is the radius of the SCR.

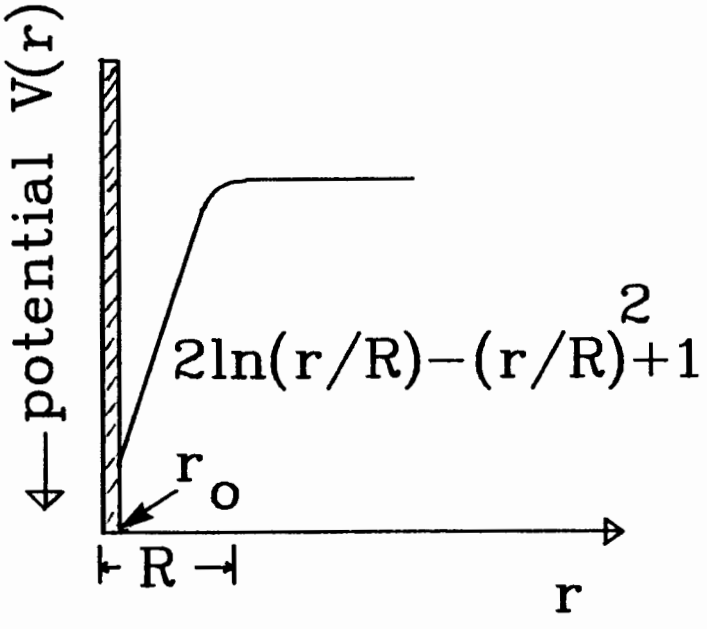

Fig.2-1b The potential of a dislocation has a logarithmic form. The inner cutoff point, r_o is assumed to be few angstroms.

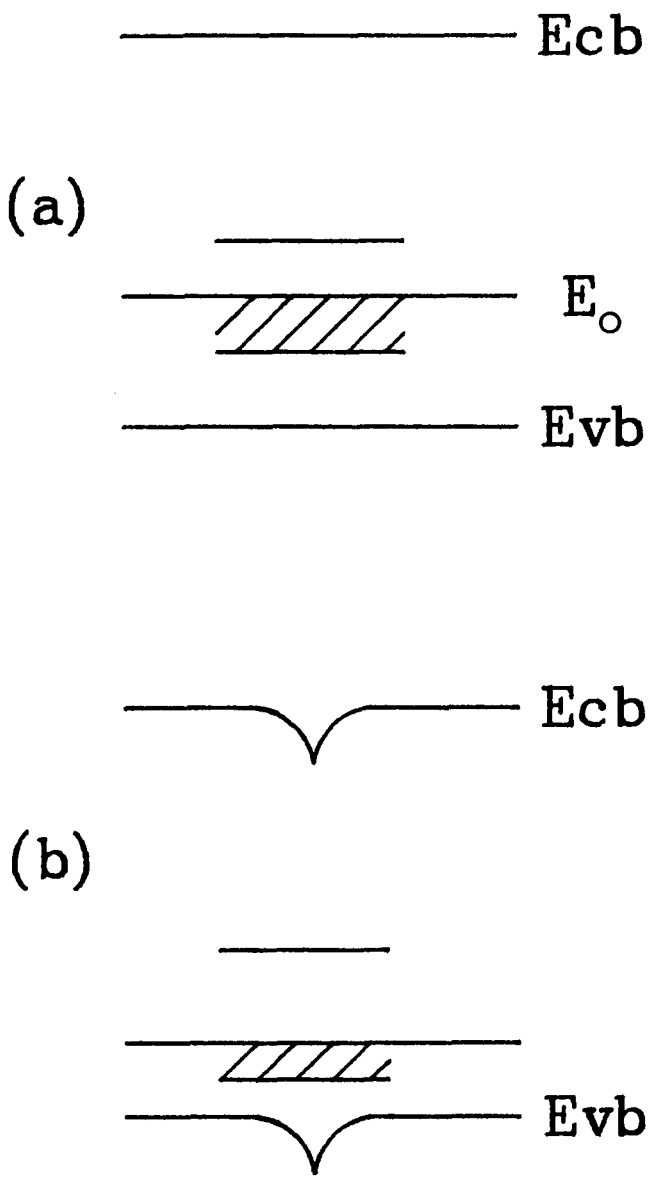

Fig.2-2 The half filled band (HFB) model.
(a) A neutral dislocation.
(b) A positively charged dislocation.

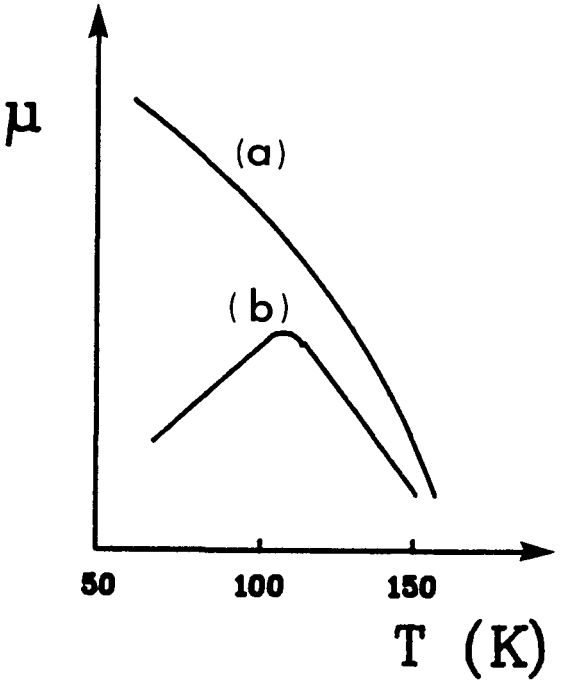

Fig.2-3 The variation of the mobility of a Ge sample is shown schematically before and after deformation.

(a)Undeformed
(b)Deformed.

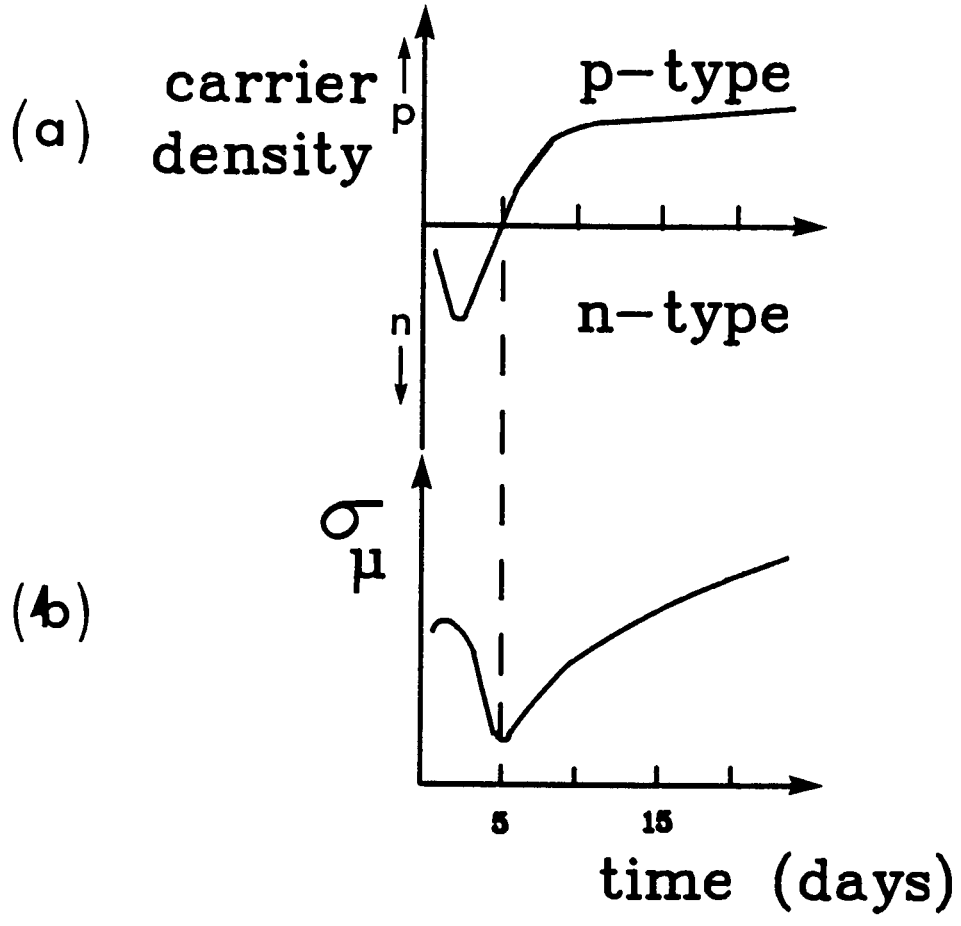

Fig.2-4 The results of Osip'yan's experiment are indicated schematically.
(a) The variation of carrier density with time after irradiation of Ge sample with neutrons.
(b) The corresponding variation of microwave conductivity.

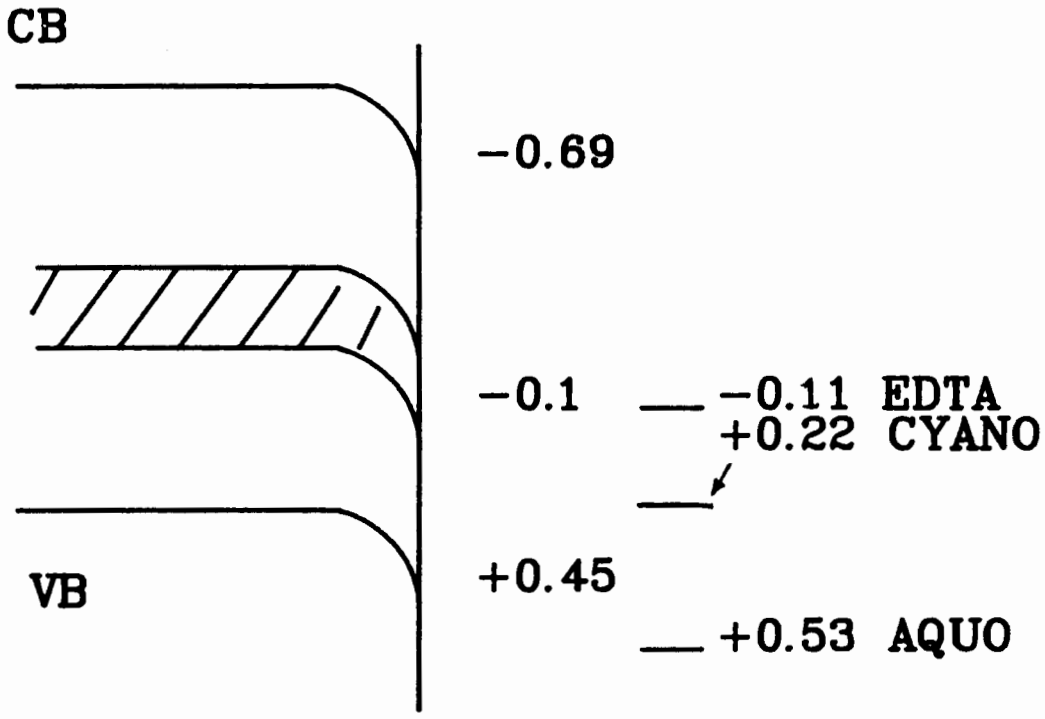

Fig.2-5 The band diagram of p-type polysilicon (at pH3) showing relative positions of (Fe^{+2}/Fe^{+3} EDTA, Fe^{+2}/Fe^{+3} cyanide and Fe^{+2}/Fe^{+3} aquo) redox couples

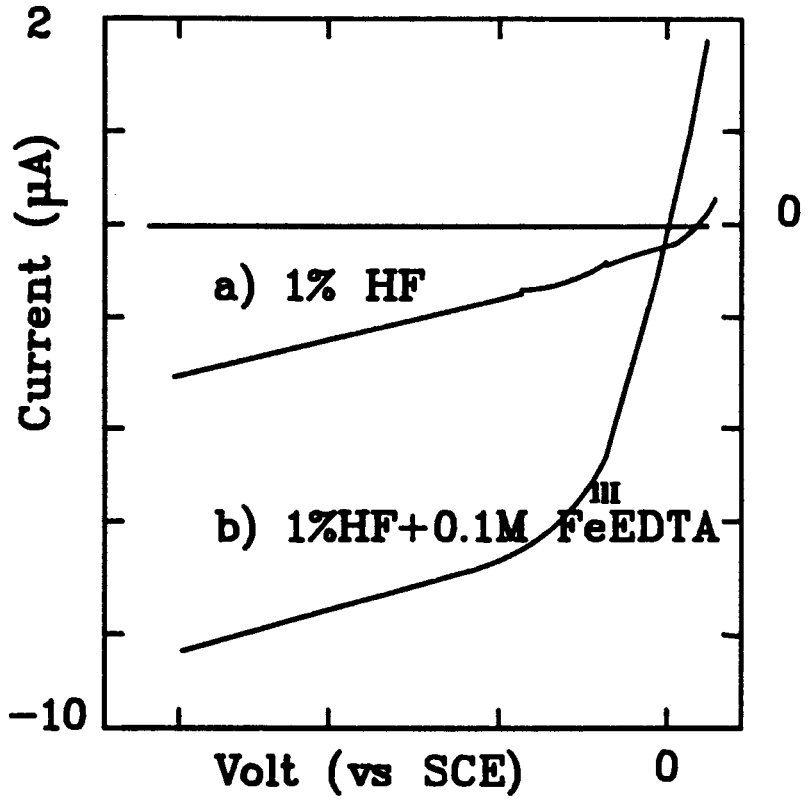

Fig.2-6 Reverse bias current-voltage characteristics for p-type polycrystalline with and without Fe^{III} EDTA in solution.

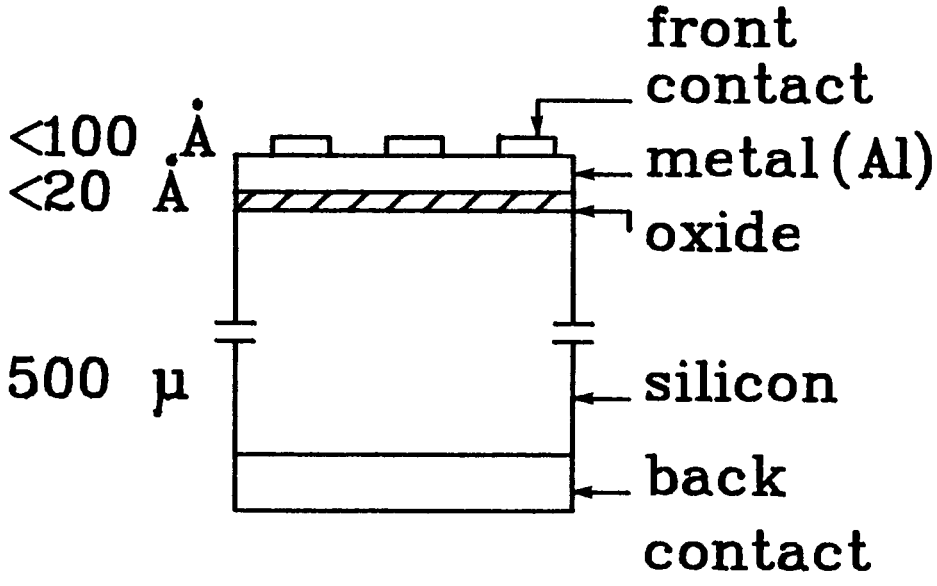

Fig.2-7 The structure of a metal - insulator - semiconductor (MIS) solar cell.

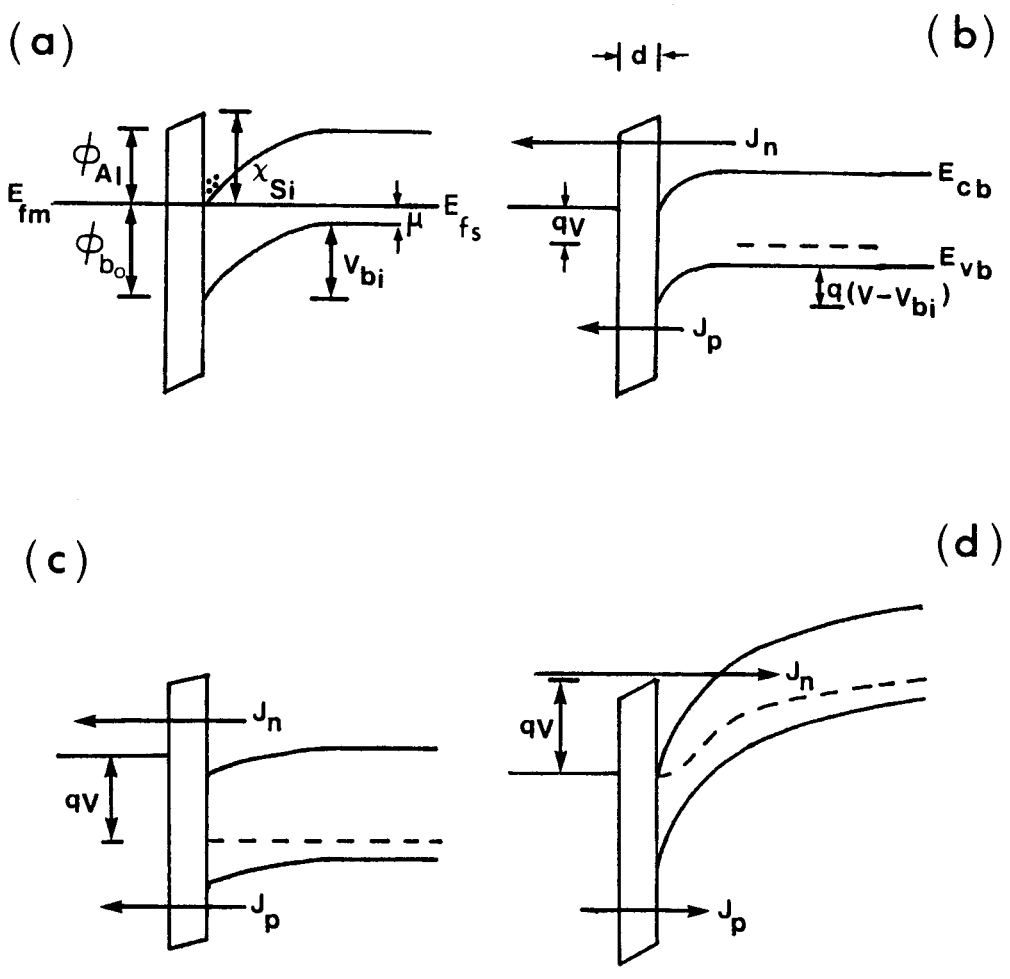

Fig.2-8 The band diagram for an Al-SiO_x-pSi MIS sructure.

(a) At zero bias
(b) At a small forward bias
(c) At high forward bias
(d) At reverse bias

ϕ_{bo} is the barrier height at zero bias. The inverted surface gives rise to a minority carrier device at reverse bias and at small forward bias.

The work function of Al, ϕ_{Al} = 3.2 eV

The electron affinity of Si, χ_{Si} = 3.2 eV

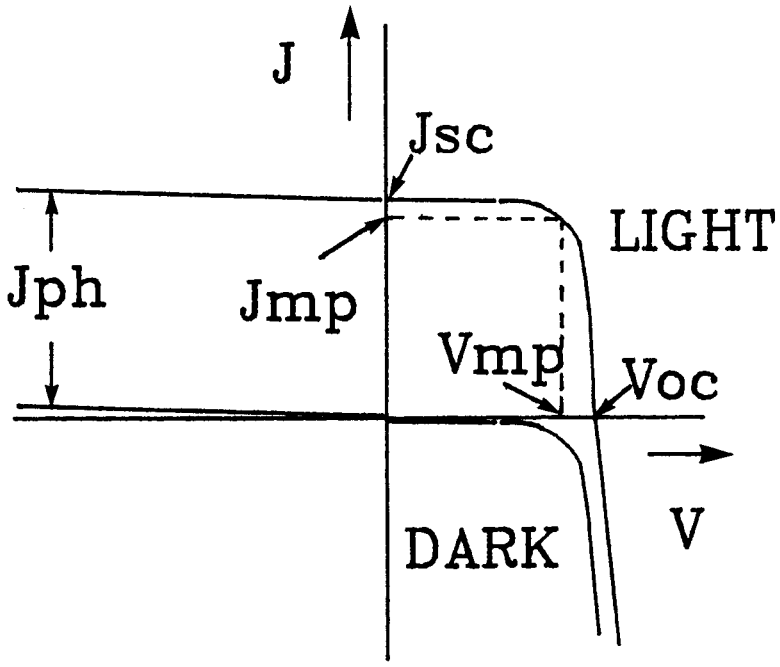

Fig.2-9 The current - voltage characteristics of a solar cell.

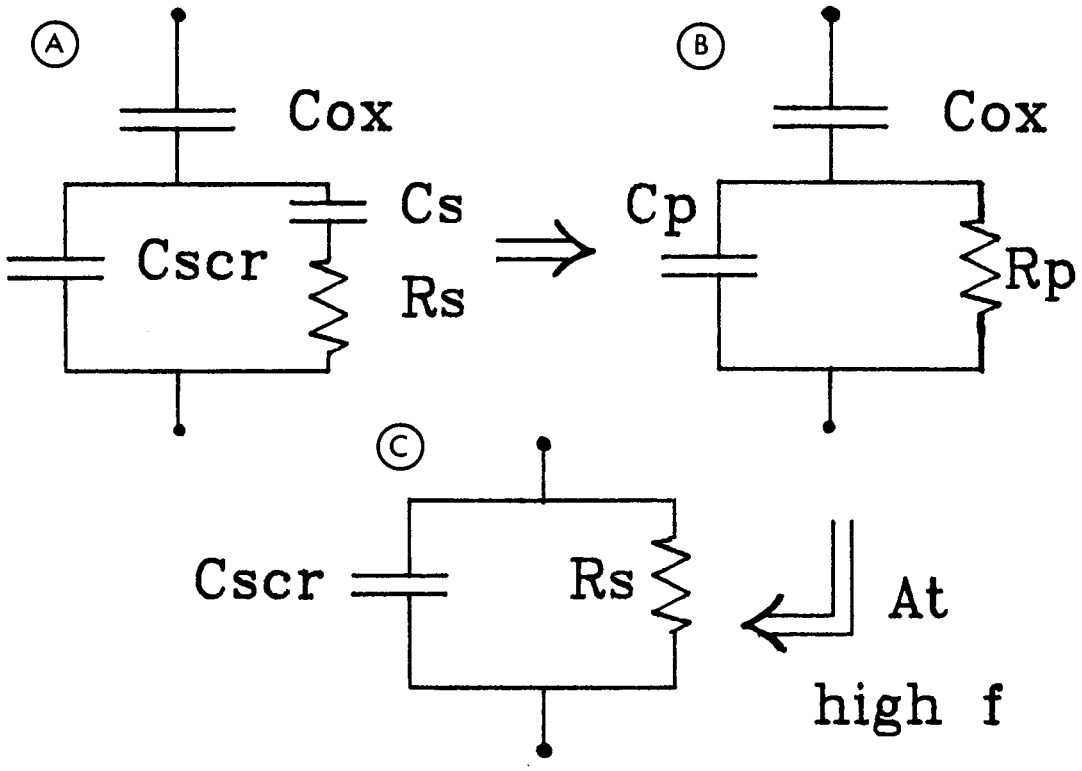

Fig.2-10 The equivalent circuit for an MIS structure. At higher frequencies, $f > 1/\tau$ ($\tau = R_s C_s$) the circuit a) reduces to c).

$$C_p = C_{scr} + \frac{C_s}{1 + \omega^2\tau^2} \quad , \quad R_p = \frac{1 + \omega^2\tau^2}{\omega^2\tau C_s}$$

CHAPTER III

EXPERIMENTAL

3.1 Generation of dislocations

It is well known that dislocations can be introduced into a crystal by plastic deformation[7,90]. With silicon this is carried out at temperatures > 700°C in a bending apparatus. However, great care has to be taken to avoid introducing impurities to the sample because at these temperatures the diffusivities of the impurities are high (such as Fe, Cu etc,). Hence deforming the samples has to be carried out in a vacuum.

Another method of generating dislocations is lapping the surface of the sample with an abrasive powder[91,92]. This method minimizes the problem of impurity diffusion since it is carried out at room temperature. The dislocations so produced are in the form of loops since[92] a dislocation has to start and end at a surface (Fig.3-1). The exact morphology is not well known in this case but, presumably, it is a mix of both edge type as well as screw type dislocations (see section 1.1). This method is ideal for studying dislocations with solar cells since the generated dislocations are concentrated at the surface of the sample. In contrast, plastic deformation produces dislocations throughout the bulk of the sample.

3.1.1. The depth of damage.

A wealth of evidence is found in the literature[93-97] which shows that the depth of damage produced by mechanically abrading a semiconductor is comparable to the diameter of the particles used for lapping. Semiconductors such as Ge, Si, ZnO, TiO_2, GaAs, InSb, GaP, InAs and GaSb have been investigated with polishing powders such as diamond, SiC and Al_2O_3 of various sizes ranging from 0.3 to 70 μm.

There are a large number of experimental techniques for determining the depth of damage but they all follow the same basic methodology. First, a physical or chemical property (eg. IR reflectance, conductivity, x-ray line broadening, etch rate, photomagnetoelectrical (PME) voltage) of the material, which has a different value in the bulk than in the damaged layer is selected. The sample is weighed and that selected property is measured, a thin layer of the surface is etched away, the sample is reweighed and remeasured. This sequence is repeated until there is no further change in the measurement of the selected property indicating the undisturbed bulk has been reached. Knowing the density and the surface area of the sample the thickness of successively removed layers can be calculated. Then a parameter representing the selected property is plotted against the thickness of the incrementally removed layer and a curve similar to one shown in Fig.3-2 is obtained. The

saturating point (point a) indicates the thickness of the damaged region where the dislocations are found.

3.1.2. Determination of density of dislocations.

There are a variety of techniques for determining the density of dislocations in a sample, out of which "etch pit" counting was selected because of its simplicity[78]. In this standard method the sample is treated with a preferential etching solution which removes atoms at different rates in different crystallographic directions (Fig.3-3). The final result is the formation of etch pits where dislocations intersect the surface. Since, one-to-one correspondence has been established[78] between the dislocations and etch pits the density of dislocations can be determined by establishing the density of etch pits. This is usually done by counting the etch pits after obtaining a scanning electron micrograph of the prepared surface.

3.1.3 Experimental.

All experiments described in this thesis were carried out using p-type (boron doped) single crystal silicon wafers of <100> orientation, obtained from AMETEK (Silicon Material Division, California). The resistivities of the wafers were in the range of 2 - 10 ohm cm and their thicknesses were 525 +/- 25 μm. Initially, the wafers were cut into 1 cm squares in such a way that the surface which has been polished by the manufacturer to a mirror-like

finish was kept intact, so that the starting materials were in principle of zero dislocation density. These cut pieces were degreased by rinsing, sequentially, in a series of cleaning liquids, viz, trichloroethylene, acetone, methanol and water. Then they were etched in 48% hydrofluoric acid for one minute, to remove their native oxide, and washed in distilled water.

A slurry of polishing powder in water was prepared with agglomerate-free alumina powder obtained from Baikalox Corporation, California. The slurry was kept in an ultrasonic bath for about 10 minutes to make sure that the Al_2O_3 particles were well dispersed without agglomeration. About 2 ml of the slurry was immediately transferred on to a clean glass plate and the shiny side of a cleaned silicon piece was hand lapped on this Al_2O_3 suspension for 1 minute. The sample was thoroughly cleaned with deionized water after lapping, and the alumina particles still adhering to the surface were removed by ultrasonicating for about 3 minutes. This procedure was repeated with Al_2O_3 powder of different sizes viz, 0.05 μm, 0.1 μm, 0.3 μm and 1 μm to prepare samples with dislocations penetrating various depths into the sample surface.

Dash etch[9] which is composed of one part of HF, 3 parts of HNO_3 and 10 parts of acetic acid was used for revealing the dislocations. A pilot experiment had to be done to determine a suitable etching period for the samples because etching for longer time will give an unrealistic value by joining more than one etch pit together while on

the other hand, if too shorter period of time is used the dislocations will not be revealed at all. A 200 Å thick gold layer was evaporated on the lapped surface of the samples to avoid imaging problems due to electrostatic charging when using the SEM for obsrevations. Qualitatively observing the SEM micrographs of damaged silicon samples obtained after etching them for various periods of time, it was determined that 20 second is the optimum etching period.

3.2 Sample Preparation

There are three major steps in fabricating an MIS solar cell namely, a) preparing an oxide layer of suitable thickness on the semiconductor, b) depositing a thin transparent metal film on the oxide and c) making electrical (ohmic) contacts to the top metal layer as well as the back side of the semiconductor.

3.2.1 The insulator and its thickness measurement.

The oxide was grown thermally on silicon using a Lindberg furnace (2900 W) and its thickness was measured ellipsometrically. The required thickness of the oxide layer on the surface of silicon is < 20 Å. Ellipsometry, being a very sensitive (up to 1 Å) and a non-destructive technique, is the standard method of determining the thickness of oxides in this range[99]. Gaertner model L116A-85F dual mode automatic ellipsometer at Microtel Research in Discovery Park, Burnaby was available for use.

3.2.2 Ellipsometry: theory.

In ellipsometry one extracts information (thickness and optical constants) about a film on a substrate by measuring the polarization state of a beam of light of known polarization after it has been reflected from the film (Fig.3-4a). The state of polarization of a beam of light is characterised by the amplitude ratio and the phase difference between the two component plane waves of the electric vector into which the polarized oscillation may be resolved (one in the plane of incidence, p and the other in the plane perpendicular to it, s). In general, reflection causes a change in the relative phase of the two component plane waves and a change in the ratio of their amplitudes. Two angles called ellipsometric parameters denoted by and are usually defined: Δ is the change in phase of p and s components after reflection, and Ψ is the arctangent of the factor by which their amplitude ratio changes.

In conventional null ellipsometry (CNE) the ellipsometric parameters Δ and Ψ are usually determined by arranging a linearly polarized light to impinge upon the sample using a polarizer and finding an extinction of reflected light by observing through another polarizer called the analyzer. Δ and Ψ are simply related to the angles at which the polarizer and analyzer are to be positioned at a null[100]. Using Drude's theory, one can obtain a relation between Δ and Ψ in terms of the optical constants of the ambient N_0, film N_1 and the substrate N_2,

thickness d, angle of incidence ϕ, and wavelength λ of incident monochromatic light as[99]

$$\tan\psi\, e^{i\Delta} = \rho(N_0, N_1, N_2, d, \phi, \lambda) \qquad (3\text{-}1)$$

where ρ is a complex transcendental function which cannot be solved explicitly for d and N_1 but which can be satisfactorily handled by a computer.

In rotating analyzer ellipsometry (RAE), as in the case of the available instrument, the intensity of the reflected light is measured through the analyzer while it rotates. For light of any polarization incident on the rotating analyzer, the intensity of the transmitted light has the form (Fig.3-4b)

$$I(\theta) = I_0(1 + a\cos 2\theta + b\sin 2\theta) \qquad (3\text{-}2)$$

where θ is the angle between the transmitting axis of the analyzer and the plane of incidence, and I_0 is the average intensity for a full rotation of the analyzer[99]. The coefficients a and b represent all the polarization information that is available from the measurement and they can shown to be related to the ellipsometric parameters Δ and ψ as

$$a = \cos 2\psi \qquad (3\text{-}3)$$

and

$$b = \sin 2\psi \cos\Delta \qquad (3\text{-}4).$$

By Fourier transforming the intensity data from the rotating anlyzer one can obtain the coefficients a and b, and thereby

determine and using Eqn.3-3 and 3-4. These parameters can be used with Eqn.3-1 to determine the film thickness d and the optical constants resorting to numerical iteration routines by a computer[99].

3.2.3 Thickness measurement.

The Gaertner L116A-85F automatic ellipsometer is a rotating analyzer ellipsometer where a monochromatic 6328 A He-Ne beam of light is made to pass through a polarizer to give linearly polarized light. The beam is reflected from the sample which is placed on a levelled sample stage and is passed through another polarizer (analyzer) that can be rotated at constant speed (Fig.3-4b). A solid state photodetector measures the emerging light flux while the analyzer rotates, and a computer interfaced to the instrument acquires the data and performs the necessary calculations to extract the required parameters of the film.

The accuracy of the measurement is about +/- 3 $\mathring{A}$ while the repeatability is +/- 1 $\mathring{A}$. The speed of measurement is an impressive 30 seconds. A "thicness standard" of a SiO_2 film on Si is available for checking the instrument.

3.2.4 Metal evaporation.

The metal used for both contacts was aluminum, and was evaporated using a vacuum evaporator fitted with a liquid nitrogen baffle and an oil diffusion pump. An out of commission bell jar vacuum coater (Norton model 3115) was available for this study (Fig.3-5a). The complete system

including diffusion pump and electro-pneumatic valves was overhauled and restored to operational condition so that it was capable of achieving an ultimate pressure of 10^{-7} torr. A quartz-crystal-oscillator thickness monitor (Kronos model QM-310) was installed inside the bell jar enabling one to measure the thicknesses of deposited metal films with reasonable accuracy ($\pm$ 20 Å). Al was evaporated by placing the metal pellets on a suitable boat or wire basket and passing a high current through it to melt the pellets by ohmic heating. The silicon substrate on which the Al film is to be deposited is kept at about 30 cm above the boat, inside the vacuum to ensure a uniform deposition.

Since the fabrication of the MIS cells involved depositing a thin transparent metal layer followed by forming a contact finger pattern on the metal layer, it was desirable to evaporate both layers without breaking the vacuum to minimize contamination. To achieve this a sample holder with a rotating mask system that could be manipulated mechanically from the out side of the vacuum system was designed and mounted inside the bell jar. A mechanical shutter for controlling metal deposition on the sample was also installed between the source and the sample holder. The mask arrangement (Fig.3-5a and b) permits one to deposit three different patterns successively of the same metal, in addition to a fixed circular pattern, by evaporating the metal through them on to the sample placed on the holder. The masks which are made of Al disks (0.7 cm dia.) placed on slots machined on the holder to fit them snugly could be

easily interchanged.

3.2.5 The MIS fabrication.

Metal-insulator-semiconductor (MIS) solar cells of Al-SiO_2-pSi structure were fabricated on damaged and undamaged silicon samples following a similar procedure reported by Olsen et al,[101]. Whenever a cell was fabricated on a damaged sample, an undamaged sample also was subjected to the same fabrication process for comparison.

A thick layer of Al of about 1500 $\mathring{A}$ was first evaporated on to the back of the cell and was alloyed at 520° C, in a quartz tube placed inside the Lindberg furnace, to make a good ohmic contact. In the same step, a thin layer of SiO_2 was grown by passing high purity Ar and O_2, alternately, through the tube. Argon was, first, passed for 5 minutes, then O_2 for 5 minutes followed by Ar for another 5 minutes. Then, after turning off the furnace the sample was allowed to cool for about 30 minutes in Ar flow, at the end of the quartz tube. The thickness of the grown oxide layer was measured by the ellipsometer, and was found to be 17 +/- 3 $\mathring{A}$. Immediately, after the oxidation step, a thin layer of 99.999% pure Al of thickness of 50 A was evaporated on to the oxide from a tungsten wire basket in a vacuum of 10^{-6} torr. As the front contact, a 200 A thick finger pattern was then deposited on the metal layer, in the same pump-down cycle of the evaporator with the aid of the rotating mask. To maximize the reproducibility of the cells by limiting the number of

steps in the fabrication procedure no anti-reflection coating or contact pad were deposited. A Cu wire was attached to the back ohmic contact with silver dag for electrical connection as the final step of the cell fabrication procedure. A pointed end of a spring loaded phosphor bronze wire was employed to make electrical connection to the front contact. This procedure yielded MIS cells of good reproducibility. Their effective area was 0.37 cm^2.

3.3 I-V, C-V Measurement

The I-V measurement of a solar cell involves determining the current across the cell at a given voltage for a range of voltage between the front and the back contacts, which can be done either by point by point reading or by continuous ramping of the bias voltage. The latter method was selected in this study for convenience and speed. The differential capacitance of the cell also could be measured at the same time by superposing a small a.c. voltage on the d.c. bias voltage and using phase sensitive detection with the aid of a lock-in-amplifier.

3.3.1 Theory.

An electrical circuit for measuring the I-V characteristics fo the MIS structure was wired following one used for photoelectrochemical studies. The circuit diagram is shown in Fig.3-6a. The set up allows one to determine the capacitance of the MIS structure at a given frequency as

well.

Fig.3-6b shows the schematic of the relevant electrical circuit used for measuring the capacitance. The lock-in-amplifier measures the voltage across the small resistance R. Hence the a.c. current I, through the MIS cell, shown as an RC circuit, can be calculated by V_{LIA}/R and is equal to $V_{a.c.}/Z$ where $V_{a.c.}$ is the a.c. voltage across the cell and Z is the total impedence of the cell at that particular frequency (see section 2.4.2). Z is given by

$$1/Z = 1/R + jwC \qquad (3\text{-}5)$$

where $j = (-1)^{1/2}$, $w = 2 f$ and f is the frequency at which the measurement is carried out. Hence, I is given by

$$I = V_{a.c.}/R + jV_{a.c.}wC \qquad (3\text{-}6)$$

which can be rewritten as

$$I = I_{//} + I_{\perp} \qquad (3\text{-}7)$$

where $I_{//} = V_{a.c.}/R$ and $I_{\perp} = V_{a.c.}wC$. Hence, by measuring the component of current 90° out of phase with the d.c. voltage one can determine C by

$$C = I_{\perp} / wV_{a.c.} \qquad (3\text{-}8).$$

Measurements were carried out at a high frequency

(100 kHz) where the dispersion of capacitance due to the surface states is negligible. It turns out that the oxide capacitance C_{ox} also can be ignored compared to the space charge region capacitance C_{SCR} (see section 2.4.2). By parallel plate capacitance formula we obtain

$$\frac{C_{SCR}}{C_{ox}} = \frac{e_{ox}\, W_{SCR}}{e_{Si}\, d_{ox}} \sim 1500$$

for an oxide of thickness d_{ox} = 20 Å, where, e_{ox} and e_{Si} are the dielectric constants of the oxide and Si respectively. Consequently, the measured capacitance of the MIS structure can be justifiably approximated to that of the space charge region of the semiconductor.

3.3.2 Experimental.

An IBM personal computer was interfaced to the analog outputs of the DVM, the electrometer and the lock-in-amplifier via an A/D converter (Tecmar Labmaster) for acquiring and recording data. A versatile program (VIC.bas) written for photoelectrochemical work was suitably modified and were used to aquire, display and record data. This program allows one to acquire data from three analog outputs (channels) simultaneously and save them in a diskette. Eqn.3-8 is written into the program, so by providing the program with the actual values of the frequency, the area of the sample, and the a.c. voltage across the sample, the capacitance of the sample is

calculated and stored as $1/C^2$ vs. voltage along with corresponding I-V data which can be subsequently plotted on a HP plotter.

Once the cell was connected at the sample terminals as shown in Fig.3-6a the ramp was set to start from -1V to 1V with a 100 s period so there is no detectable hysterisis associated with the I-V measurement. Before connecting the sample, the lock-in-amplifier was zeroed in phase with the d.c. voltage in the resistor at its highest sensitivity (1 μV full scale) and then the detection was set to 90° out of phase with this at a suitable sensitivity. The a.c. voltage at 100 kHz across the sample was monitored and was set to a convenient value (5 mV) by adjusting the output of the oscillator. The I-V and C-V measurement was started by manually triggering the ramp while initiating data acquisition by VIC. bas program in IBM PC.

3.3.3 Light source and sample holder.

A 150 W Xe arc lamp (Oriel model 6253) was used as the source of illumination along with AM2 (Oriel) filter for correcting its spectrum to match that of the terrestrial solar illumination (Fig.3-7). A light tight housing was built to contain the sample holder and was coupled to the arc lamp via a mechanical shutter (Fig.3-8) so both the dark and illuminated characteristics of the sample could be measured. A pyroelectric detector with a chopper (Oriel model 7084 and 7509) was available for measuring the illuminating intensity. By adjusting the distance from the lamp to the

sample a convenient intensity comparable to standard solar cell measurement was obtained. Throughout the study the standard intensity used was 100 mW cm^{-2} (AM2) unless stated otherwise.

A small cryostat was designed so that the cell temperature could be varied continuously from room temperature to that of liquid nitrogen while illuminating it through a quartz window (Fig.3-9). The MIS cell is mounted on a thick Cu block inside the cryostat. The Cu finger which is in good thermal contact with the cell ensures that the cell temperature is kept constant during measurement. A chromel-alumel thermocouple embedded inside the Cu finger was used to monitor the cell temperature. The design of the cryostat allows it to be used for carrying out four-probe resistivity measurement with varying temperature as well.

3.4 Hydrogen Passivation

In an effort to study the effects due to two major parameters associated with dislocations, namely the linear density of recombination centers and the conductivity, the damaged samples were treated in an atomic hydrogen atmosphere at various temperatures. A plasma of atomic hydrogen was produced using a Tesla coil following Seager and Ginley[102]. The $H^{\bullet}$ radicals produced by the high frequency alternating field of the Tesla coil are very reactive and are considered as good candidates for making covalent bonds with the unsaturated dangling bonds on dislocations, thereby altering the above two parameters.

3.4.1 Experimental.

The dislocations were passivated in an apparatus shown schematically in Fig.3-10. The damaged samples to be passivated were introduced into the quartz tube after degreasing and cleaning. The tube was then evacuated and filled with ultra high purity (U.H.P. Linde) hydrogen. This was repeated several times to minimize the presence of contaminants in the system. The gases inside the tube were monitored with a quadrupole mass spectrometer. Then, the Tesla coil was turned on and the pressure of H_2 was adjusted until an optimum (reasonably homogeneous) plasma glow was obtained inside the tube. The tube furnace enveloping the quartz tube in the vicinity of the sample enabled control of the temperature at which the plasma hydrogenation of dislocations was carried out. A thermocouple placed between the outside wall of the quartz tube and the heater monitored the temperature. A typical passivation-run was carried out at a given temperature for 3 hrs, at the end of which the furnace was turned off and the samples were left to cool for a half an hour with the plasma on. Once the samples reached room temperature they were withdrawn from the tube, cleaned again and used in fabricating MIS cells.

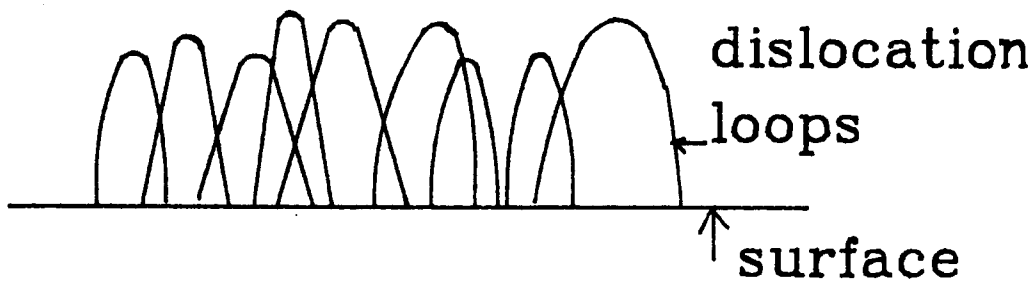

Fig.3-1 Dislocation loops near the surface.

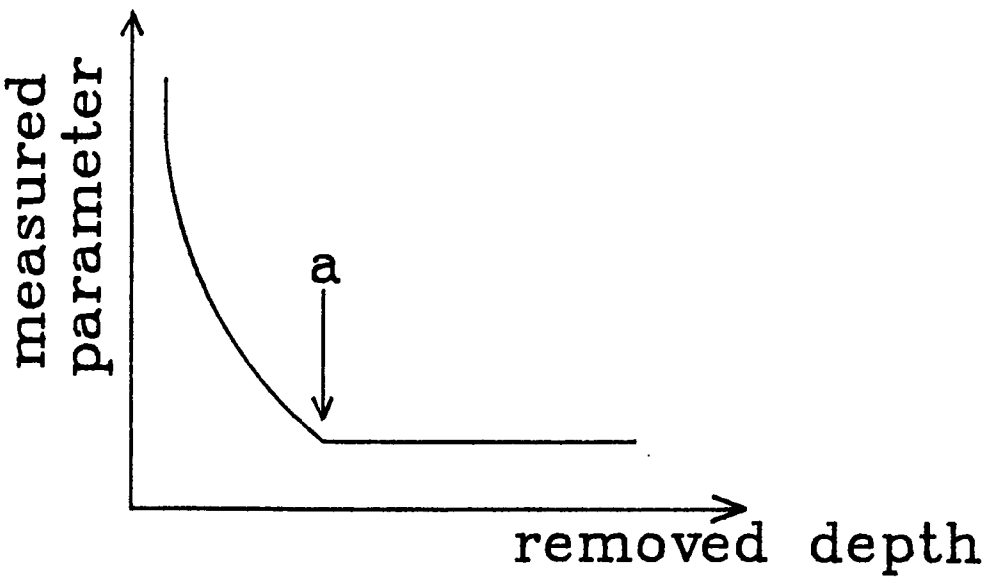

Fig.3-2 A plot of the measured 'parameter' versus the thickness of the incrementally removed layer. (The depth of the damage is indicated by point (a).)

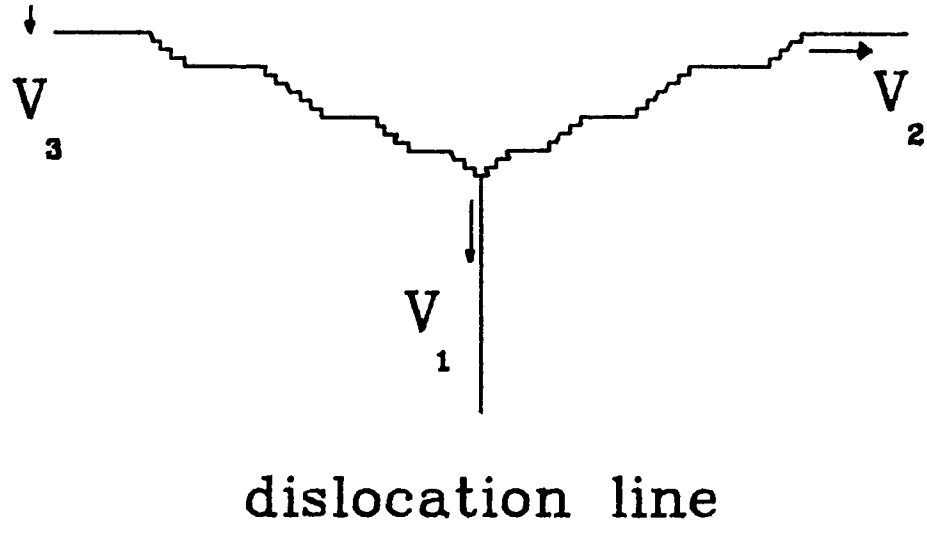

Fig.3-3 Formation of an etch pit at a dislocation due to preferential etching. The etching rates are different in different directions.

$V_2 > V_1 > V_3$

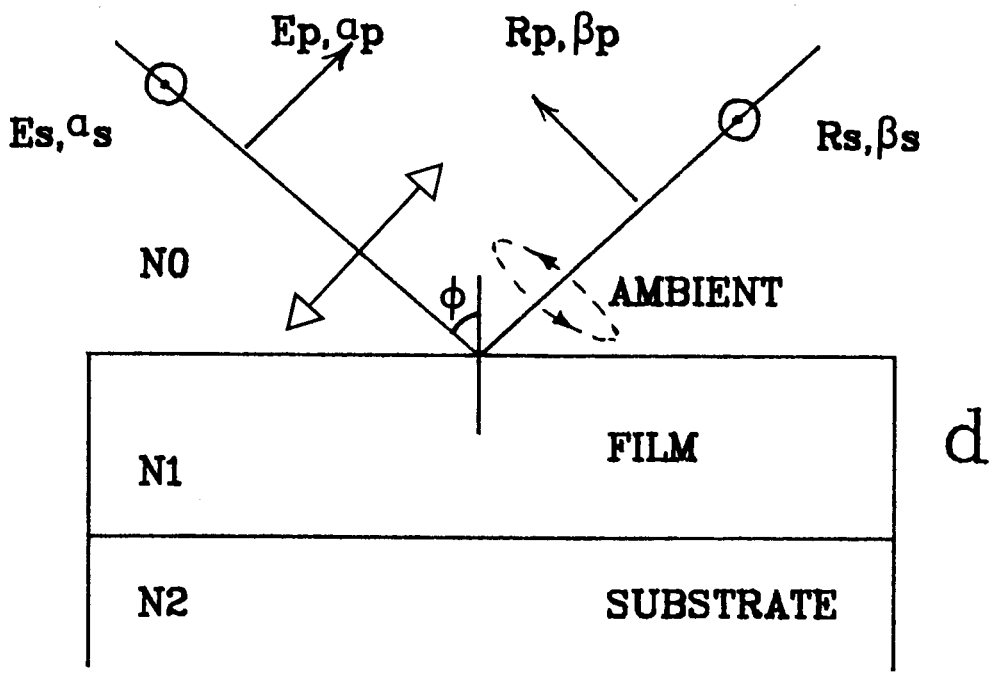

$$\Delta = (\beta_p - \beta_s) - (\alpha_p - \alpha_s)$$

$$\psi = \tan (Rp/Rs)/(Ep/Es)$$

Fig.3-4a Linearly polarized light reflected from a film on a substrate changes into elliptically polarized light. Ellipticity characterized by Δ and ψ carries information about the film.

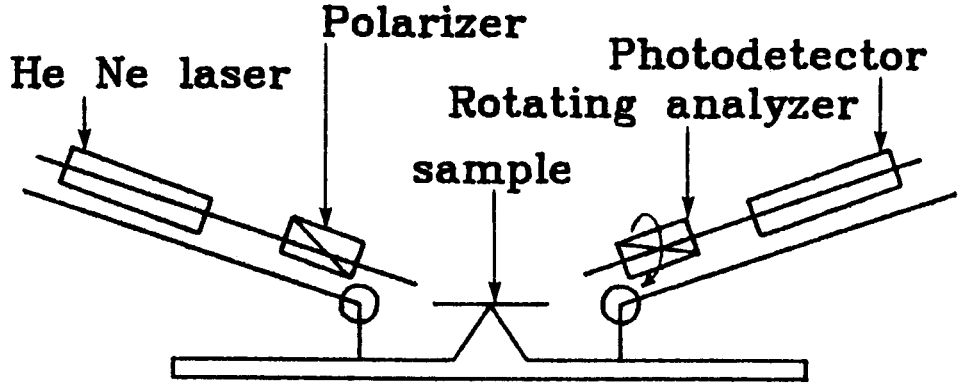

Fig.3-4b Schematic diagram of the rotating analyzer ellipsometer.

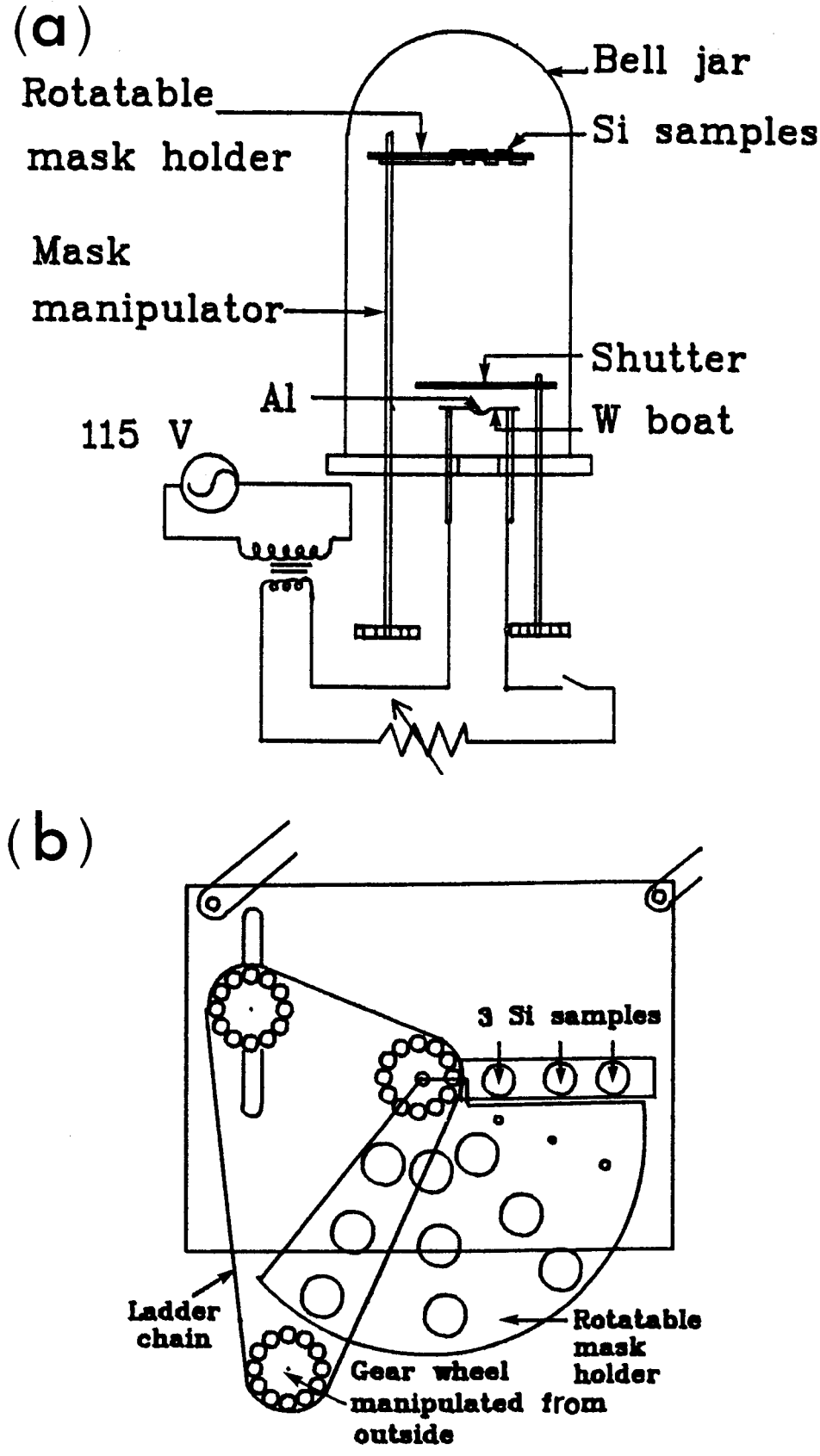

Fig.3-5 (a) Schematic diagram of the vacuum evaporator.
(b) The rotatable mask holder.

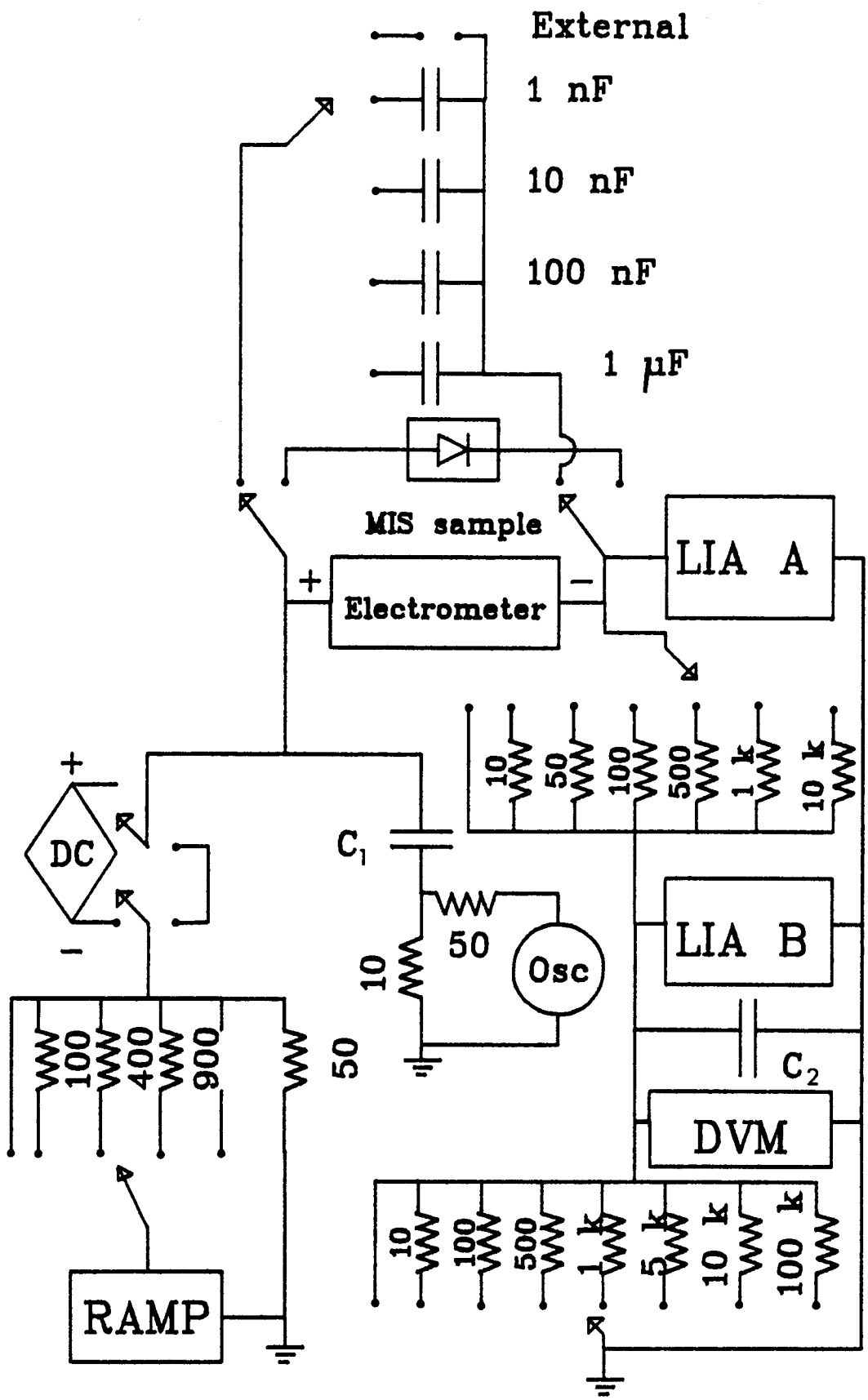

Fig.3-6a Schematic diagram of the electrical circuit used for measuring (I-V)/(C-V).
$C_1 = C_2 = 12.2 \mu f$

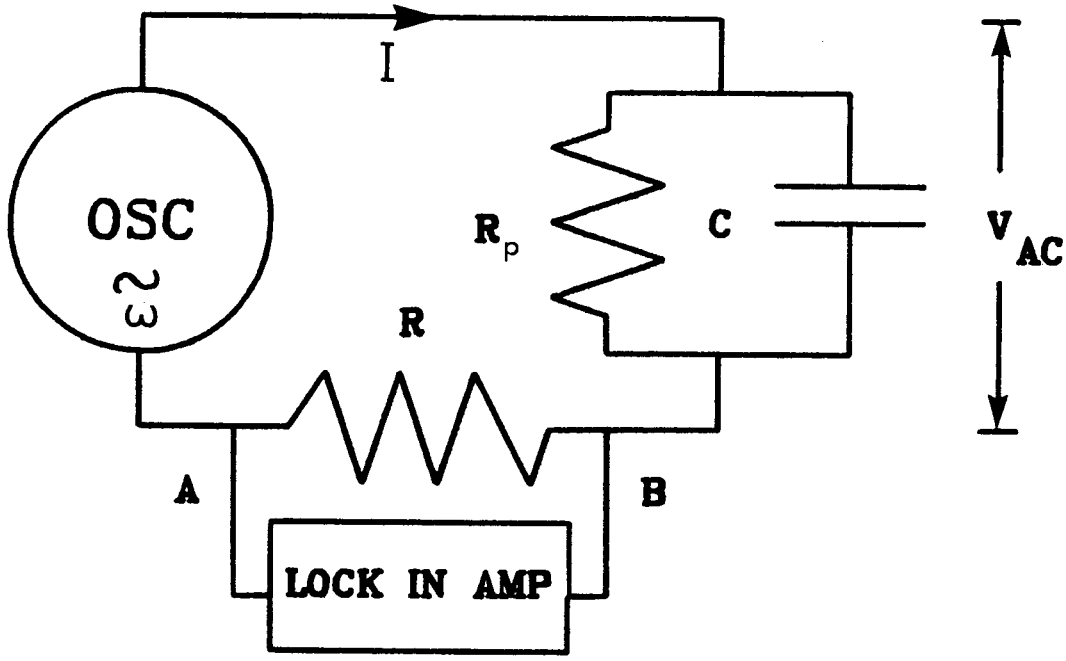

Fig.3-6b Measurement of capacitance with the lock-in-amplifier (LIA) at frequency f ($\omega=2\pi f$) with a constant $V_{a.c.}$ across the sample.

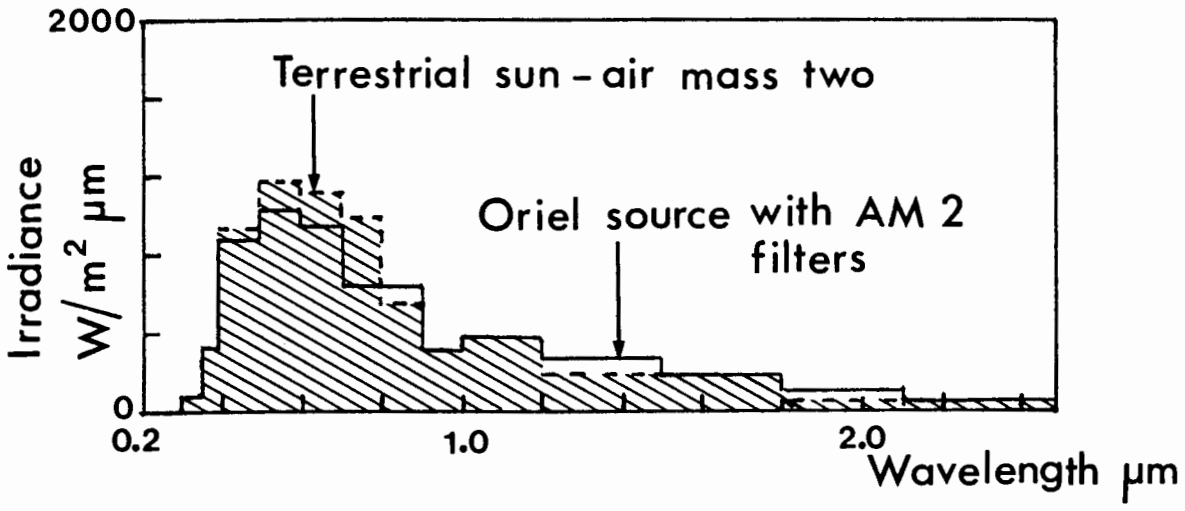

Fig.3-7 The spectral distribution of the Oriel light source compared to terrestrial sun (from the manufacturer of xenon arc lamp).

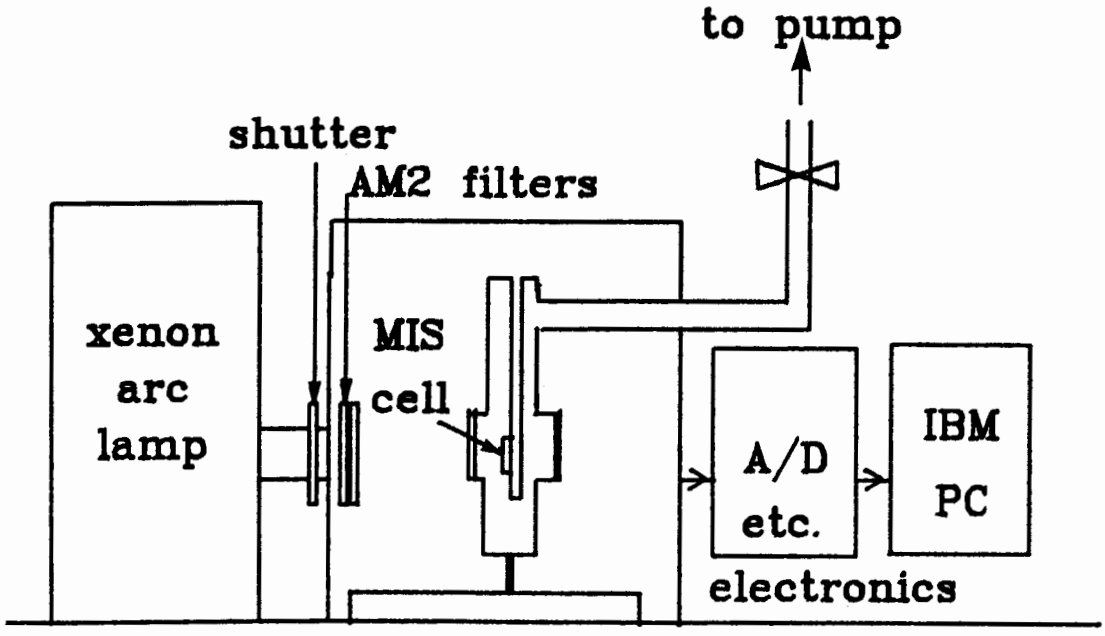

Fig.3-8 Schematic diagram of the system used for measuring the dark and the illuminated characteristics of MIS solar cells.

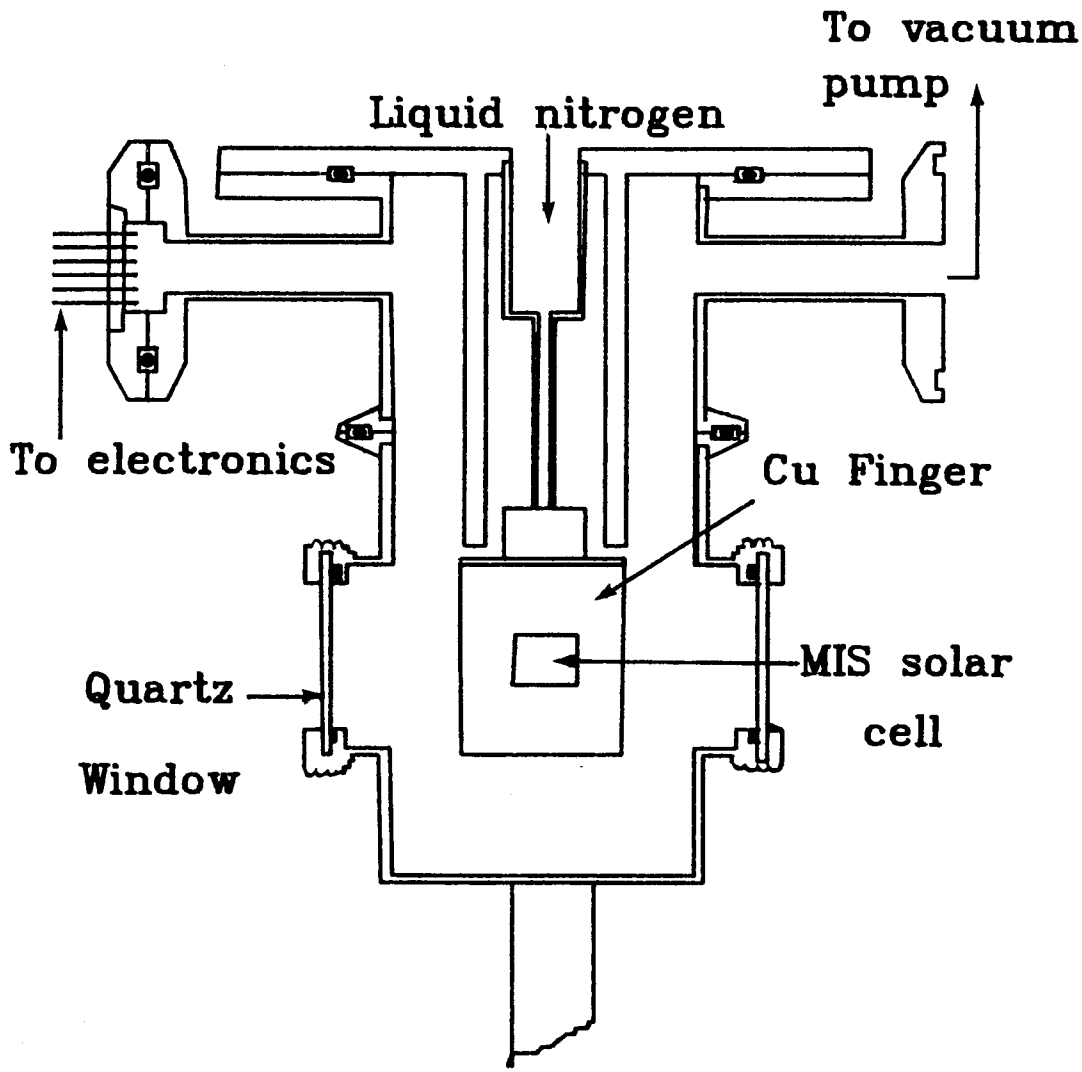

Fig.3-9 Schematic diagram of the cryostat.

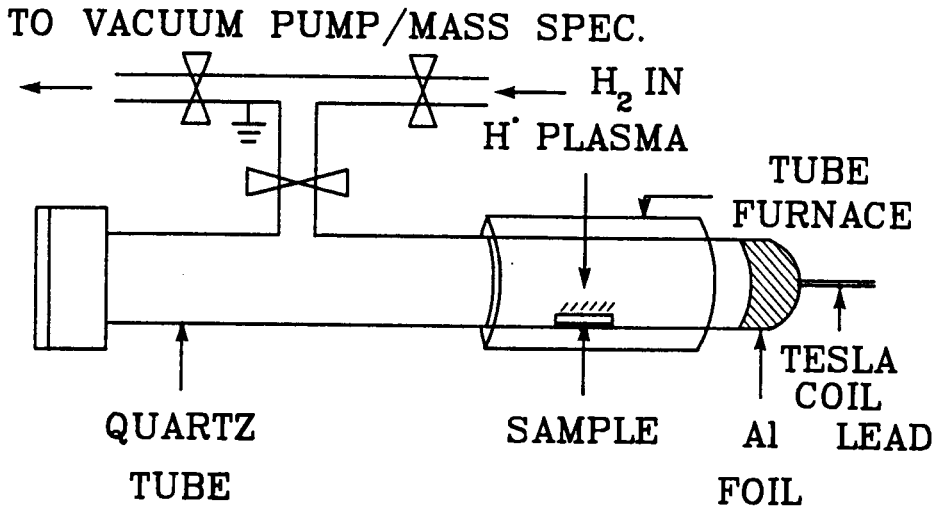

Fig.3-10 Hydrogen passivation apparatus.

CHAPTER IV

RESULTS AND ANALYSIS

4.1 MIS Cell Characteristics

4.1.1 Use of HF for etching

In the early stages of experimentation the top layer (5 μm) of the samples where possible unintended damage might be still present was removed by etching it away in an etchant called the planar etch. As its name indicates this etchant, composed of 8% HF, 17% HNO_3 and 75% acetic acid (all acids are in the concentrated form) in water, dissolves Si equally in all the crystallographic directions[103]. The etch rate was found to be about 4-5 μm/min for p-Si when the solution is stirred. However, the cells fabricated on such single crystal samples showed a rather large variation in J-V data. On close inspection the etched surfaces showed the formation of a thin, patchy, whitish layer that could not be removed or controlled by conventional chemical means. This has been observed previously by others too[104]. Use of clean Nalgene containers, teflon tweezers and deionized water (>15 mega ohm) did not alleviate the problem.

An elemental survey done with a Scanning Auger Microscope (model SAM-PHI-595) on a p-Si sample etched in the planar etch for 1 min showed that the white layer is associated with some kind of fluoride compound formation

(see Fig.4-1a and b) where fluorine was found to be absent on regions devoid of this layer. Even with new batches of acids, after some time in storage in the lab, this problem occured intermittently, although it was undetectable in the beginning. HF alone was never observed to form this type of layer. Hence it was decided to avoid use of the planar etch. It was found possible to do so, if great care was taken not to handle the top surface of the Si while cutting the samples. This could be achieved by the use of a watch glass to hold the samples while working with them, and taking enough care to handle the samples only from the edges with teflon tipped tweezers. For removing the native oxide prior to sample preparation 10% HF was used. The results of Fig.4-2a and b where we show the illuminated J-V characteristics for two batches of samples, one treated with the planar etch and the other treated with 10% HF, indicate the latter procedure yields superior quality samples.

4.1.2 Oxidation time

Since the effect of damage on the cell characteristics was to be studied we looked for a sample fabrication procedure that gives the maximum difference between a damaged and an undamaged sample. An initial experiment for finding such conditions was carried out. Four sets of MIS cells were prepared with both undamaged and damaged Si by oxidising them for various lengths of time at 500°C. The thickness of the oxide was measured

by ellipsometry on separate Si samples that were oxidised at the same time as the measured samples. The observed differences in the major solar cell parameters are indicated in Table 4-1. Oxidation as described in section 3.2.5 was seen to be the best and was used throughout the study.

4.1.3 General Cell Characteristics

The MIS structures fabricated in the manner described in section 3.2.5 yielded solar cells with following parameters: J_{sc} = 11.4 $\pm$ 1.3 mA/cm^2, V_{oc} = 527 $\pm$ 14 mV, FF = 0.7 $\pm$ 0.1 and η% = 4.1 $\pm$ 0.5 for illumination with AM2 spectrum at the intensity set to 100 mW/cm^2. J-V characteristics of a cell are shown in Fig.4-3 where both dark and illuminated cases are given. The variation of the short circuit current density, J_{sc} with illumination intensity is shown in Fig.4-4a and it indicates the conventional cell behavior. The variation of the other cell parameters with illumination (or with J_{sc} which is proportional to the intensity) is plotted in Fig.4-4b.

Using a photometer (Coherent Light) it was estimated that the reflection loss due to the metallised top layer of a cell is about 43%. If it is assumed that an anti-reflection coating would reduce the losses to a negligible level, a typical cell of ours without an anti-reflection coating would yield the following parameters: J_{sc} = 20 $\pm$ 2.3 mA/cm^2, η = 7.2 $\pm$ 0.9 %. This relatively low value obtained for the efficiency, even after correcting for the reflection

losses, indicates that there are several other loss mechanisms. One obvious possibility is the series resistance of the cell enhanced by the sheet resistance of the thin Al film, which usually depends on the evaporating conditions. In solar cells it is customary to employ metallized finger patterns to avoid high surface recombination velocity at the front contact, and the spacing between the fingers is typically in the order of 100 μm[83]. Referring to Fig.4-3b, where the top contact geometry of the MIS cell is shown, one can see that in this case the photogenerated minority carriers are not optimally collected at all. In addition to the above factors the low efficiency can also be attributed to the high surface recombination velocity at non-optimised surface states or at the perimeter of the front metal layer where the induced junction beneath it intersects with the surface. The latter has not been isolated by a thick oxide as well.

The Mott-Schottky plot of a typical cell is shown in Fig.4-5 where the capacitance was measured at 100 kHz. Its intercept yields a value of 0.80 eV. The slope indicates a doping level of $N_A = 3 \times 10^{15}$ cm^{-3}. Due to the possible inversion at the surface the intercept can not be used to determine the barrier height. However, it can be used to determine whether the surface is in fact inverted. The value of the surface potential needed for driving the semiconductor to inversion for this doping level is 0.61 eV calculated by Eqn.2-21. Since the measured surface potential from the Mott-Schottky plot is greater than this

the semiconductor is found to be inverted as suggested by the work function differences.

4.1.4 Damaged Samples

A set of illuminated J-V characteristics of a series of damaged samples are shown in Fig.4-6a. Results for samples with dislocations of varying lengths (grit size used) from 0.05 μm to 1 μm, as well as an undamaged cell are shown. Table 4-2 gives the major cell parameters averaged over a large number of samples. All the cell parameters, viz, the open circuit voltage, V_{oc}, the short circuit current, J_{sc}, the fill factor, FF, and the efficiency, η are observed to be progressively degraded with increasing grit size. A more interesting result is seen when one examines the J-V characteristics at reverse bias. It is found, of course that minority carrier generation at the dislocations leads to excess dark current at reverse bias. Allowing for this, subtracting the dark current from current under illumination, it is found that the resulting "saturation photocurrent" is independent of the presence or length of the dislocations. Fig.4-6b shows the net photocurrent of these samples versus reverse bias in a blown-up scale to bring out the details (the origin of the net J_{ph} axis is not zero but 10 mA cm^{-2}).

The range of grit sizes we have used in this study makes it possible to have dislocation loops which remain inside (0.05 μm), or span across (0.1 μm - 0.3 μm), or extend well beyond (1 μm) the space charge region. In the

undamaged samples, the width of the SCR, W_{SCR} was estimated by Eqn. 2-20 and was found to vary between 0.5 μm and 0.8 μm from zero bias to reverse bias at 1V, respectively, using reverse bias capacitance data at high frequency. With surface damage, the measured capacity was three to four times higher, indicating a substantially thinner space charge region due to the added centers. However, a quantitative interpretation of the capacity for a damaged sample is difficult.

Another experiment was carried out by successively etching a 1 um damaged sample and fabricating an MIS cell at the end of each etch. In Fig.4-7 the results of this experiment is shown where the 10% HF was used for 20 s for each etch. The gradual improvement of the cell characteristics can be interpreted in terms of the changes in the surface region (including the space charge region, SCR) which is affected by the chemical treatment. It is well established that the electrical activity of a surface is quite sensitive to even a minor chemical treatment[89]. The surface recombination velocity at surface states, as well as SCR recombination-generation rate is influenced by such treatments. Gradual decrease in the generation current associated with the surface states in the SCR explains the behavior of J-V curves in Fig.4-7. This shows that one should use different lengths of dislocations rather than different densities of dislocations to extract their electrical effects since the surface effects can presumably be kept constant by giving identical chemical

treatments to samples of various damage sizes.

4.2 Density of dislocations

The average value of the density of dislocations, D_{DL} determined by counting etch pits after treating the damaged samples with Dash etch is also given in Table 4-2. The values obtained for both 0.05 μm (average of 7 samples) and 0.3 μm (average of 10 samples) cases seem to be roughly equal although the standard deviation of the latter is relatively larger. It is difficult to explain this similarity. Two scanning electron micrographs indicating the nature of the observed etch pits are shown in Fig.4-8. The sample shown in Fig.4-8a has been treated with the Dash etch for 20 s while that in Fig.4-8b has been etched for more than 1 min. The undamaged samples were free of etch pits.

These two micrographs show the importance of the etching time. As the results indicate, D_{DL} was found to be in the order of 10^9 cm^{-2} in all the samples measured increasing somewhat with increasing grit size used for lapping.

4.3 ANALYSIS AND MODEL

As seen in the experimental data, under reverse bias, even in the 1 μm damaged case the photocurrent is only moderately affected (Fig.4-6b). By comparison, in TiO_2 samples the photocurrent is reduced by two orders of magnitude in the presence of even less surface damage (0.3 μm)[97]. The insensitivity of the photocurrent to the length

of the defects suggests that there is a mechanism which dominates over the simple recombination at these defects, for if simple recombination were the dominant effect of the dislocations then the saturation photocurrent would decrease as well as the other solar cell parameters.

4.3.1 Recombination model

The inadequacy of the standard recombination mechanism for explaining the reverse bias data can be shown for the special case of the 1 μm damaged case by a simple analysis of the photocurrent in terms of Shockley-Noyce-Sah (SNS) theory[82]. The inversion layer makes the analysis simpler since the structure can be treated like a n^+p junction in the bias range of interest. However, the exact nature of the front contact is not important to see the effect of recombination on the photocurrent at reverse bias. The standard diode theory can be applied assuming the MIS structure can be represented by a one-sided-junction (see Appendix I) where recombination is described in terms of a suitable minority carrier life time.

Instead of a uniform semiconductor the sample can be considered to be composed of two different regions: one, containing the damage, extending a length ℓ from the surface, characterised by a minority carrier life time, t_d, and the region beyond ℓ, the bulk or the undisturbed material with a different but higher life time t_b ($t_d \ll t_b$). One has to account for the recombination in the damaged region beyond the space charge region (SCR)

when calculating the photocurrent since the width of the SCR in the bias range of interest is less than the the depth of damage when ℓ = 1 μm. In addition to that, both thermal and photo generation in the SCR also have to be taken into account (see Appendix I for details).

The resulting curves of the photocurrents of a 1 μm damaged and an undamaged sample are shown in Fig.4-9 where for simplicity a constant generation of electron-hole pairs has been assumed. The minority carrier life time in the damaged region (t_d) was estimated by fitting the dark current data with the SCR generation component as shown in the Fig.4-9.

The results indicate clearly the photocurrent should be very sensitive to damage if recombination is the dominant effect in the samples. Of course, the curves can not be directly compared with those obtained experimentally since the calculations are based on constant photogeneration. However, it is evident from the shape and the magnitude of the calculated photocurrent that the defect states at the dislocations should strongly reduce the photocurrent if the carriers were only to be recombined at them. This is quite contrary to the experimental observations in Fig.4-6a and b.

4.3.2 Dislocation Conductivity Model

It will be shown that conduction of captured carriers along the dislocation levels provides a good explanation of experimental results[105]. For mathematical convenience, the dislocation loops are replaced with a uniform distribution of dislocation lines running perpendicular to the surface of Si (Fig.4-10a). The dislocations introduced to the sample will undoubtedly have a certain distribution with respect to their lengths. As discussed in section 3.1.1, experiments have shown that the effect of dislocations (on IR reflectivity, chemical etch rate, conductivity, x-ray line broadening and photomagnetoelectrical voltage) disappears when material is etched away to a distance ℓ where ℓ is the diameter of the particles used to produce the dislocations. For lack of a better value for dislocation length we have used the same value ℓ as the effective depth of penetration. Since we are not expecting a rigorous agreement between the model and experiments (see discussion in section 4.3.3.) this approximation should be satisfactory. The surface distribution of the dislocations is also assumed to be uniform for the simplicity of calculations even though the actual case is seen to be somewhat different from that (Fig.4.8a).

Fig.4-10b shows the band diagram of the cell with a dislocation, with the plane of the paper parallel to the dislocation, where for clarity, the insulator layer is not shown. It is known that dislocations in p-type materials have

donor levels in the band gap, which we will call the defect levels. Hence, a dislocation can capture holes producing a positive line charge, which is compensated by a negative charge in a cylindrical space charge region around it. Fig.4-10c is the cross sectional diagram at AB of Fig.4-10b, viewed perpendicular to the surface.

The model of Fig.4-10 thus includes a single level of localized states, due to the dislocations, denoted by E_t, assumed to be near mid gap. E_v and $E_{v,d}$ are the valence band edges of the bulk semiconductor and the dislocation, respectively. E_{FM} and E_{FS} are the Fermi levels of the metal and the semiconductor, respectively. E_i is the depth of the defect levels given by $E_i = E_t - E_{v,d}$. V_o is the output voltage of the cell given by $V_o = (E_{FM} - E_{FS})/q$. Electrons from the conduction band and holes from the valence band can be captured at the defect levels. As indicated both in Fig.4-10b and 4-10c holes have to be activated over a barrier of magnitude $(E_v - E_{v,d})$ to be captured, while the electrons as the minority carriers do not. Further, we assume that there is a certain conductivity along the dislocation so carriers can move along the potential gradient which is established by the carrier movement itself. Using Ohm's law to describe this, we obtain

$$J_d(x) = -s(dV_d(x)/dx) \qquad (4-1)$$

where, J_d is the electron current (in amperes) along the

defect levels and V_d is given by, $V_d = (E_t - E_{FM})/q$. Here s, the specific conductance of the dislocation which is assumed to be constant over the length of the line defect, has units of cm ohm^{-1}. The bending of the levels on the dislocation as a function of x as sketched in Fig.4-10b is described by equation (4-1). In sketching Fig.4-10b we assume the density of trap levels at the dislocation is high enough that carrier exchange with the metal makes the trapping level at the surface isoenergetic with the metal Fermi energy ("pins" the Fermi level) as shown. The double layer formed by this carrier exchange, a few tenths of angsrtoms thick, is not shown in Fig.4-10b.

The equation of continuity of carriers yields another relation, namely

$$dJ_d(x)/dx = -qk_p p_d \qquad (4-2)$$

The gradient of the current along dislocation is equal to the net rate of carrier capture on the defect levels. In Eq.(4-2) we indicate only the majority carrier (hole) capture and neglect the capture of electrons along the dislocation. This is partially justified by the fact that the photoproduction of electrons in the damaged region of the sample, which has a maximum dimension of about 1 μm, is negligible in comparison with photoproduction over a distance of a minority carrier diffusion length (L ~ 100 μm). For simplicity of the analysis we make the

approximation that all electron capture occurs at the tip of the dislocation, and any electrons not captured at the tip will reach the metal in the defect free area between dislocations. With this approximation there will be a quantitative error in the results, but qualitatively the J-V curves will not be significantly altered. In Eq.(4-2), k_p is a rate constant given by

$$k_p = c\ \sigma_p p_u \qquad (4-3)$$

where c is the thermal velocity of the holes, σ_p is the capture cross section of the traps for holes, and p_u is the density (per unit length) of the traps occupied by electrons (or unoccupied by holes). p_d in Eq.(4-2) is the density of holes in the valence band at the dislocation, given by

$$p_d = p_b \exp(-qV/kT) \qquad (4-4)$$

where p_b is the density of holes in the bulk silicon and V is given by inspection of Fig.4-10b.

$$V = (E_v - E_{v,d})/q \qquad (4-5)$$

Also by inspection (Fig.4-10b), we obtain a relation between V and V_d

$$E_i = q(V + V_o + V_d) + \mu \qquad (4-6)$$

where μ is $E_{FB} - E_V$,

The differential equations (4-1) and (4-2) describe the model and we have two boundary conditions. First, as mentioned above we assume that there is a high enough density of states in the defect levels that the Fermi level of the metal is pinned to the dislocation level at the surface, i.e., at $x = 0$. Hence, the first boundary condition is that (Fig.4-10b)

$$\text{at } x = 0 \; ; \; V_d(x) = 0 \qquad (4\text{-}7)$$

Next, the simplifying assumption that all electron capture takes place at the tip of the line defect, provides the second boundary condition. Since the photocurrent is the same for the damaged and the undamaged cells the magnitude of the electron (minority carrier) current density at $x = -\ell$ is the same as the photocurrent density (J_{ph}) of the undamaged cells. If the dislocation space charge region (DSCR) has a radius of r, then we have

$$J_d(x=-\ell) = \pi r^2 J_{ph} \quad (= I_p, \text{ say }) \qquad (4\text{-}8)$$

as the second boundary condition. In our calculations, r is assumed to be 0.15 μm[27]. Using the boundary conditions given by (4-7) and (4-8), the differential equations (4-1) and (4-2) are solved for $J_d(x)$. Assuming that the electrons can

communicate with the metal readily through the 20 Å thick insulating layer we can calculate the contribution to the photocurrent from one dislocation (J_{d1}) by evaluating $J_d(x = 0)$ as follows.

Substituting for $J_d(x)$ in (4-2) by (4-1) and eliminating V using (4-6) yields

$$d^2V_d(x)/dx^2 = 2\beta K \exp(\beta V_d(x)) \qquad (4\text{-}9)$$

where $K = (qk_p p_b/2\beta s)\exp(-(E_i - \mu)/kT)\exp(\beta V_D)$ and $\beta = q/kT$. By multiplying (4-9) with $(1/2)(dV_d/dx)$ and integrating, we obtain

$$(dV_d/dx)^2 = K\exp(\beta V_d) + C \qquad (4\text{-}10)$$

where C is an integration constant.
Eqns. (4-1) and (4-10) yield

$$J^2_d(x) = s^2K\exp(\beta V_d(x)) + s^2C \qquad (4\text{-}11).$$

We had the boundary conditions (4-7) and (4-8). Writing $J_d(x)$ at $x = 0$ as J_{d1}, we obtain

$$J_{d1} = \pm s\,(B\exp(\beta V_D) + C)^{1/2} \qquad (4\text{-}12)$$

where $B = (qk_p p_b/2\beta s)\exp(-(E_i - \mu)/kT)$. C can be evaluated using the second boundary condition, Eqn. (4-8). First, we should evaluate $V_d(x = -\ell)$, which can be obtained from

solving (4-10). Rearranging Eqn. (4-10) and integrating, we have

$$\int \frac{dV_d}{\sqrt{K\exp(\beta V_d) + C}} = \pm x + D \qquad (4\text{-}13)$$

where D is another integration constant. The LHS of (4-13) depends on the sign of C. Eqn. (4-12) which can be rearranged as

$$C = (J^2_{d1} - s^2K)/s^2,$$

clearly shows that C can be either negative or positive depending on whether J^2_{d1} is less or greater than s^2K.

Case I.

If C > 0, integral of the LHS of Eq.(4-13) yields

$$\frac{1}{\beta\sqrt{C}} \ln\left[\frac{\sqrt{K\exp(\beta V_d) + C} - \sqrt{C}}{\sqrt{K\exp(\beta V_d) + C} - \sqrt{C}}\right] = \pm X + D \qquad (4\text{-}14)$$

Using the first boundary condition (4-7), we evaluate D and the second boundary condition (4-8) then yields

$$Ip^2 = s^2C\left[\frac{(\sqrt{K + C} + \sqrt{C})^2 + K\exp(\pm\beta\sqrt{C}\ell)}{(\sqrt{K + C} + \sqrt{C})^2 - K\exp(\pm\beta\sqrt{C}\ell)}\right]^2 \qquad (4\text{-}15)$$

which can be used to evaluate C, numerically.

Case II.

If C < 0, the integral of the LHS of Eqn. (4-13) yields, with C = abs(C),

$$\frac{2}{\beta\sqrt{C}} \tan^{-1}\sqrt{\frac{K\exp(\beta V_d) - C}{C}} = \pm x + D \qquad (4\text{-}16)$$

Using (4-7) and (4-8) as before, we obtain

$$J^2_p = s^2 C \tan^2 (\theta \mp \beta C \ell/2) \qquad (4\text{-}17)$$

where $\theta = \tan^{-1}((K - C)/C)^{1/2}$. Eqn. (4-17) also can be solved numerically, for C which in turn can be used in Eqn. (4-12) to calculate J_{d1}. When C = 0 we get the limiting value of both cases.

With the above equations one can calculate the values of C and insert it in Eqn. (4-12) to obtain J_{d1}, the current reaching the surface through the dislocation, as a function of voltage V_D.

The total current of the cell can be thought of as being comprised of two components, the current along dislocations, and the current supported by the undisturbed regions of the sample. The latter component can be

described, by the ideal single crystal solar cell J-V characteristics that can be expressed in terms of the photocurrent density J_{ph} and the reverse saturation dark current density J_{od}. Then the current density J_b of an undamaged cell is

$$J_b = J_{ph} - J_{od}(\exp(qV_o/kT) \qquad (4\text{-}18)$$

Then the total current density, J can be expressed as the sum of the current through dislocations and current associated with the undisturbed region.

$$J = J_{d1}D_{d1} + aJ_b \qquad (4\text{-}19)$$

where a is a geometrical factor which represent the effective area for the current in the undisturbed region of the cell and D_{d1} is the density of dislocations.

4.3.3 Results and discussion

Several simplifying assumptions were made in order that the model be analyzable relativley easily, namely, a) actual dislocation loops can be approximated by a uniform distribution of line defects whose lengths are comparable to the size of the particles used for lapping the samples, b) the dislocation states in the band gap can be represented by a single level, c) the Fermi energy of the metal is pinned to that of the dislocation states at the surface, d) the capture of the electrons (minority carriers) predominanatly occurs at

the tip of the line defect, and e) the insulating layer is thin enough so that it does not pose any hindrance to the carrier transport across it. Considering these assumptions one expects the model to yield qualitative aggreement with the experiments at best.

Figs. 4-11 to 4-14 show the numerical solutions of Eqns.(4-15,17,12,18 and 19). The variation of J_{sc} with the length of dislocation (ℓ) is shown in Figs. 4-11a and b where the parameter ($E_i - \mu$) is assumed to be 0.3 and 0.5 eV, respectively. The other parameters used in the calculations are given in Table 4-3. Figs.4-12a and b show the effect of the specific conductance on the J-V characteristics for a fixed length of dislocations, namely, = 1 μm.

The total J-V characteristics of the MIS cells for the cases shown in Figs. 4-11 and 12 are indicated in Figs. 4-13 and 4-14, respectively. The Eqn.(4-19) was used to add the contribution of defects and the contribution of defect free regions. Figs.4-15a and b show the cell parameters obtained from the calculations for various lengths of dislocations when $(E_i - \mu) = 0.3$ eV and $s = 1 \times 10^{-15}$ cm ohm^{-1}. The experimental data given in the Table 4-II are also plotted for comparison.

Figs. 4-16a and b show the calculated variation of the cell parameters with D_{sc} for the case of when $\ell = 1$ μm.

The J-V characteristics obtained from the model by varying the length of the dislocations show the strong effect of the surface damage on V_{oc} and FF (Figs. 4-11a and

b). Furthermore, it is evident from Figs. 4-11a,b and 4-13a,b that the saturation photocurrent (at reverse bias) is actually independent of the length although it is not completely shown in the figures the case of ℓ = 1 μm is the same.

The fact that the reverse saturation photocurrent of the cells damaged using various grit sizes does not depend on the grit size (the depth of the damage) is a very important observation from the experiments. If recombination were the important role of the dislocations in degrading the diode, the saturation photocurrent would be affected as much as the open circuit voltage. As demonstrated in the mathematical model of the photodiode for this special case of a thin layer of surface damage, if conductance and shunting is the important role of dislocations, the saturation photocurrent is unaffected while V_{oc} is strongly affected. Because the latter agrees with experimental observations, we believe that this constitutes a piece of compelling evidence in favor of conduction along dislocations.

In the case of conducting dislocations the model shows why the recombination of minority carriers captured by the dislocations should increase with the length of the line defects ℓ, under forward bias and be negligible under reverse bias. This behavior is exactly what we observe experimentally and arises due to the fact that once the minority carriers (electrons) are captured at the dislocations, their movement along the defects under reverse bias permits them to reach the surface. However, the

majority carrier capture on the dislocations is exponentially dependent on voltage, and with a forward biassed diode, will recombine before they reach the surface. This will lead to a low V_{oc} and FF. If the distance ℓ that the minority electrons have to traverse before reaching the surface is long, then, their likelihood of being recombined increases, and V_{oc} and FF worsens.

The effect of the parameter $(E_t - \mu)$ is readily seen in Figs. 4-11 to 4-14: E_t is the depth of the defect levels (or dislocation states) and μ is the difference between the Fermi level and the top of the valence band of p-type silicon. A sensitive variation of the current along the line defects with E_t should be expected since according to the model the hole capture at the defect level varies as $\exp(-(E_t - \mu))$ at a given bias (see equations (4-2, 4-4 and 4-6)). Hence lowering $(E_t - \mu)$ should increase recombination of electrons at the dislocations giving rise to a lower J_{d1} at a given bias. This behavior is, in fact, discerned by examining Figs. 4-11a and 4-11b. Comparing the experimental results (Fig. 4-6a) with the theoretical curves (Figs.4-13a and b showing the calculated total J-V characteristics) one observes that $(E_t - \mu) = 0.3$ eV is more favorable for an agreement between the model and data than 0.5 eV. The acceptor density of the samples being 3×10^{15} cm^{-3}, the value of μ, calculated by $\mu = (kT/q)\ln(N_v/N_A)$ is 0.2 eV where N_v is the effective density of states in the valence band of Si. Consequently, the depth of the dislocation

levels, E_t is found to be 0.5 eV. This value of E_t compares very well with the value reported by Mantovani and Pennino[37] who studied the reverse bias dark current of Schottky diodes prepared on dislocated p-Si. They report that the dislocations introduced by bending the samples have most effective energy level for the generation/recombination process at 0.52 eV above the top of the valence band.

The effect of the specific conductance, s on the cell characteristics is also relatively strong as clearly indicated by the various curves in Figs. 4-12a, b and Figs. 4-14a, b. As it has been assumed in the model, the minority carriers can still reach the barrier even when they are captured at the dislocations and the magnitude of the current should depend on the conductivity of the line defects. Figs. 4-12a and b reflect this behavior. Comparing the experimental J-V curve for 1 um damage (curve e in Fig. 4-6) with those in Figs. 4-14a or b one can infer that a value of the order of 10^{-15} cm ohm^{-1} for s would give the closest agreement between calculations and observations. As mentioned earlier in section 2.2, the only value of s available in the literature is 10^{-10} cm ohm^{-1} at 4.2 K which was estimated by Labusch[13]. The value of s at the room temperature estimated by fitting the model to the J-V data is lower than that at low temperature.

The calculated variation of the cell parameters (J_{sc}, η, V_{oc} and FF) agrees quite well with that observed experimentally as indicated by Figs. 4-15a and b

when $s = 1 \times 10^{-15}$ cm ohm^{-1} and $(E_i - \mu) = 0.3$ eV. The only deviation seen in these results is when $\ell = 1$ μm where V_{oc} and FF are significantly larger than the experimental values. The fact that the results for the largest ℓ are affected in forward bias suggests that the simplifying assumption used in calculations where the electron capture along the line defect was ignored except at its end ($x = -\ell$), could be responsible for this. Apart from this minor deviation the simple model adequately describe the effect of dislocations.

The shunt current as expressed by Eqn. (4-12) indicates an exponential dependence with the bias, contrary to the generally believed linear dependence. It is of interest that the effective quality factor of photodiodes dominated by conduction along dislocations will be greater than two, according to Eq.4-12.

Calculated dependence of the cell parameters with the density of dislocations, D_{d1} shows that, as expected, they degrade with increasing D_{d1}. However, it is most interesting to note that there is no significant deterioration when $D_{d1} < 10^4 - 10^5$ cm^{-2}. This behavior closely agrees with what is observed in practice by other authors[59,106].

A solar cell is usually represented by an equivalent circuit involving a diode in parallel with a resistance (shunt resistance, R_{SH}) and in series with another resistance (R_S). A current source parallel to the diode is used to indicate the photogenerated current under illumination. The

R_{SH} and the R_S are generally estimated by inverse slopes of the current-voltage characteristics of the cell as $R_{SH} = (dI/dV)^{-1}$ at $V >> 0$ and $R_S = (dI/dV)^{-1}$ at $V << 0$. One must have the $R_S = 0$ and $R_{SH} \rightarrow \infty$ for an ideal solar cell. Either a large R_S or a lower R_{SH} degrades the fill factor yeilding a poor cell. The R_S alone does not affect the open circuit voltage (V_{OC}) although it will affect the short circuit current (J_{SC}) while the R_{SH} alone does not influence J_{SC} although it will influence the V_{OC}. It seems at a glance that a combination of both R_S and R_{SH} may produce the degradation observed in the J-V data. However, when the effect of R_S and R_{SH} on J-V characteristics (as calculated by several authors[85]) is examined it shows that unrealistically low shunt resistance (of several ohms instead of several hundred killo ohms indicated by the slope of the reverse biased characteristics measured) and a very high series resistance (of several hundred ohms as opposed to just several ohms indicated by the slope of the forward biased characteristics measured) are needed together to bring about the changes in V_{OC} and J_{SC} concurrently as in the experiments. Thus, the data can not be explained in terms of such an equivalent circuit with any physical significance. On the other hand, the dislocation conductivity model explains the variation of the J-V data at a more fundamental level where one can directly relate the parameters involved to the structure.

4.4 Conclusions

The J-V characteristics of the MIS cells

fabricated on p-type Si containing dislocations of various lengths, showed that all of the cell parameters were progressively degraded with increasing penetration of these line defects into the sample. However, the reverse saturation photocurrents were observed to be independent of the depth of the damage. This combination suggests the degradation is due to conduction of captured carriers along the dislocation levels in the band gap. A simple model presented, assuming a certain conductivity along the dislocations, is used to explain the experimental data. The J-V characteristics calculated using the model seem to be very sensitive to the specific conductance, s of the dislocations. An estimate of the value of s was made by fitting the theoretically calculated curves with the experimental curves. For the type of dislocations studied, s could be estimated to be about 10^{-15} cm ohm^{-1}. To our knowledge, this is the first time that such a conductivity has been observed in a solid state semiconductor device at room temperature[105]. It is of interest to note that the model predicts that with dislocation densities less than about 10^{5} cm^{-2} or so, there is no significant degradation due to dislocations, which agrees quite well with the observations made by others.

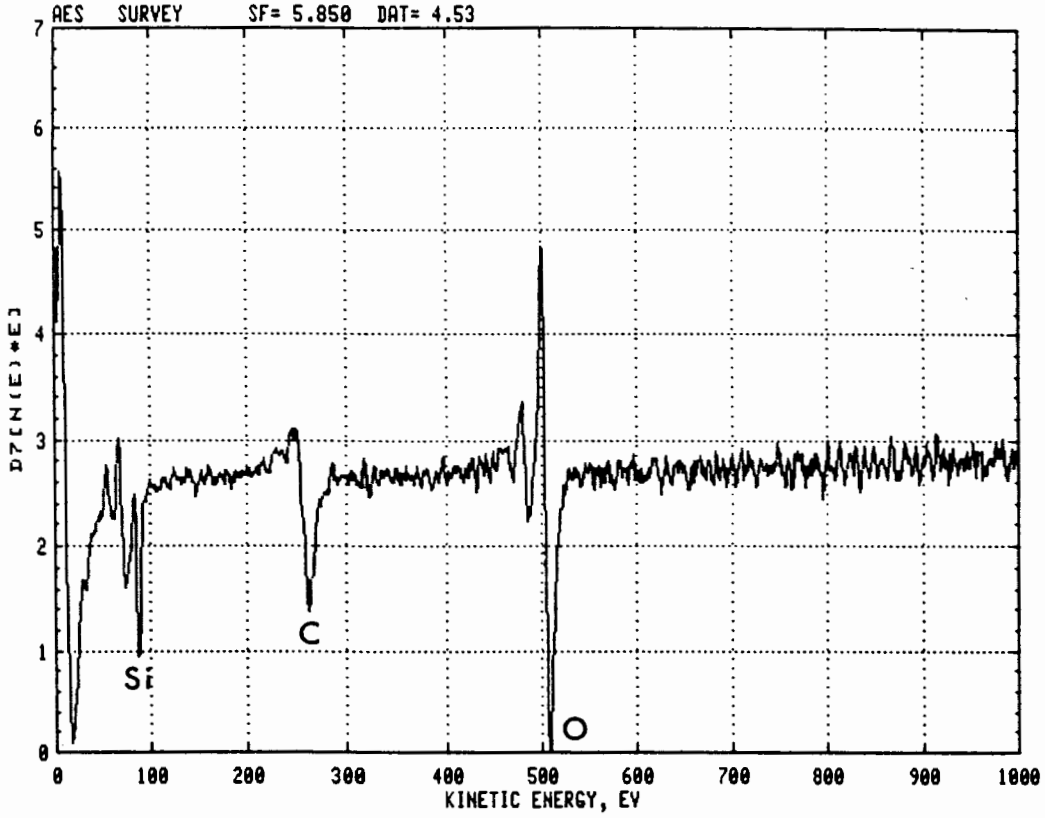

Fig.4-1a Auger survey spectrum on an unstained region.

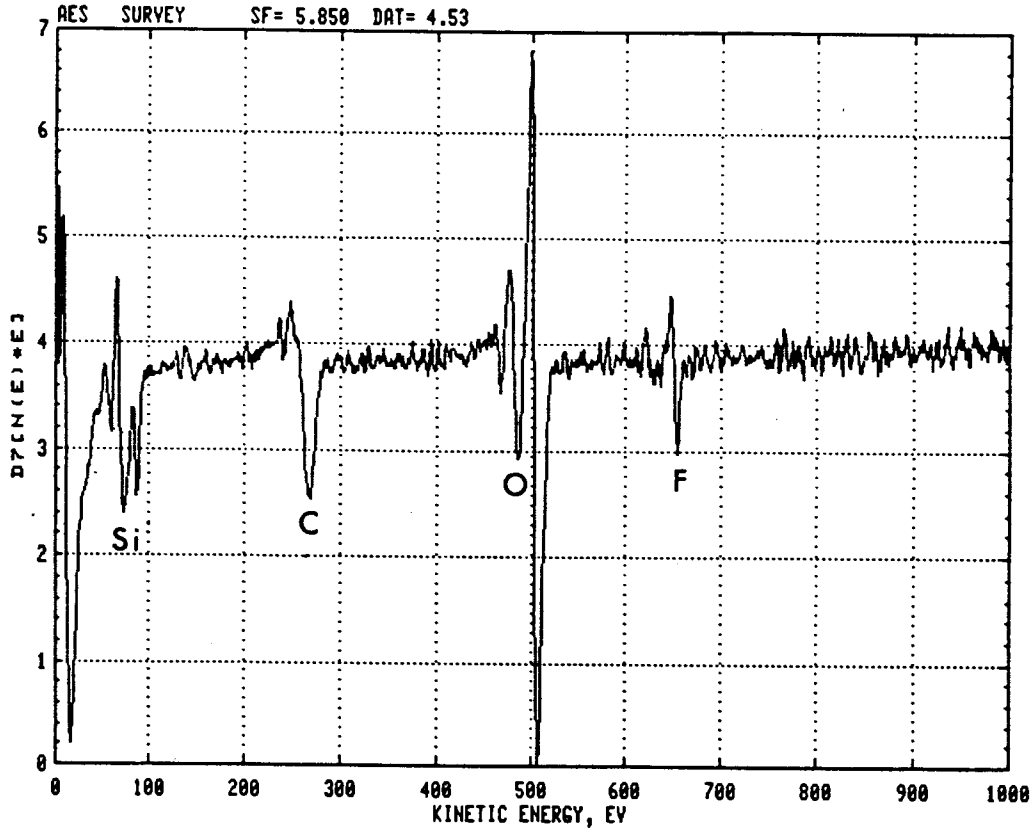

Fig.4-1b Auger survey spectrum on the surface of a stained area of p-Si sample after using the planar etch.

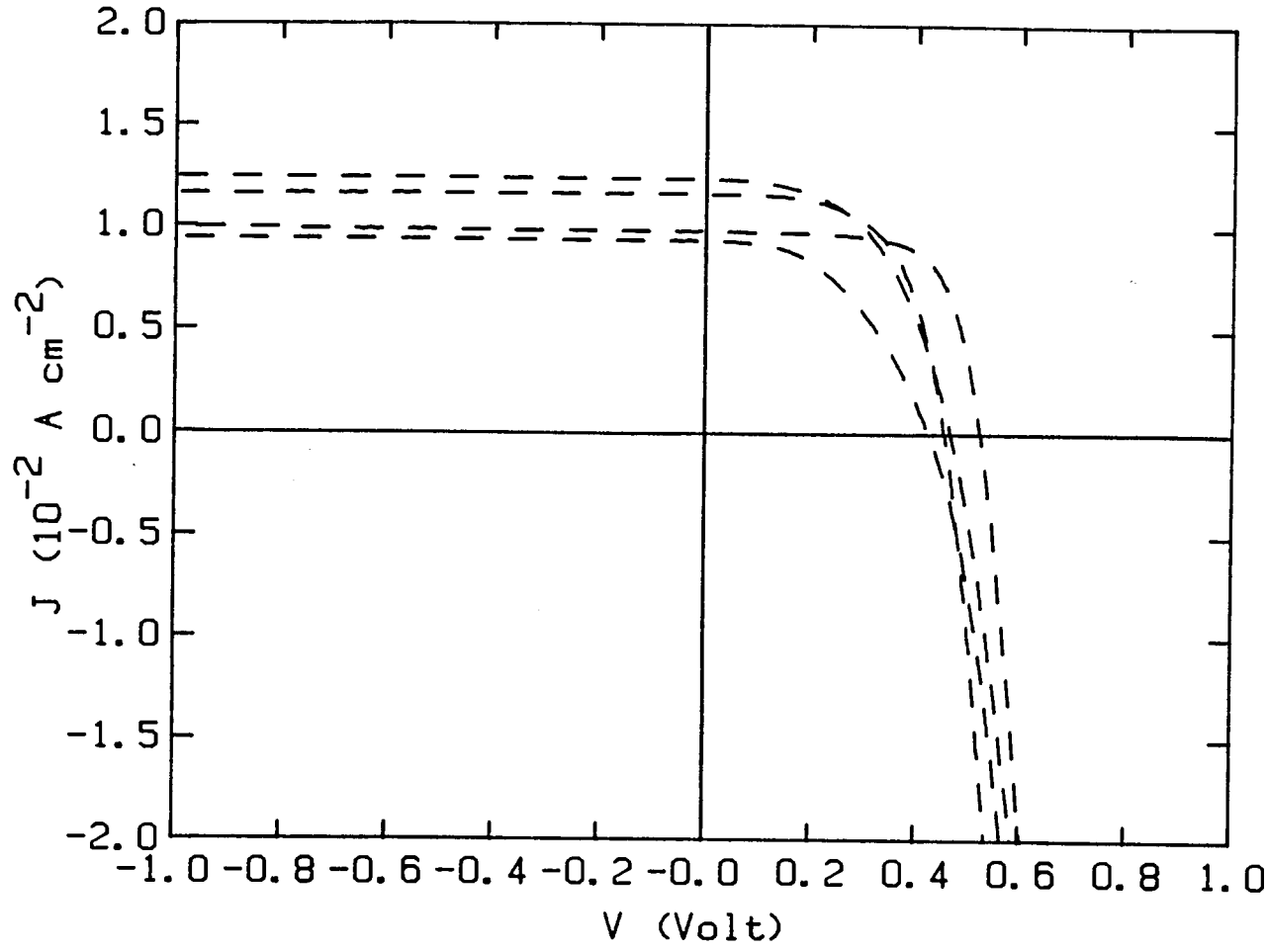

Fig.4-2a The J - V characteristics of a batch of samples where the planar etch has been used.

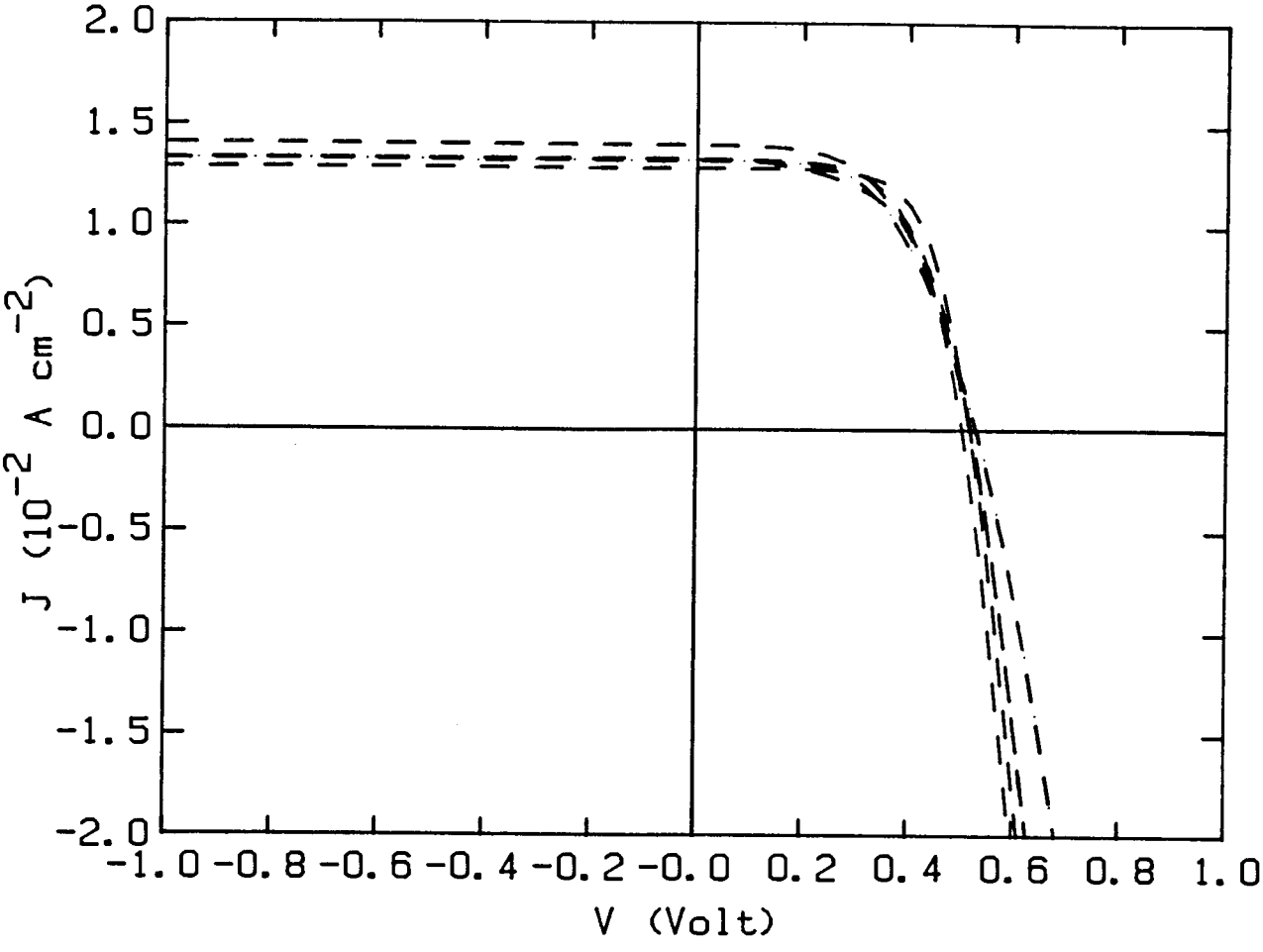

Fig.4-2b The J - V characteristics of a batch of samples prepared without using the planar etch. 10% HF was used instead. This batch shows better reproducibility.

TABLE 4-1

Oxidataion time (min)	ΔVoc/Voc	Δη/η	Oxide thickness +/- 3 Å
0	0.36	0.35	12
5	0.42	0.63	18
30	0.32	0.27	24
180	0.30	0.81	24

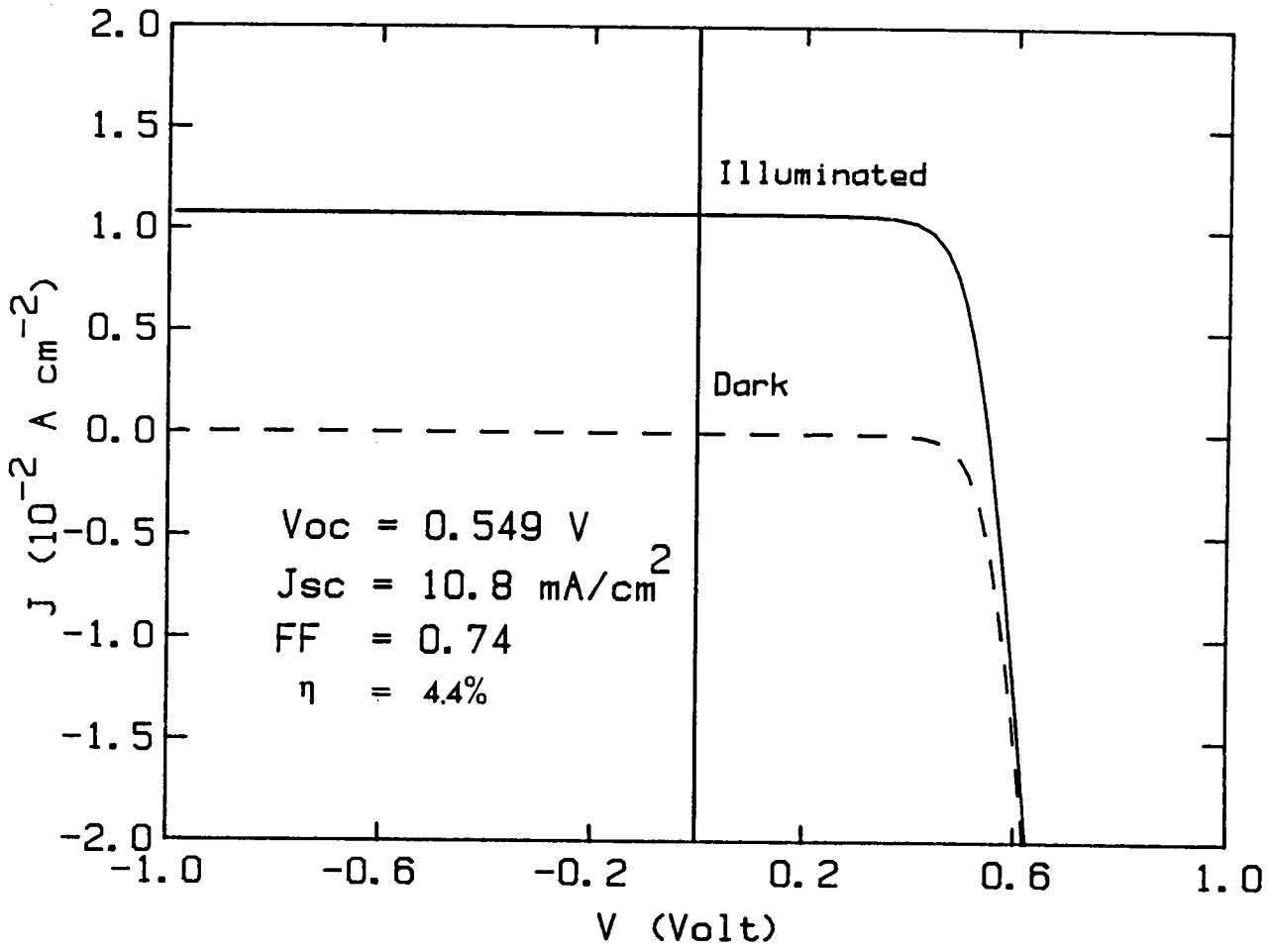

Fig.4-3 J-V characteristics of an MIS cell. Both the dark and the illuminated cases are shown. Accounting for the reflection losses, this cell corresponds to an efficiency of 7.7% (AM2).

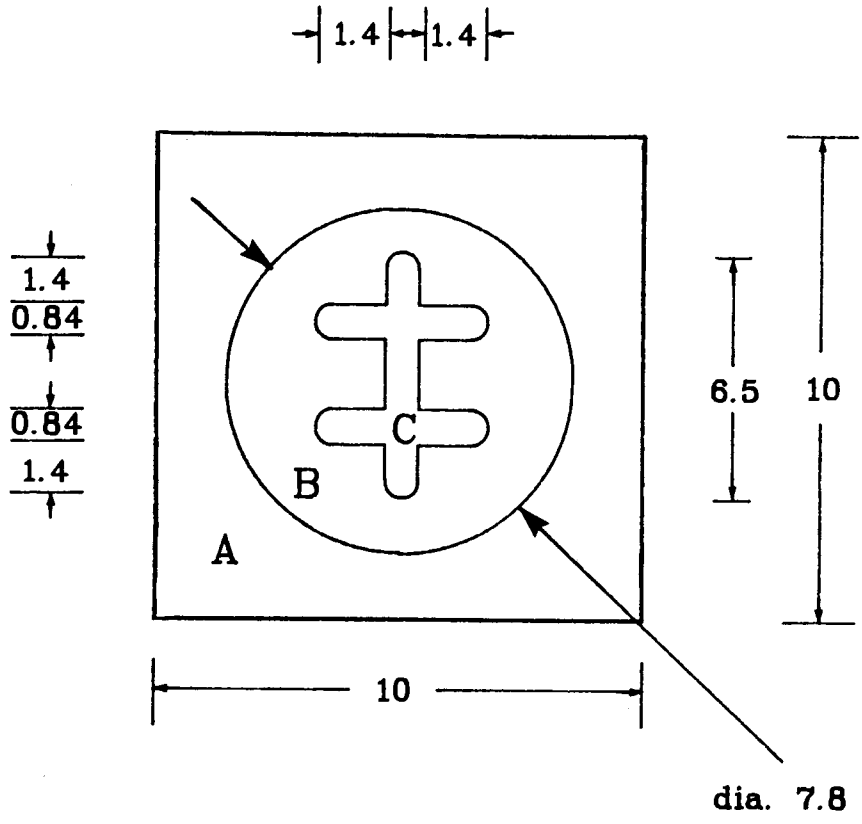

Fig.4-3b. The top view of the MIS cell.
All dimensions are in mm.
A - p-type silicon
B - thin (50 Å) circular Al layer
C - thick Al contact pad

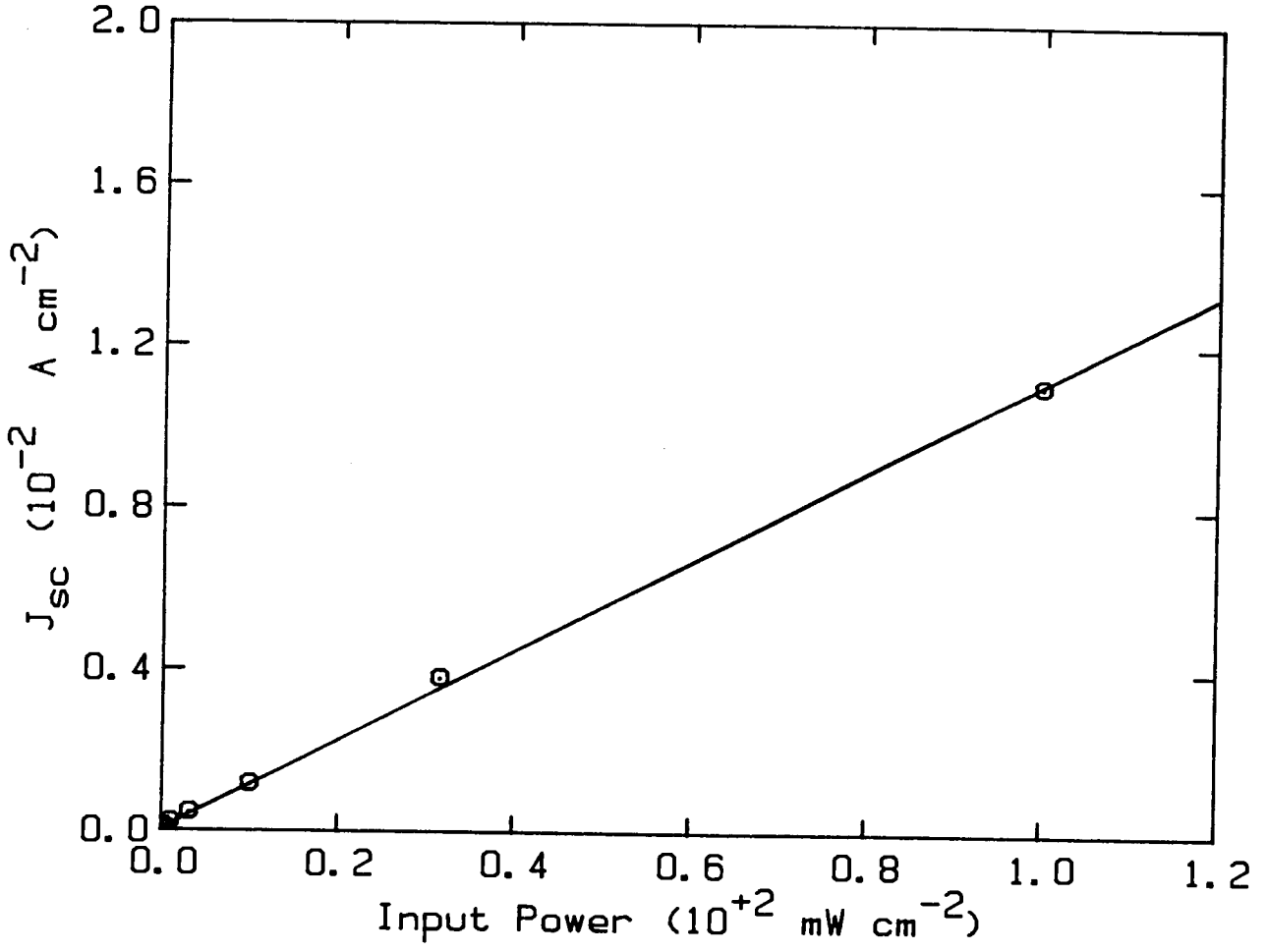

Fig.4-4a The short circuit current density versus the illumination intensity of an MIS cell (P124). This shows, as usual, that the J_{sc} is proportional to the light intensity.

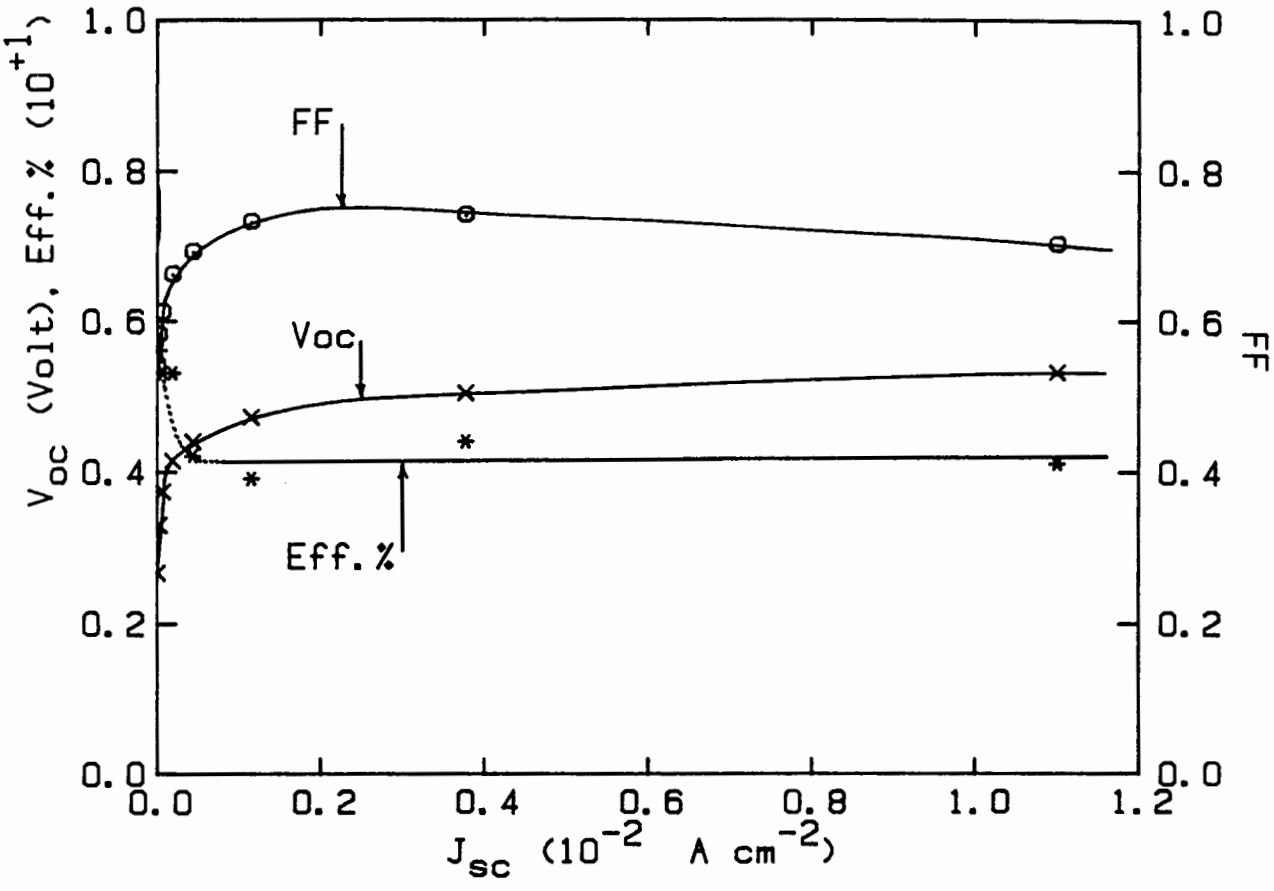

Fig.4-4b The behavior of the cell parameters with illumination. The open circuit voltage V_{oc}, the efficiency η %, and the fill factor FF are plotted against the short circuit current density J_{sc}.

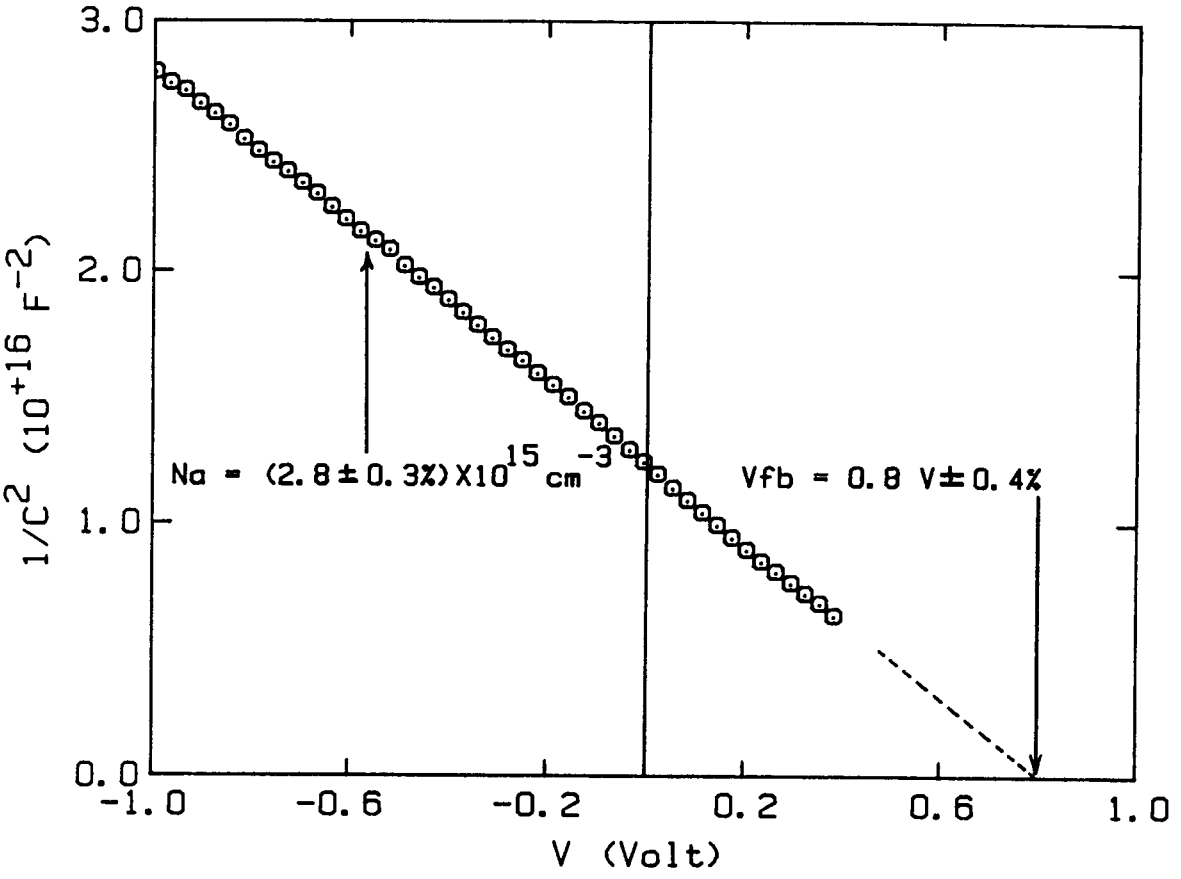

Fig.4-5 A plot of $1/C^2$ versus V (Mott-Schottky plot) of an MIS sample (P56). The doping density is calculated from the slope. The flat band potential is given by the intercept.

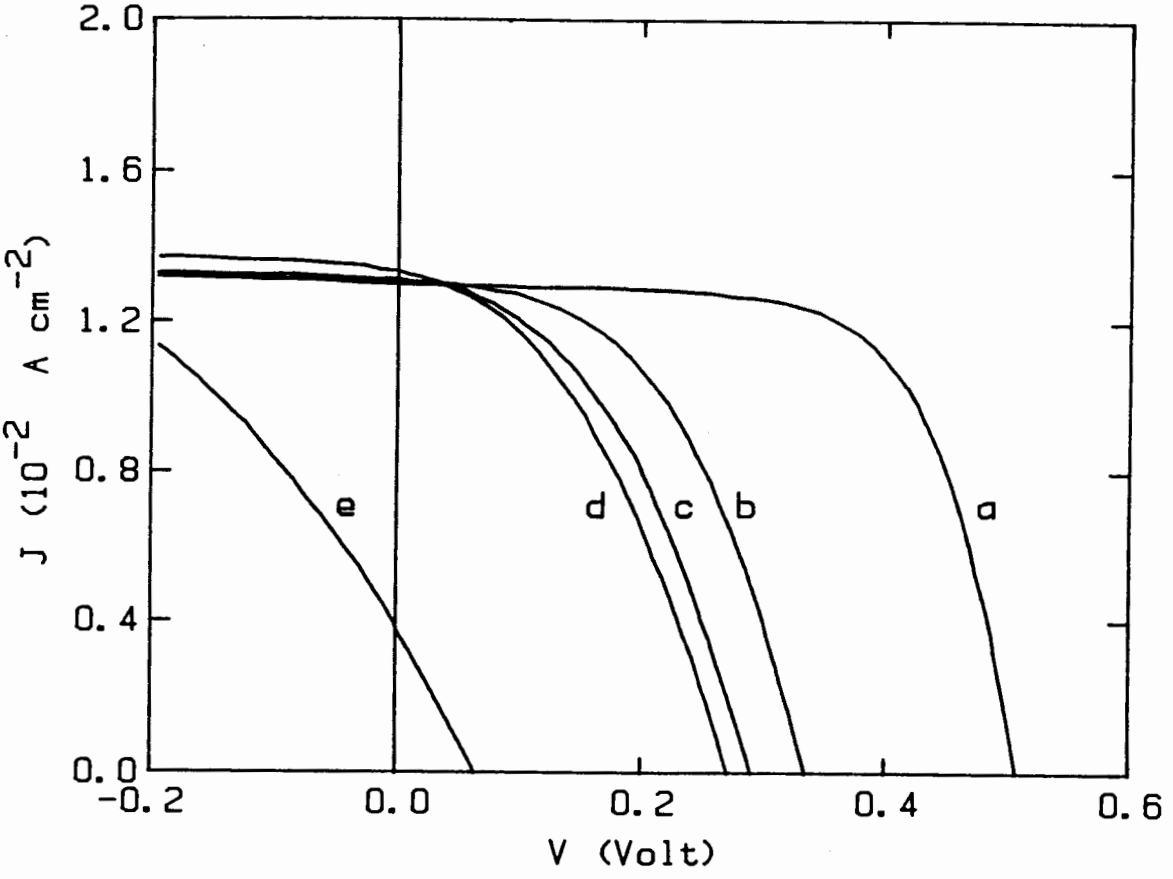

Fig.4-6a Illuminated J - V characteristics of cells damaged with various particle sizes (or lengths of dislocation loops).
(a) undamged (b) 0.05 μm (c) 0.1 μm (d) 0.3 μm (e) 1 μm.

Table 4-2 Parameters of undamaged and damaged solar cells.

ℓ (μm)	V_{oc} (mV)	J_{sc} (mA cm^{-2})	FF	η %	D_{dl} (10^8 cm^{-2})
0	527±14	11.4±1.3	0.70±0.05	4.1±0.5	0
0.05	316±78	11.7±1.6	0.52±0.10	1.2±0.2	4.4±2.0
0.1	295±19	11.1±1.3	0.54±0.02	1.7±0.3	10.0±8.0
0.3	242±66	9.2±2.0	0.41±0.60	0.9±0.3	4.5±2.7
1	79±19	4.3±1.0	0.26±0.03	0.14±0.14	23.0±2.1

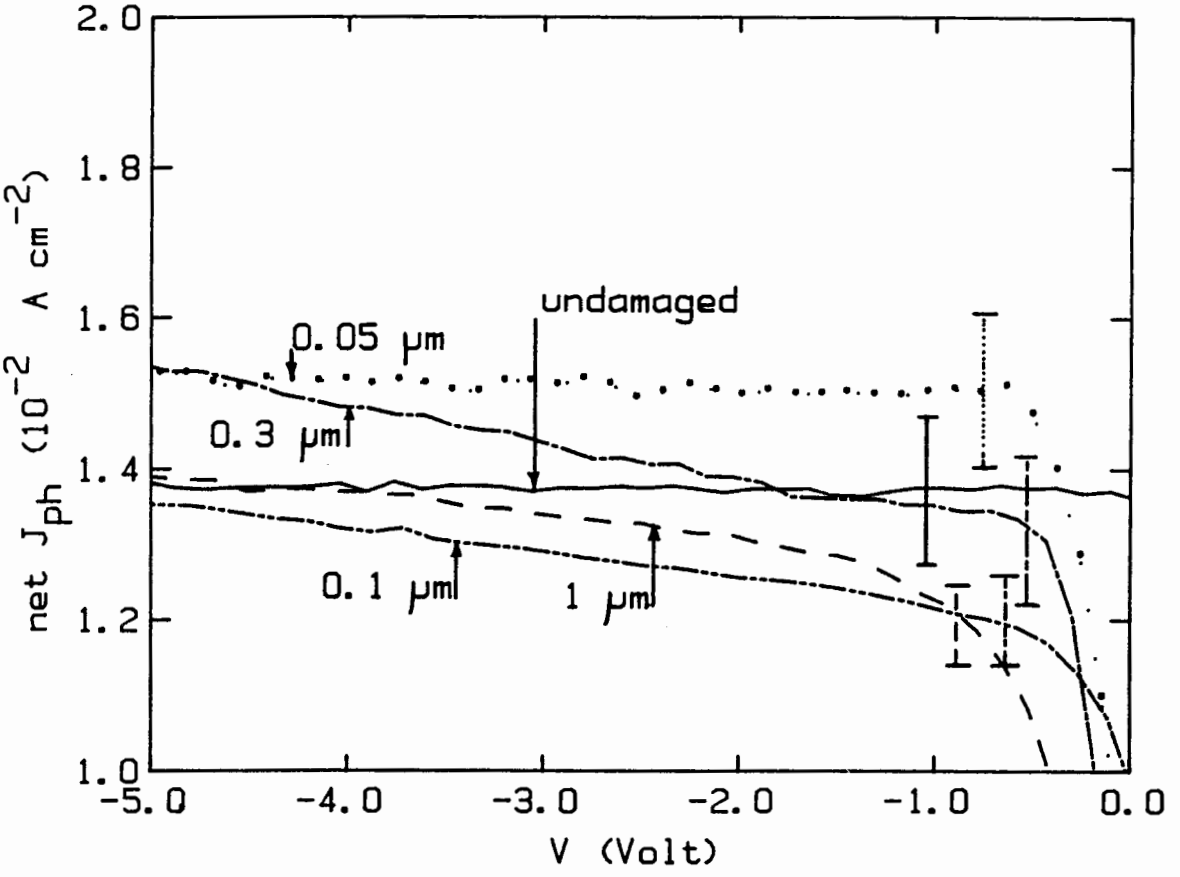

Fig.4-6b The net photocurrent density (saturation photocurrent), J_{ph} of MIS cells of various damage sizes versus reverse bias plotted on a blown up scale. J_{ph} is obtained by subtracting the reverse dark current from the current under illumination. Note that the origin of the J_{ph} axis is not zero but 10 mA cm^{-2}.

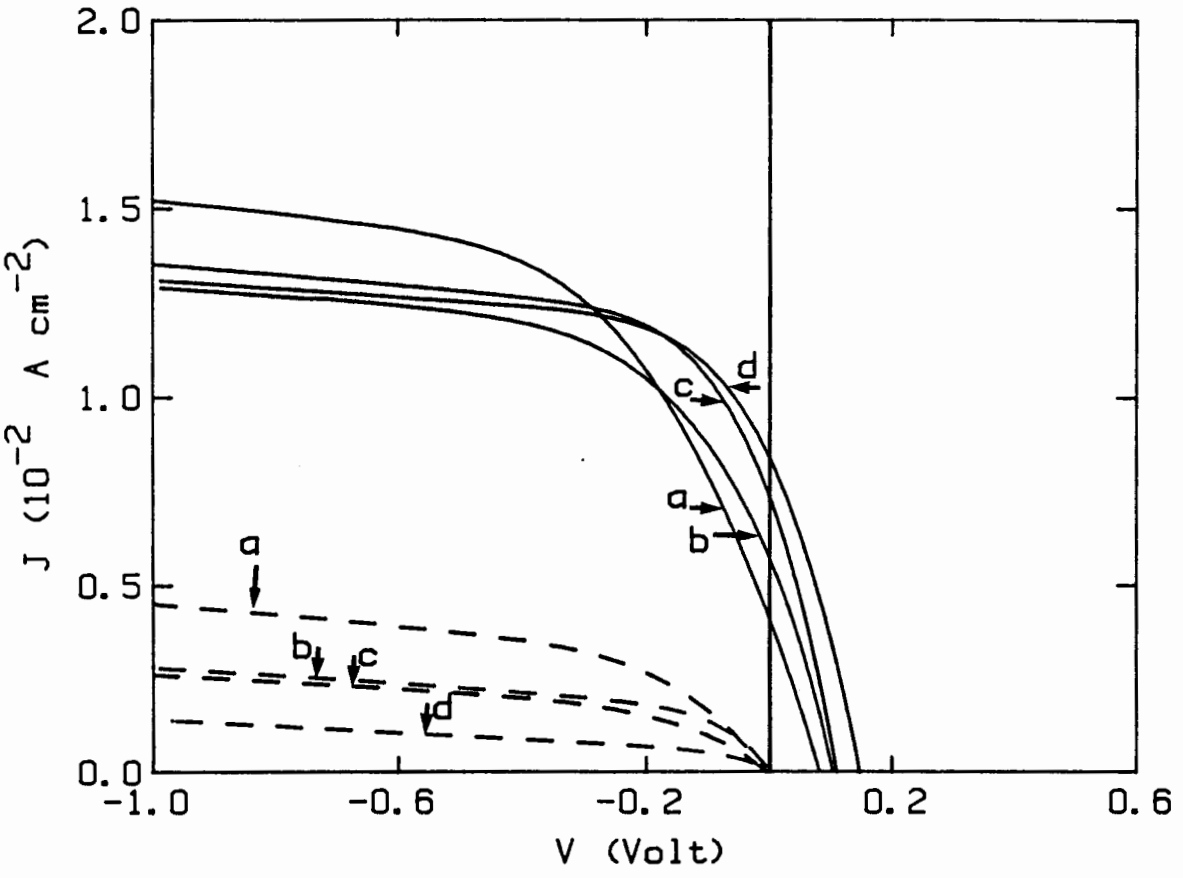

Fig.4-7 The dark (dotted lines) and illuminated (solid lines) J - V curves of 1 μm damaged MIS cell (P115D) prepared after successively etching the surface for 20 s in 10% HF.

(a) The original 1 μm damaged sample (b) After the first 20 s etch (c) After the second etch (d) After the third etch.

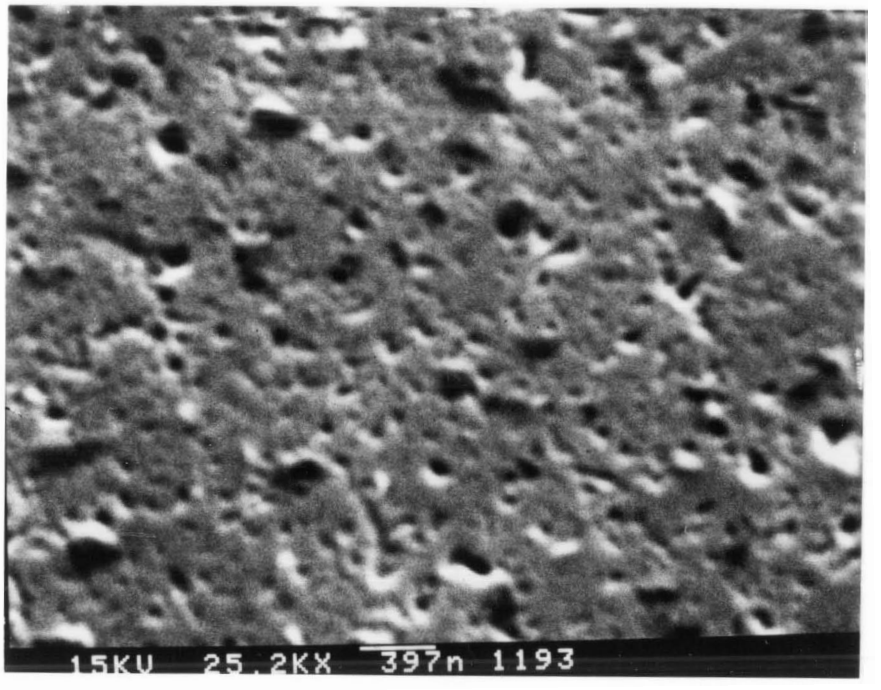

Fig.4-8a Scanning electron micrograph of a sample damaged with 0.3 μm that has been treated with the Dash etch for 20 s. This shows the various sizes of etch pits and all were counted.

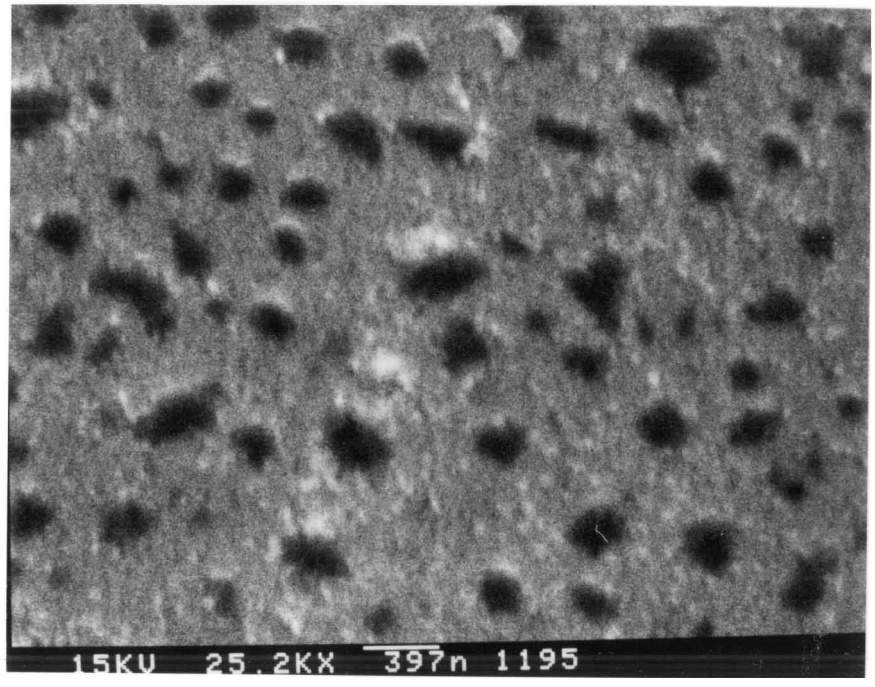

Fig.4-8b Scanning electron micrograph of a sample etched for 1 minute showing only the large pits. All small pits have been removed. This was not used for determining D_{dl} but the density of pits is reduced by about a factor of 5. Hence the etching time is important.

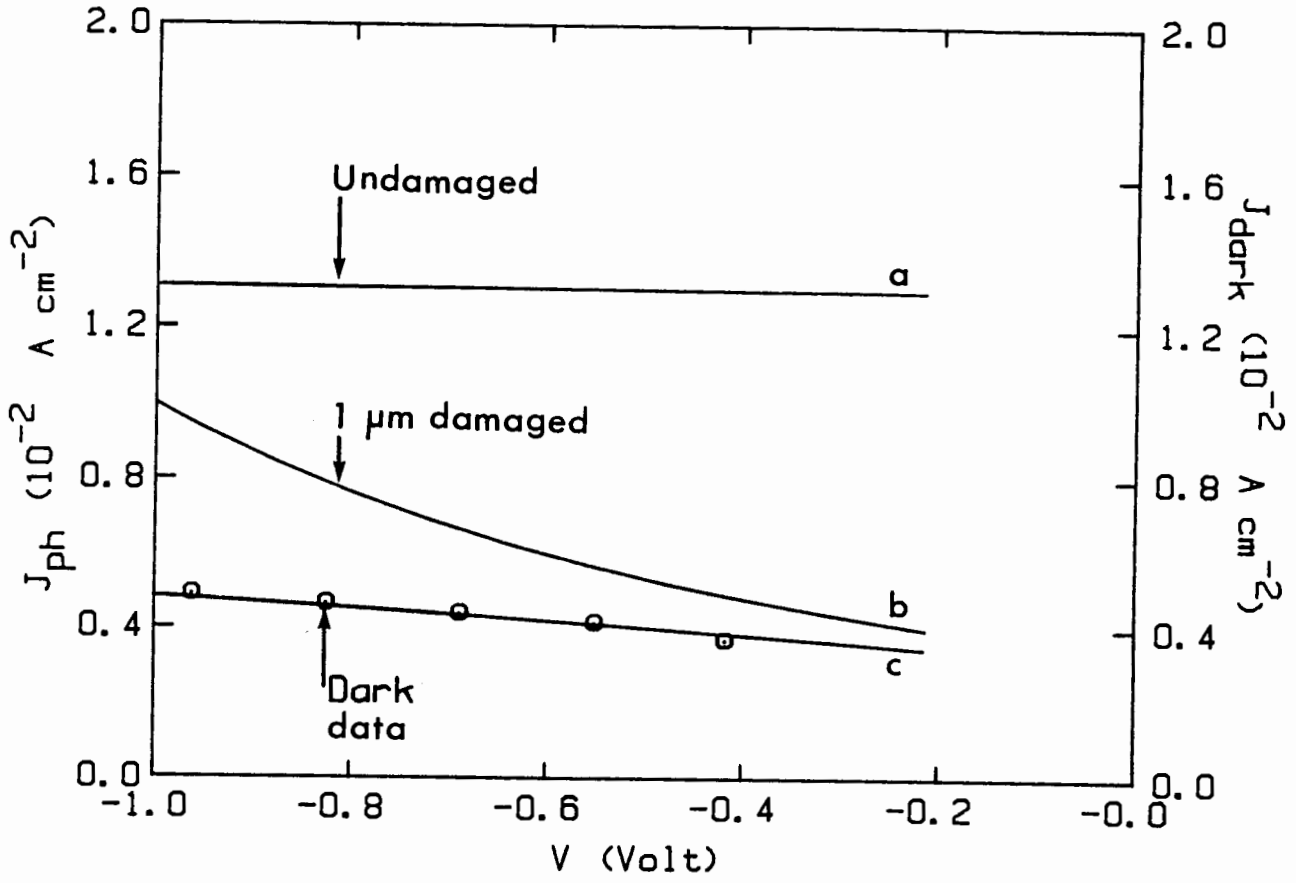

Fig.4-9 Calculated J-V curves using recombination theory at reverse bias (see Appendix I).

(a) Photocurrent of an undamaged cell
(b) Photocurrent of a 1 μm damaged cell
(c) Dark current of a 1 μm damaged cell according to the SNS theory[82].

The reverse dark current is fitted to obtain an effective life time (τ_d) for the damaged region.

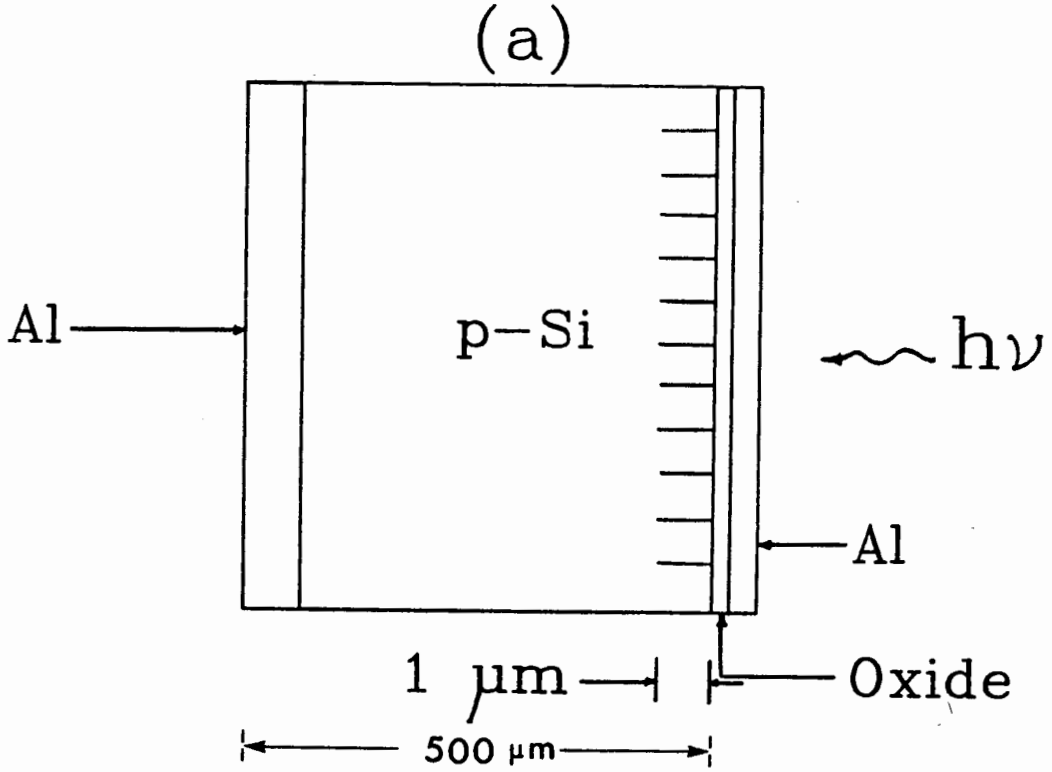

Fig.4-10a The MIS structure with mechanical damage. Dislocation loops are replaced by lines perpendicular to Si surface (not to scale).

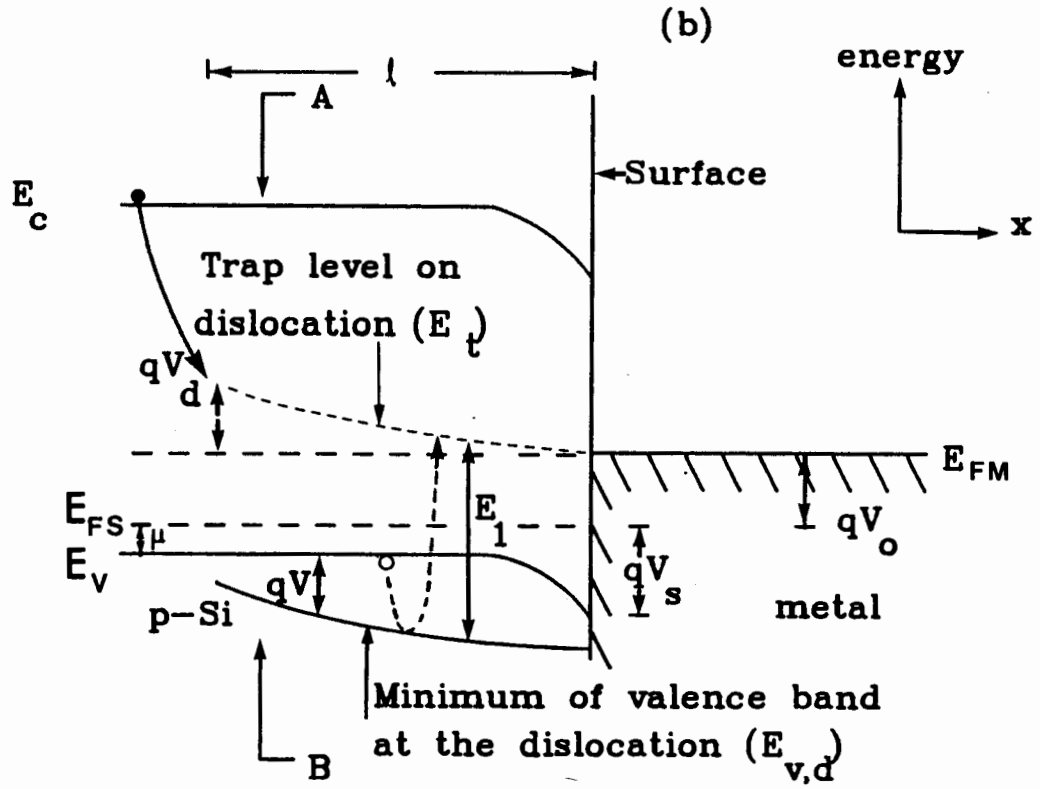

Fig.4-10b The band diagram of the cell with dislocation in the plane of paper. The insulator layer is not shown. The dislocations are indicated as extending a distance ℓ from the surface where ℓ is much greater than the space charge region width. A double layer (not shown) makes the traps in the dislocation isoenergetic with E_{FM}.

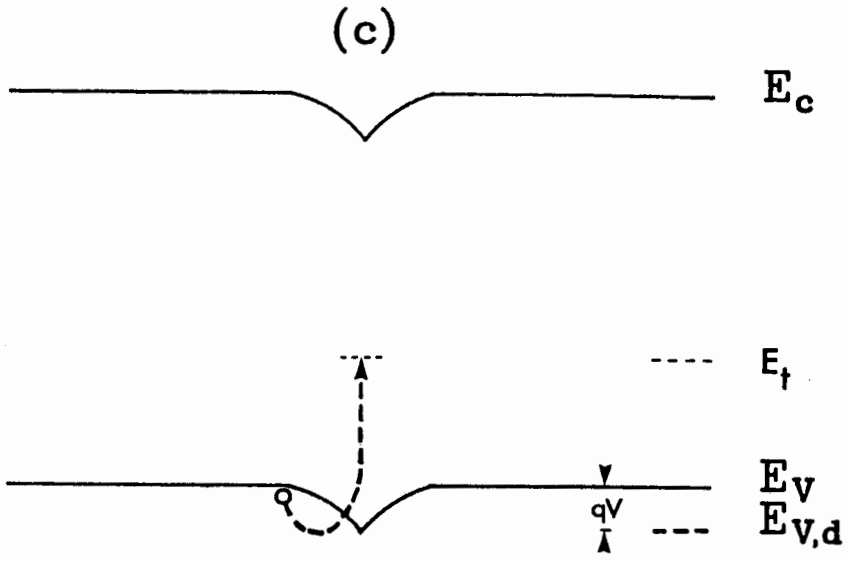

Fig.4-10c Cross-sectional diagram at AB of Fig.4-10b viewed perpendicular to the surface of the cell.

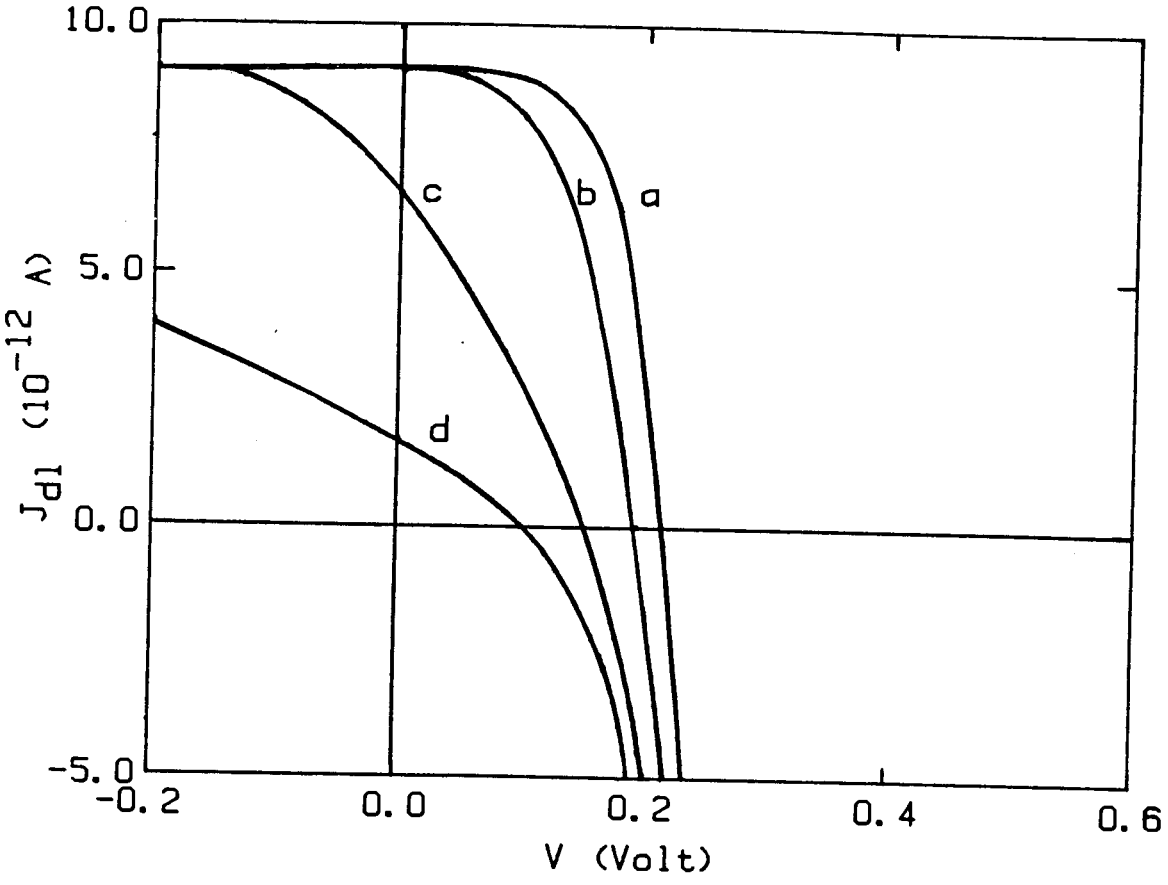

Fig.4-11a Calculated variation of the current along a dislocation (J_{d1}) with its length(ℓ) when the specific conductance, $s = 10^{-15}$ cm ohm^{-1} and $E_1 - \mu = 0.3$ eV.

(a) 0.05 μm
(b) 0.1 μm
(c) 0.3 μm
(d) 1 μm

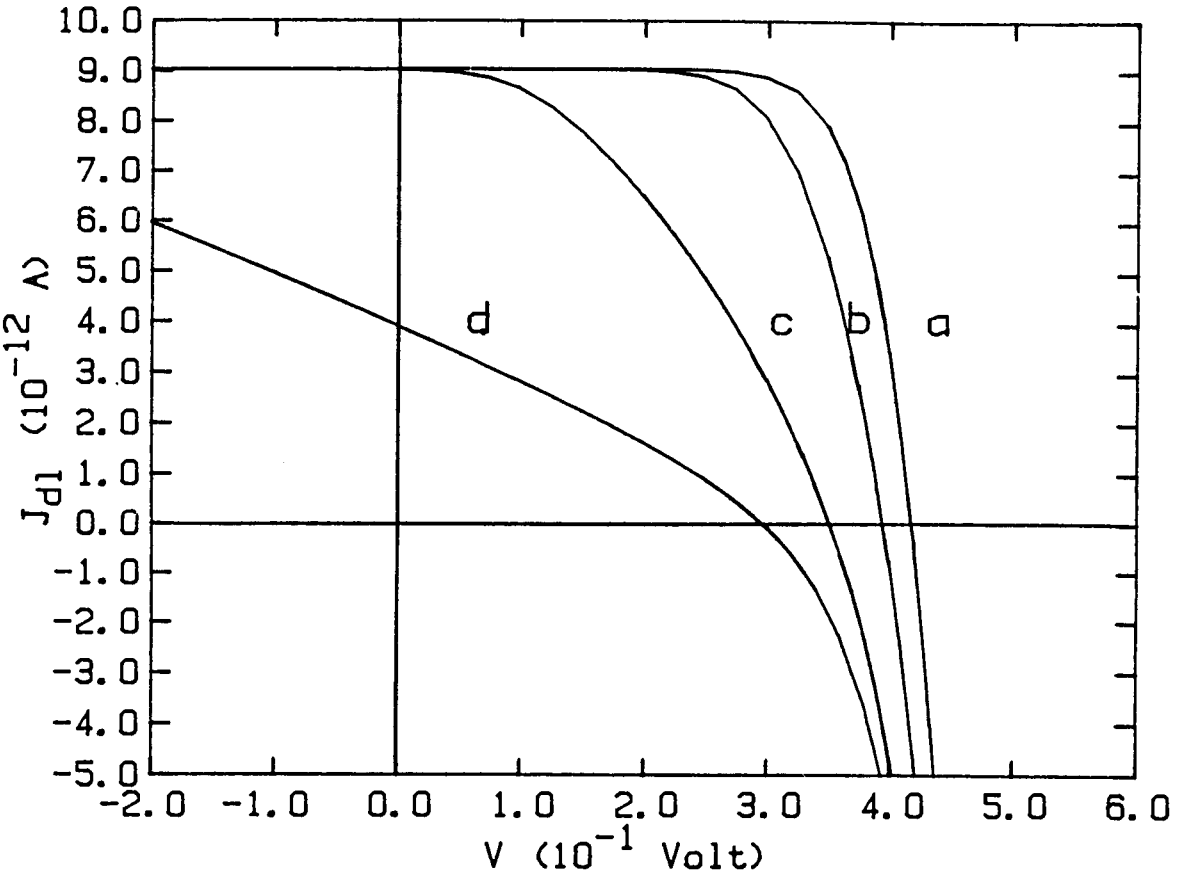

Fig.4-11b Calculated variation of the current along a dislocation (J_{dl}) with length (ℓ) when the specific conductance, $s = 10^{-15}$ cm ohm^{-1} and $E_1 - \mu = 0.5$ eV.

(a) 0.05 μm
(b) 0.1 μm
(c) 0.3 μm
(d) 1 μm

Table 4-3 Parameters used in calculations.

Symbol	Numerical value
P_b	3×10^{15} cm^{-3}
β	40 V^{-1}
$\bar{c}$	10^7 cm s^{-1}
p	10^{-15} cm^2
p_u	3×10^7 cm^{-1}
ℓ	0.05 to 1 μm
D_{dl}	10^9 cm^{-2}
$E_l - \mu$	0.3 eV
α	0.3
J_{ph}	11.4 mA cm^{-2}

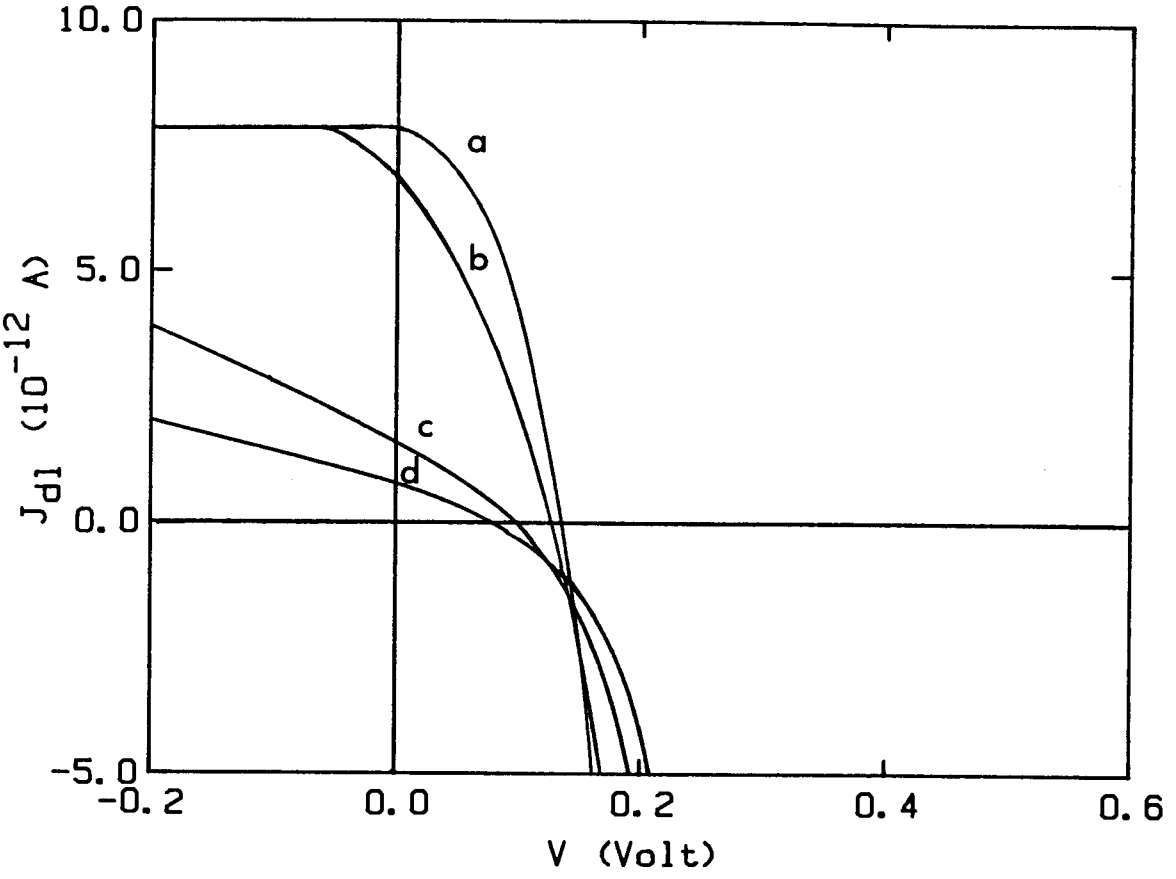

Fig.4-12a Effect of specific conductance, s on J-V characteristics of a dislocation (length = ℓ = 1 μm) for the case of $E_1 - \mu$ = 0.3 eV.

(a) 10^{-14} cm ohm^{-1}

(b) 5 x 10^{-15} cm ohm^{-1}

(c) 10^{-15} cm ohm^{-1}

(d) 5 x 10^{-16} cm ohm^{-1}

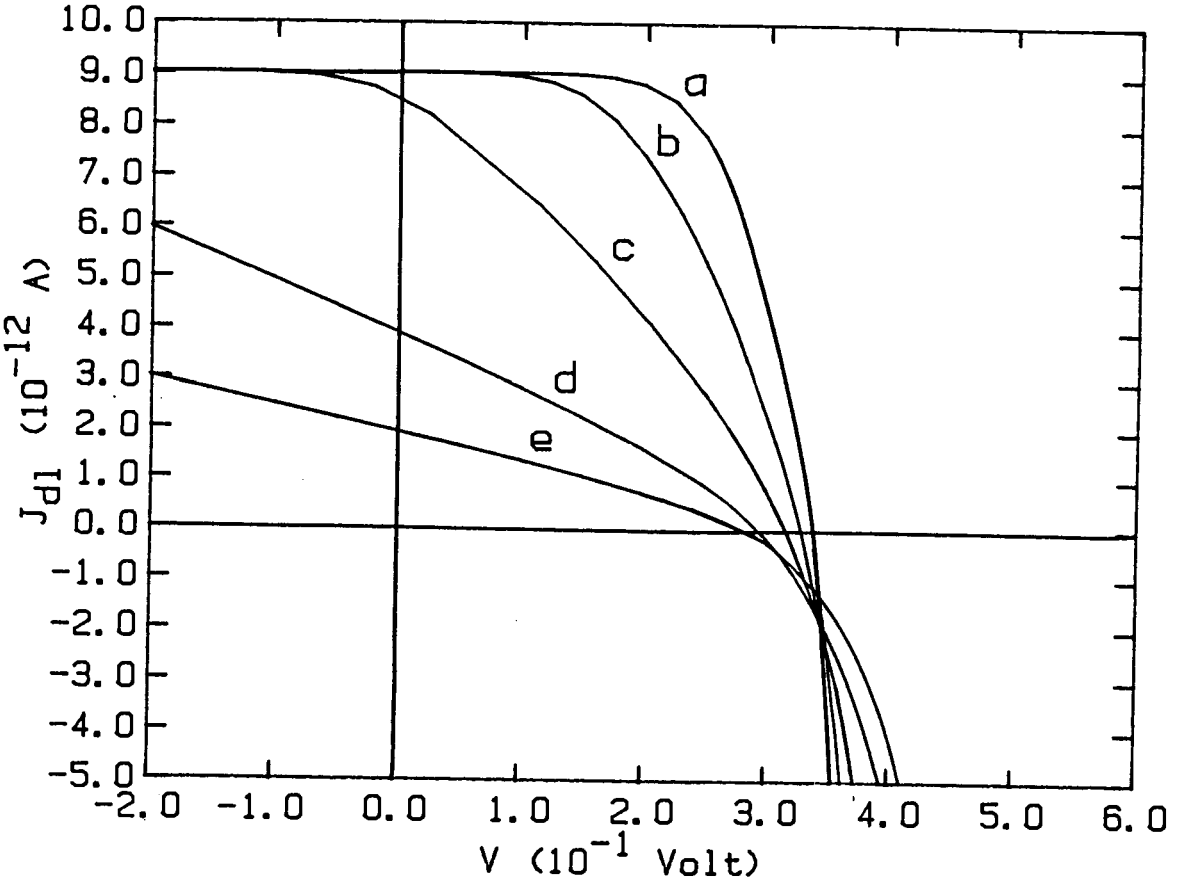

Fig.4-12b Effect of specific conductance, s on J-V characteristics of a dislocation (length = ℓ = 1 μm) for the case of $E_1 - \mu$ = 0.5 eV.

(a) 10^{-14} cm ohm^{-1}

(b) 5 x 10^{-15} cm ohm^{-1}

(c) 2.5 x 10^{-15} cm ohm^{-1}

(d) 10^{-15} cm ohm^{-1}

(e) 5 x 10^{-16} cm ohm^{-1}

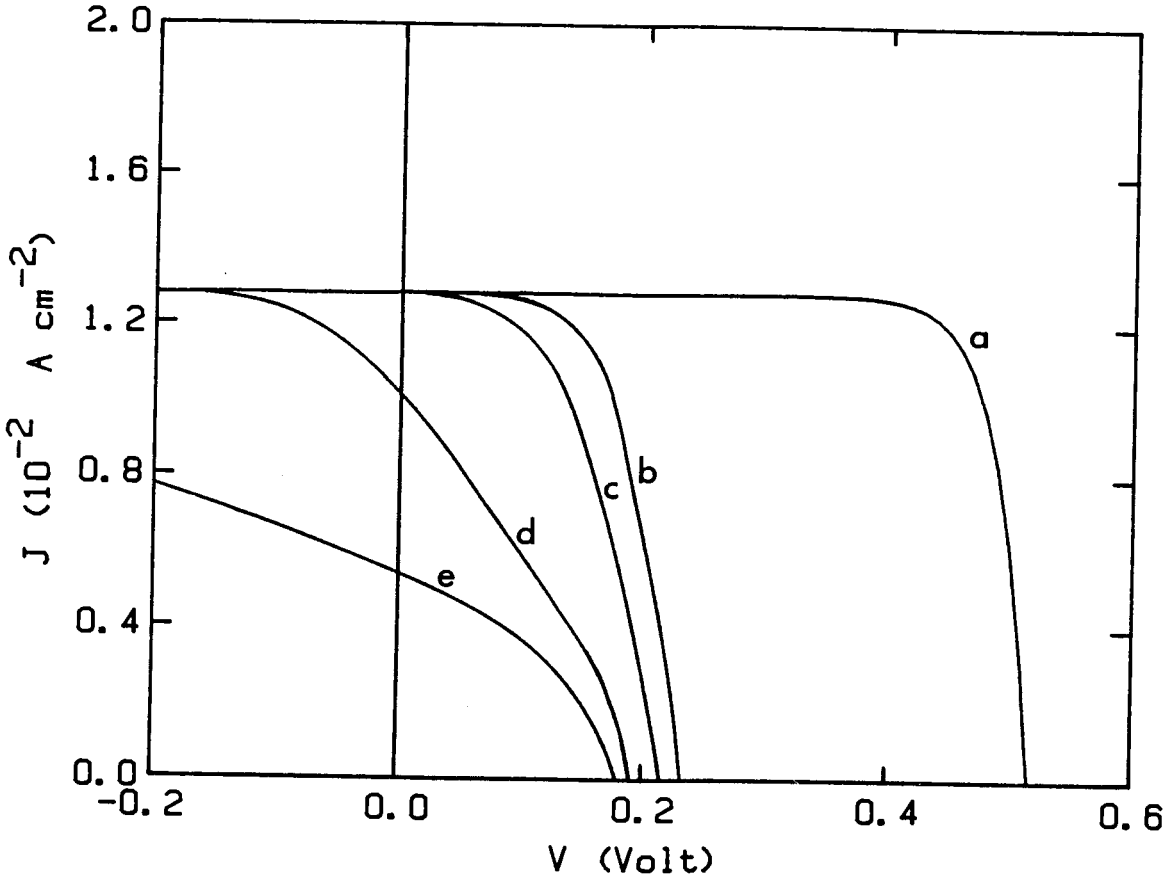

Fig.4-13a Variation of the total J-V characteristics of MIS cell with dislocations of length ℓ when $E_1 - \mu = 0.3$ eV.

(a) 0 μm
(b) 0.05 μm
(c) 0.1 μm
(d) 0.3 μm
(e) 1 μm

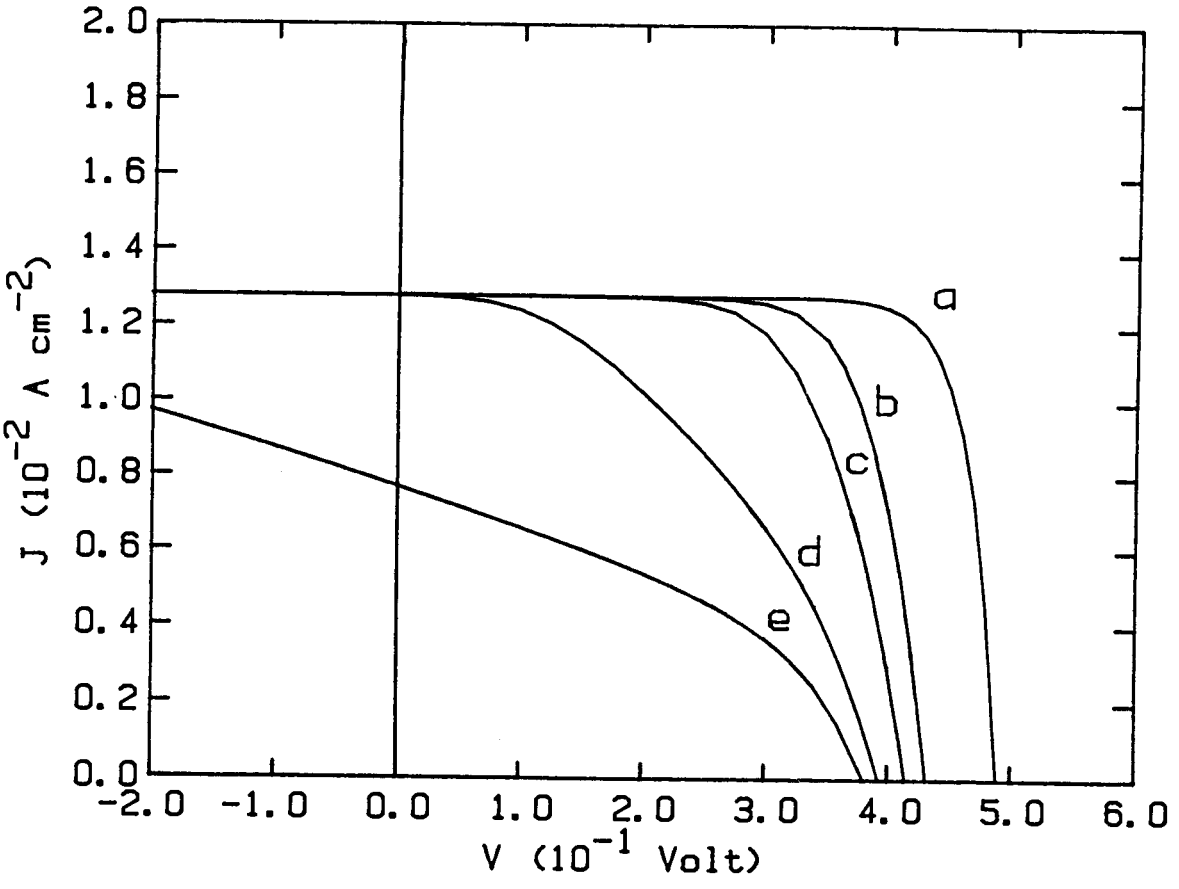

Fig.4-13b Variation of the total J-V characteristics of MIS cell with dislocations of length ℓ when $E_1 - \mu = 0.5$ eV.

(a) 0 μm
(b) 0.05 μm
(c) 0.1 μm
(d) 0.3 μm
(e) 1 μm

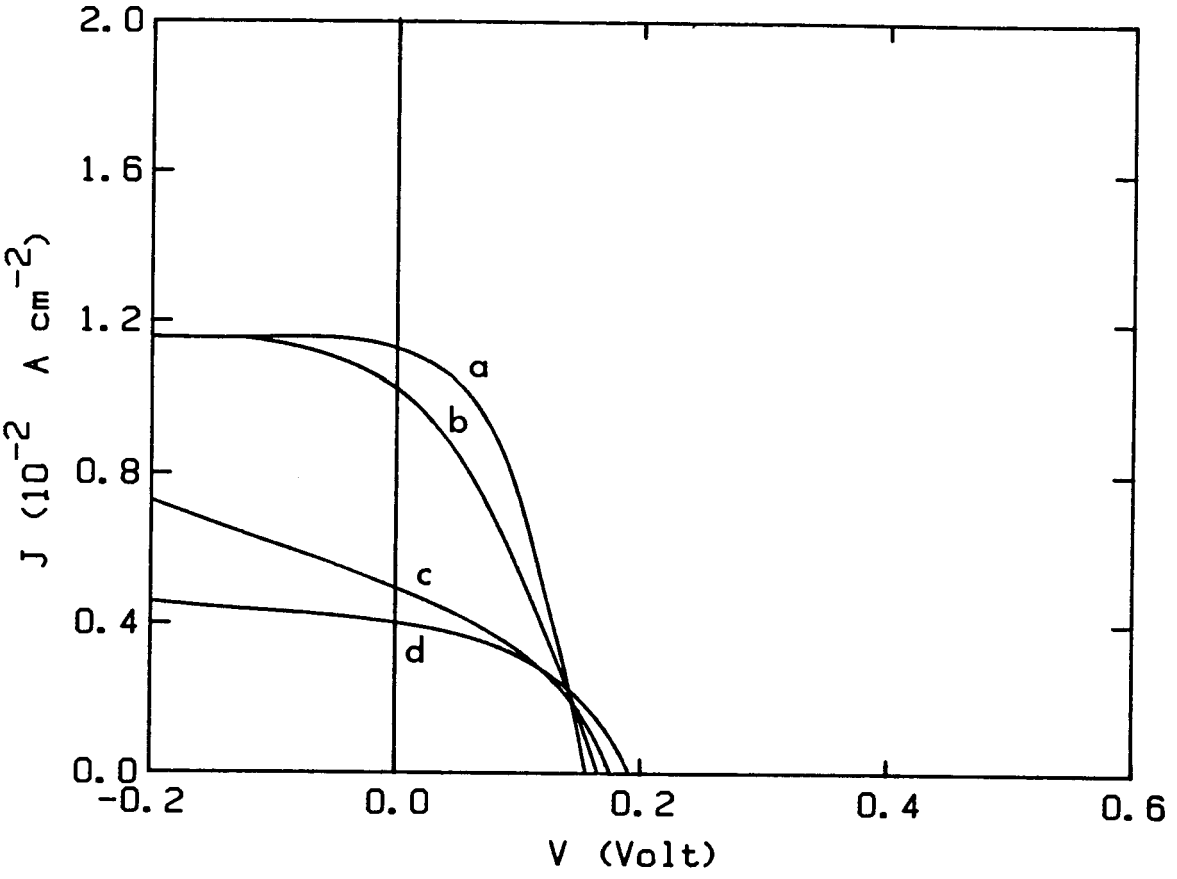

Fig.4-14a Variation of the total J-V characteristics of MIS cell with specific conductance, s of dislocations with a fixed length of 1 μm when $E_1 - \mu = 0.3$ eV.

(a) 10^{-14} cm ohm^{-1}

(b) 5×10^{-15} cm ohm^{-1}

(c) 10^{-15} cm ohm^{-1}

(d) 5×10^{-16} cm ohm^{-1}

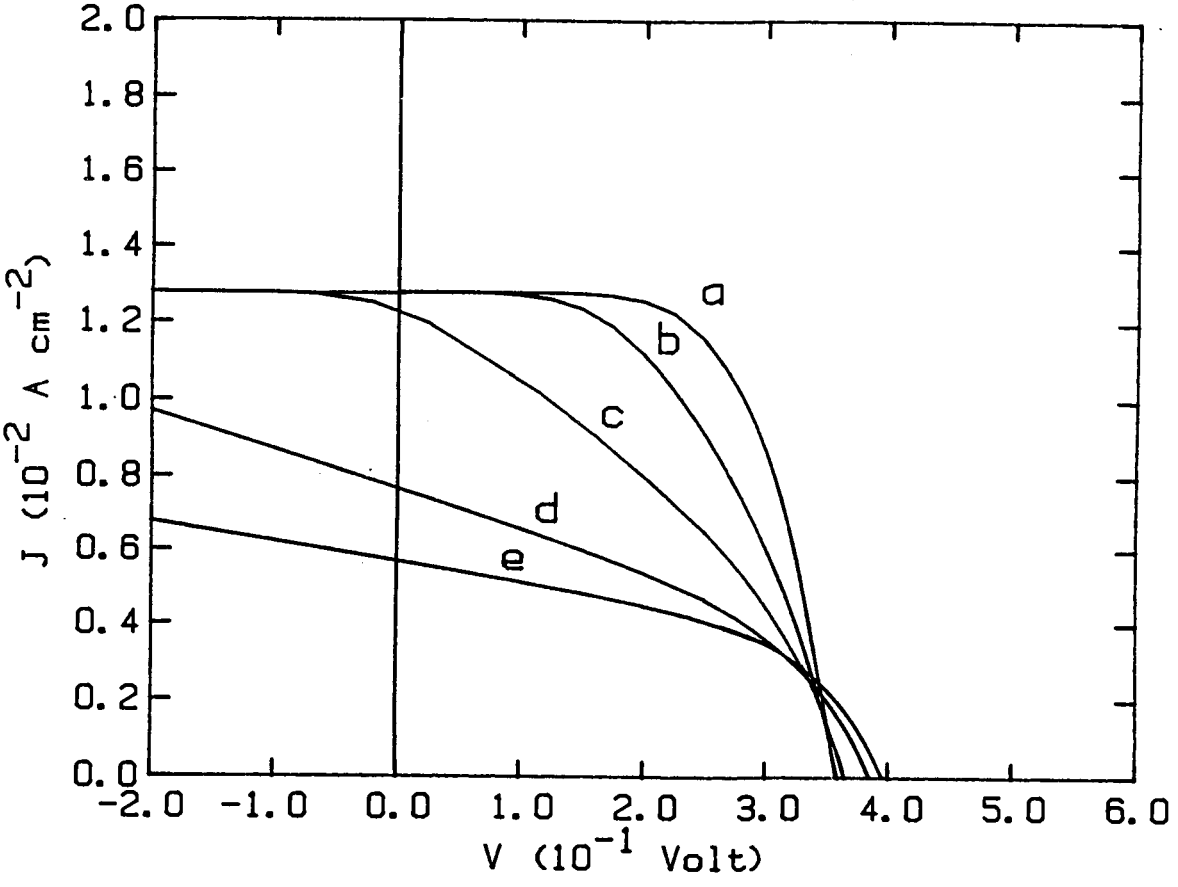

Fig.4-14b Variation of the total J-V characteristics of MIS cell with specific conductance, s of dislocations with a fixed length of 1 μm when $E_1 - \mu = 0.5$ eV.

(a) 10^{-14} cm ohm^{-1}

(b) 5×10^{-15} cm ohm^{-1}

(c) 2.5×10^{-15} cm ohm^{-1}

(d) 10^{-15} cm ohm^{-1}

(e) 5×10^{-16} cm ohm^{-1}

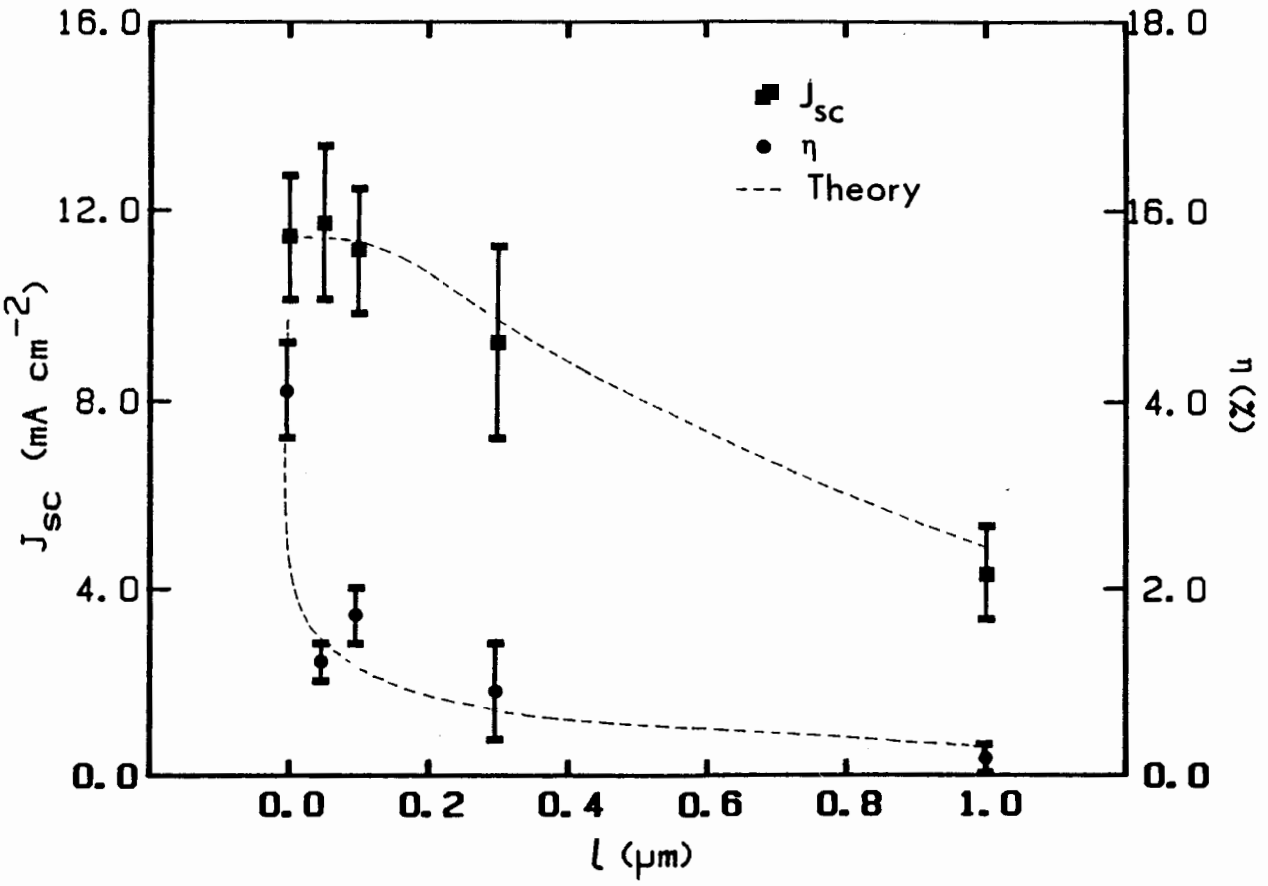

Fig.4-15a The variation of the short circuit current, J_{sc} and the efficiency, η with the length, ℓ of dislocations. Calculated variation is shown in dashed lines.

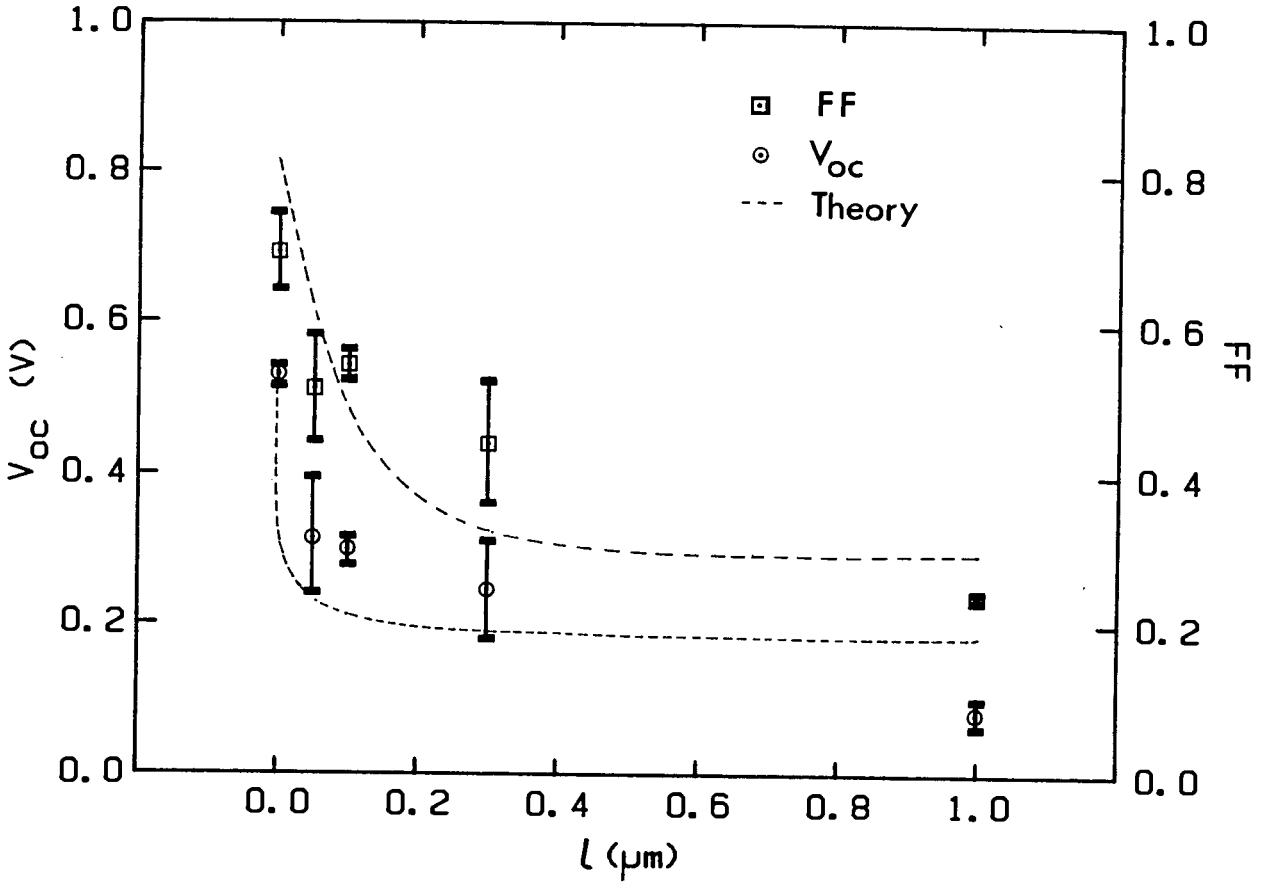

Fig.4-15b The variation of the open circuit voltage, V_{oc} and the fill factor, FF with the length, ℓ of dislocations. Calculated variation is shown in dashed lines.

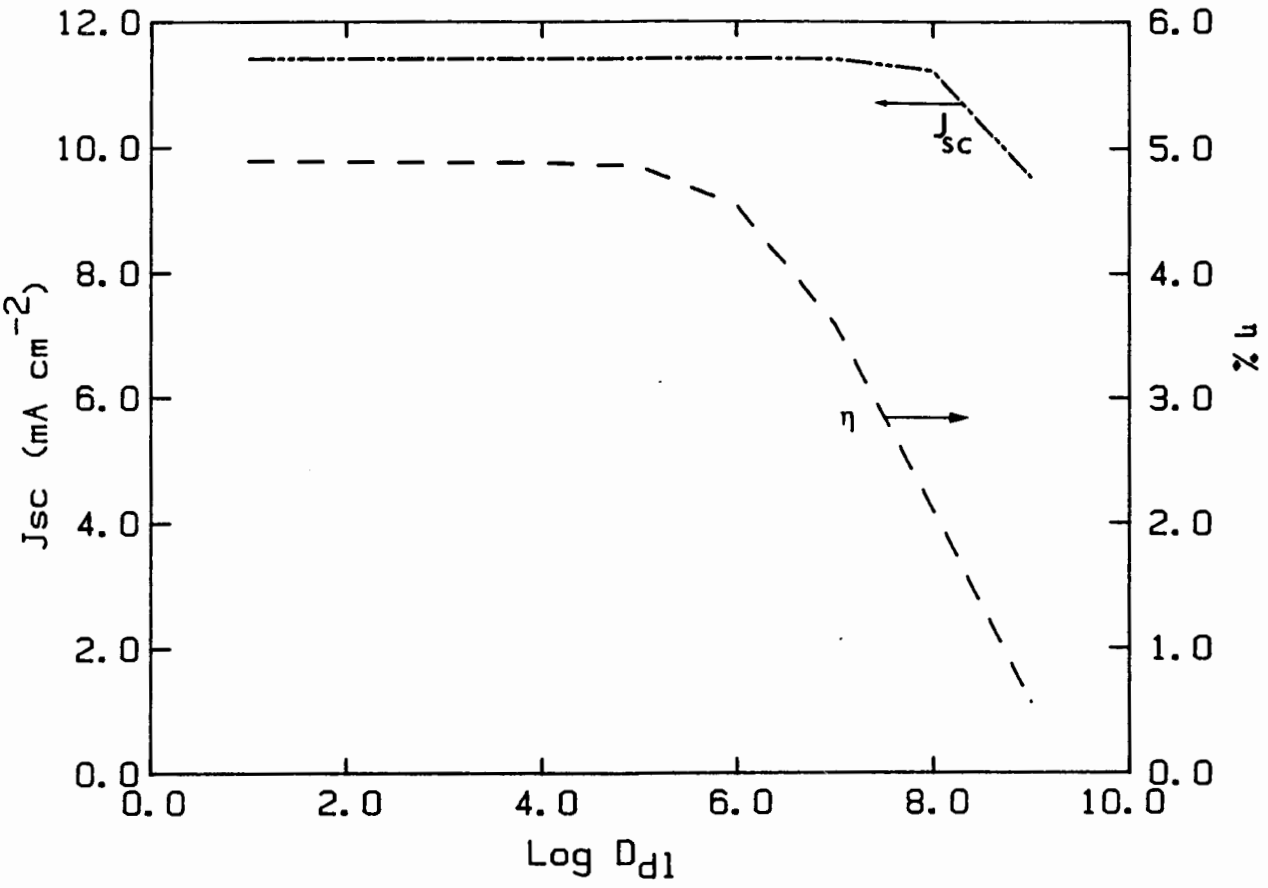

Fig.4-16a Calculated variation of J_{sc} and η with the density of dislocations, D_{dl}.

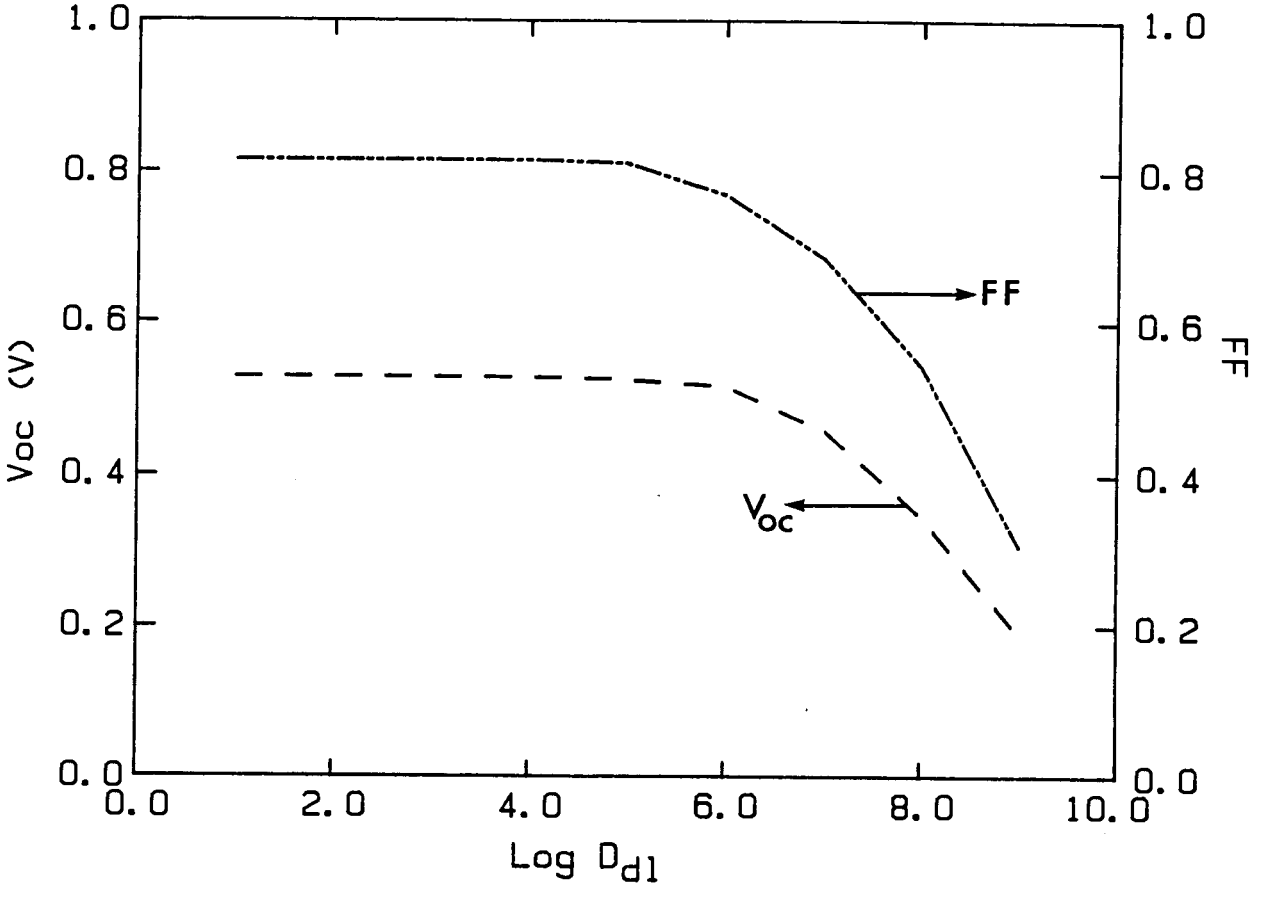

Fig.4-16b Calculated variation of V_{oc} and FF with the density of dislocations, D_{dl}.

CHAPTER V

FURTHER STUDIES OF DISLOCATIONS

5.1 Photoelectrochemical data

To further verify the results obtained in MIS measurements, one half of several batches of damaged samples prepared similar to those measured earlier were sent to Dr. W.P. Gomes in University of Gent in Belgium for photoelectrochemical (PEC) measurements. The other half of the samples were retained, and were measured in the MIS configuration. To avoid a discrepancy of results due to any time dependence of the properties of the dislocations introduced by lapping, both type of measurements were carried out at the same period of time after their initial preparation (lapping).

The PEC procedure is much simpler, experimentally. An ohmic contact is made at the back side of the silicon sample (damaged or undamaged) with Ga-In eutectic, and the surface is masked with an epoxy so that when the sample is immersed in the electrolyte only the front surface is exposed to the solution. The electrolyte used was NH_4F with or without a $K_4Fe(CN)_6/K_3Fe(CN)_6$ redox couple in water as discussed below. The current-voltage characteristics were measured using a He-Ne laser as the source of light. Their measuring system allowed them to obtain a scanning laser spot (SLS) map of the sample, which is essentially a 2 dimensional distribution of the net photocurrent with position of the sample surface.

A small variation of the sample preparation was introduced for another experiment where, after initial sample lapping (with 0.3 μm powder) half of the surface was masked with black wax which is resistant to acid etch. The masked sample was etched in planar etch for 1 min which removed about 5 μm of the top damaged layer of the exposed region of the sample while keeping the other half intact. After the etch the wax was dissolved away and the sample was degreased, cleaned and was sent to University of Gent for laser scanning measurements.

Fig.5-1 represents a resulting laser scanning map showing a case where (a) a slight cathodic potential was applied to the sample compared to a case where (b) a high cathodic (reverse) potential was appled. These measurements were made on a single sample, the left half of which was polished with alumina grit of 0.3 μm. The net photocurrent vs. position over the scanned area of the sample show dramatically the effect, obtained in previous MIS measurements, that under a high cathodic potential (at reverse bias) the saturating photocurrent is independent of the presence of the surface dislocation loops. When a slight cathodic potential is present the presence of dislocations leads to much lower photocurrent.

In Figs.5-2 and 5-3 we show net photocurrent vs. applied potential curves for the PEC and the MIS solar cells on undamaged and damaged samples obtained by subtracting the dark J-V characteristics from those under illumination. In Fig.5-2 we show the results where the damage is produced by

0.05 μm and 0.1 μm grit sizes of alumina. In Fig.5-3 we show the results where the damage is produced by 0.3 μm and 1 μm diameter alumina grit. On both graphs are shown results for the damage-free silicon case. The voltage axis for PEC data must be normalized because with PEC solar cells the voltage is measured relative to a particular reference electrode which for our purpose is at an arbitrary potential. Thus there is no relationship between V = 0 on MIS solar cell and V = 0 (vs. SSE) with the PEC solar cell. To normalize the curves we simply have adjusted V = 0 position so that for the undamaged cells the decrease in photocurrent curves start at the same place on the graphs for the two cases. The current axis is adjusted experimentally by controlling the light intensity for the two types of measurements so that the saturation photocurrent in both cases is in the order of 10 mA/cm^2.

It is seen that the the effect of the damage on both the MIS and the PEC J-V characteristics is qualitatively the same i.e, the forward characteristics are degraded lowering the open circuit voltage, the fill factor and often the short circuit current. However, the reverse saturation photocurrent seems to be independent of the size of the particles used for polishing. The case of PEC solar cells is similar to that of MIS cells but there are slight differences. A slight but systematic lowering of the photocurrent with increasing damage size is observed in the PEC solar cells. However the lowering is small. The fact that the lowering of the saturation photocurrent of the Si

PEC cells is small is readily appreciated when one recalls that in TiO_2 PEC cells the photocurrent is reduced by two orders of magnitude in the presence of even less damage (0.3 μm)[97].

In Fig.5-4 is shown a comparison of the MIS and the PEC illuminated characteristics with in each case no oxide present at the surface of the sample. "No oxide" means that the sample was rinsed in HF just prior to the actual measurement of J-V characteristics. This has been shown[107] to leave an oxide of 10-15 Å thickness on the sample. In the case of the MIS solar cell the aluminum metal electrode is deposited over this area and hence the oxide is not expected to grow substantially more. In the case of the PEC sample after the HF rinse the sample is immersed in an aqueous solution containing potassium ferrocyanide which is a good stabilising agent for the silicon[108] and will maintain the oxide with no further growth as long as high hole currents to the surface are not allowed. It is observed in this comparison where the oxide is not carefully prepared that the PEC solar cells show a substantially better characteristic than the MIS solar cells. However, with an oxide, as is the case in Fig.5-2 and 5-3, the MIS solar cells show characteristics of equal quality to those of PEC solar cells[109].

It is observed in the PEC characteristics in the dark that the presence of ferricyanide ions in solution has a significant effect on the dark J-V characteristics of the diode. This was observed with Fe^{+3}(EDTA) by Sears[39] but was

not analyzed. Fig.5-5 shows the results of the injection curves associated with ferricyanide as a function of the length of the dislocation. It also shows a curve measured with the deepest dislocation loops (those produced by 1 um Al_2O_3) showing that there is negligible excess current without the $Fe(CN)^{-3}_6$ ion present. This latter curve is to indicate that the reverse current does not arise from bulk electron-hole generation process (which would be independent of the presence of the $Fe(CN)^{-3}_6$ ion) but must result from the injection of carriers into silicon from the ferricyanide. It is observed that the deeper the dislocation the higher the reverse dark current. Further, the shape of the excess current as a function of voltage depends on the length of the dislocation.

5.1.1 Discussion

In Figs.5-2 and 5-3 above, where the results with MIS and PEC solar cells are compared, it is shown that indeed the photocurrent does saturate essentially to the same value in the reverse direction (or at cathodic potential) independent of the presence of a layer of dislocations at the surface. Qualitatively this shows clearly the need for conductance through the dislocations, because if the dislocations were non-conducting and simply recombination centers, most of the minority carriers reaching the dislocations would be lost regardless of the applied bias. We note that the depth of the dislocations (1

μm) is larger than the depth of the surface space charge region, expected to be a few hundred nm, so in this case especially the dislocations penetrate into the bulk where they can act as recombination centers. The photocurrent under forward bias, associated with majority carriers captured at the dislocations to recombine with the minority carriers, is dependent on the length of the dislocations as expected, as observed experimentally for both the MIS and the PEC solar cells.

The PEC results showing dark injection current from ferricyanide suggest strongly, again, that the dislocations must be conductive. First, it is clear that the excess current is associated both with the $Fe(CN)^{-3}_{6}$ ion and the dislocation. If the holes could not move through the dislocation the dislocation would then be acting as a surface state, presumably, injecting the holes into the valence band. This is considered unlikely for two reasons: First, such a surface process would not depend on the length of the dislocation, and second, the distribution of energy levels of the ferricyanide is such that it would be more likely to inject holes directly into the valence band than via the dislocation[14,39]. If we assume that the concentration of the dislocation at the surface is independent of the particle size used for lapping and the only major difference in the samples is the length of dislocation (as indicated by results in section 4.2) the result strongly suggests that the holes do move along the dislocation.

5.1.2 Conclusions

The PEC measurements, of parallel MIS samples with surface damage, showed several useful results. First, it showed further indication of conductivity on dislocations, as indicated by the excess current associated with injection of holes by ferricyanide. The current due to such injection increased rapidly with the length of dislocation. The observation that the reverse saturation photocurrent is independent of the length of dislocations in both types of solar cells lend further support to conducting dislocations[109].

Second, it showed that although good PEC and good MIS solar cells show similar response to damage, the PEC cell is much less sensitive to an inferior oxide layer, in particular to silicon with no surface oxide. This characteristics of PEC cell has been suggested before, but to our knowledge it has not been experimentally demonstrated by a direct comparison for the two types of cells.

To distinguish between recombination at dislocations and shunting at dislocations would have been very difficult were it not for the unique configuration in the surface dislocation loops and were it not for the unique characteristics of hole injection by ferricyanide ions in solution.

5.2 Hydrogen Passivation of Dislocations

There have been many earlier studies of hydrogen passivation, particularly passivation of grain boundaries[102,110-114]. However, some recent studies using deep level transient spectroscopy (DLTS) have shown that dislocations introduced into n-type silicon by plastic deformation can be effectively passivated by hydrogen as well[115,116]. In general, it has been concluded in solar cell passivation studies that the major part of the improvement is in the open circuit voltage and in the short circuit current, although the results are somewhat irreproducible from paper to paper[112,113].

It was anticipated that with the mathematical model for the effect of the dislocation loops one should be able to determine more accurately what parameters are being improved during the hydrogen passivation treatments. Also, it was anticipated that using PEC cells with hole injection by ferricyanide[109], the interpretation should be simplified. We hoped to obtain a fairly clear-cut indication of whether the changes in resistivity of the dislocations or the density of recombination centers at the dislocations dominated the improvement associated with passivation. However, it will become clear later that the results are more complex than anticipated.

5.2.1 Model

Presumably, the major effect of hydrogen treatment on dangling bonds is formation of a covalent bond between the hydrogen atom introduced into the crystal and the dangling bond in the silicon [111]. This, in principle, should remove dangling bond energy levels from the band gap, as is found to occur with dangling bond interface states between the silicon and the silicon dioxide. The removal of such dangling bond levels from the dislocations should have two effects: first, lowering the conductivity along the dislocations, second, lowering the density of recombination centers at the dislocations.

A "high" conductivity along the dislocation has two effects according to the conductivity model[105]: one under reverse bias, the other under forward bias. Under reverse bias the dislocations will tend to conduct minority carriers to the surface. This will increase the saturation photocurrent because minority carriers captured at the dislocations will find their way to the surface and be counted as current. With a low conductivity dislocation, on the other hand, the minority carriers trapped at the dislocations can only recombine. Thus, passivating the dislocation (and lowering its conductivity) should have the effect of lowering the reverse bias saturation current and probably of lowering J_{sc}, the short circuit current. Under forward bias on the other hand, the conducting dislocations will allow excess majority carrier current to flow to the

surface along the dislocations. The model shows that at a given forward bias voltage, the forward current is greater in the case of a damaged sample (i.e., with dislocations present in the sample) than in an undamaged one. Thus, the passivation of the dangling bonds by hydrogen atoms (lowering its conductivity) should cause an increase in V_{oc}, the open circuit voltage.

In Fig.5-6 we show the results of a numerical analysis of the model in chapter 4, where we analyzed with a simple model the effect of passivating the dislocations. In curve A we show the photocurrent-voltage curve for a set of "typical" parameters (as found by fitting curves in chapter 4) for conductivity s, and the linear density of recombination centers p_d, in damaged sample. In curve B we show the effect of decreasing the conductivity as would be expected by passivation (while leaving p_d constant). As shown, simply decreasing the assumed conductivity leads to the qualitative behavior as described in the preceding paragraph, lowering J_{sc} but improving V_{oc}.

The influence of the passivation on recombination may, in the simplest model, be to decrease the density of recombination centers along the dislocation. This decrease should cause an improvement in both the short circuit current (by lowering the recombination of minority carriers) and the open circuit voltage (by lowering the forward current). In Fig.5-6 comparing curves B and C we observe the behavior, as calculated with the quantitative model, when simply assuming a lower density of recombination centers in the

model.

Thus, by this model the passivation has two effects: comparing curve A to curve B, accounting only for a conductivity decrease due to passivation it is seen the characteristics are somewhat degraded. However, as in curve C, adding in the expected improvement in recombination, the short circuit current characteristics are restored to closer to the original (damaged) values, and the open circuit voltage characteristics are substantially improved. In fact, experimentally we have not observed an overall decrease in the short circuit current as predicted by the model (compare curves A, before passivation, with C, after passivation). Thus, the model with the parameters used overemphasizes the degrading effect of the conduction along dislocations. However, as it will be shown, a substantial lowering of both conduction and recombination center density is not properly reflected in the solar cell parameters, and the model helps to explain why the improvements are not observed upon passivation to the extent that it could have been expected.

Since it was anticipated that PEC measurements with hole injection would also be of assistance in interpreting results, passivated and unpassivated samples identical to those used for MIS measurements were again sent to University of Belgium where electrochemical measurements were carried out for comparison. The damaged samples were passivated as described in section 3.4. In cases where MIS and PEC characteristics were to be compared, the samples were taken from neighboring areas of a silicon wafer, and

the samples were passivated together.

5.2.2 Results and Discussion

Passivation of the dislocations should, of course, not only affect the photocurrents but also affect the dark currents. The dark current in the reverse direction, dominated by the Sah-Noyce-Shockley type minority carrier generation[82,117] at the dislocation, should be lowered by passivating the dangling bonds. The forward characteristics of the diode should be also improved by passivation because with the non-passivated material majority carriers can readily flow to the surface along the dislocation, whereas once the dislocation is passivated the majority carrier flow is much lower. Thus, examining the dark J-V characteristics of the diodes on passivated and non-passivated material gives one an understanding of the effect of passivation on both recombination and resistance associated with dislocations[118].

In Fig.5-7, typical curves are shown for the dark J-V characteristics for MIS cells, indicating the effect of passivation on the reverse and forward directions of the diode characteristics. Strong effects are observed in both directions, suggesting both the density of recombination centers and the conductance are significantly lowered.

Fig.5-8 shows typical J-V characteristics for illuminated solar cells with varying degrees of damage, and also the effect of passivation. In all cases the samples compared are made on adjacent parts of a single silicon

wafer which have undergone identical treatments except that in one case the sample has been subjected to a passivation treatment before the solar cell is fabricated. It is clear that passivation does tend to improve the characteristics, but perhaps not as effectively as one would expect, considering the dramatic results of Fig.5-7.

In Fig.5-9 we show a summary of a large amount of data showing how the improvement in the fill factor FF, the short circuit current density J_{sc}, and the open circuit voltage V_{oc}, depend on the temperature at which the sample is passivated. All of the samples studied are included in the plot, leading to the noted standard deviation of the data. The scatter in the data, presumably, arises in part due to the variations in initial damaging of the sample, and in part due to variations in the actual passivation treatment (These results are not restricted to samples prepared or passivated together). However, it is clear that there is, in general, an improvement in the sample characteristics associated with the hydrogen passivation. And, as expected, passivation improves the cell parameters with increasing temperature, saturating at higher temperatures (Fig.5-9).

Fig.5-10 shows the net photocurrent-voltage curve with an MIS as compared to a PEC solar cell made from material prepared "identically". As before the voltage axis for the PEC results (normally expressed as volts vs. SSE reference electrode) was adjusted by shifting it so that the J-V characteristics for an undamaged PEC cell has the

same V_{oc} as the corresponding MIS cell. The active electrolyte in the PEC studies was a potassium ferrocyanide/ferricyanide mixture. The PEC cell for both the unpassivated and passivated samples show an extra current wave over the MIS cell results. The unpassivated material shows a very small current wave. The passivated PEC solar cell has a very strong double wave characteristic, which is difficult to explain as it does not seem to appear in the MIS solar cell characteristics. Were it not for the MIS results one would assume that we have a heterogeneous surface with part of the surface completely passivated, the other part unpassivated. However, if this were the explanation one would expect the same result with the MIS cells, and this has not been observed.

It is observed in Fig.5-11 that the dark characteristics of the unpassivated sample show such a wave in the same region of the photocurrent of the passivated sample. It should be noted, as shown in previously (see section 5.1.1), that the dark current in the presence of ferricyanide is due to hole injection from the ferricyanide ion. In turn, we note in Fig.5-6 that hydrogen passivation has an exceptionally strong effect, lowering the hole injection in the dark. By comparing Fig.5-3 to curves A and B in Fig.5-11, it would appear that the dark current at negative voltages may arise from minority carrier generation, while the wave of current (Fig.5-11) at positive voltages may be associated with hole injection by ferricyanide.

An anomalous effect (which may be attributed to neutralization of boron acceptors by atomic hydrogen and thereby converting the p-type Si into n-type) is shown in Fig.5-12. For a few samples the photocurrent under negative bias was extremely low, after passivation, and a photocurrent in the positive direction was observed. Curves A and B in Fig.5-12 show such results for "identical" samples as measured by PEC and MIS techniques, respectively, showing an excess photocurrent under forward bias as observed by the PEC technique and the very low photocurrent observed both by the MIS and PEC techniques in the negative voltage direction. Curve C shows another sample as measured in the MIS technique where the total surface seems to have converted to intrinsic or high-resistance n-type as indicated by the photocurrent in the positive voltage direction. Such behavior after passivation was rare, occurring in only a few percent of the samples.

Another complicating feature is the occasional heterogeneity observed in the rising part of the photocurrent - voltage curves of both the damaged and the passivated samples. Such heterogeneity is shown in Fig.5-13 where we show a scanning light spot photocurrent pattern at -1.5 volts (SSE) for a damaged sample. Such effects were sometimes observed also with passivated samples. The worst case of heterogeneity observed is shown; normally the SLS scans are far more uniform than this. (for comparison see the equivalent SLS scans on the "normal" damaged sample in Fig.5-1).

The question arises whether hydrogen dissolved in the bulk, rather than that bonded at dislocations, could affect the results. It has been shown in studies where SIMS (secondary ion mass spectrometry) depth profiles were obtained after hydrogenation of both Si and GaAs samples that acceptor compensation (neutralization) is about 10 times higher near the surface region (several thousands of angstroms) than in the bulk[118]. However, the same studies have shown that after anealing the samples for a few minutes at a temperature less than 600° C the enhanced compensation disappears althogether. Therefore in our studies where the samples were anealed for a much longer period of time after hydrogen passivation treatment the effect of such a concentrated hydrogen layer would be negligible.

5.2.3. Conclusions

It is clear from the experimental results that passivation, in general, does improve the various characteristics of the surface dislocation loops, and hence of the solar cell[119]. The model, however, does not clearly indicate whether hydrogen passivation should provide a net improvement in all the solar cell characteristics. Different voltage regions of the characteristics could show different effects, according to the model, and the effects predicted depend on details of how the removal of the dangling bonds is assumed to affect the parameters of the model. The conclusion that the passivation of defects should sometimes improve, sometimes degrade solar cell

characteristics, may be the reason for the reasonable amount of scatter in the solar cell characteristics after passivation.

Of course, if the hydrogen tends to neutralize acceptors and make the sample intrinsic or even slightly n-type [120-122], this introduces even more complexity into the net effect to be expected from passivation.

It could be concluded that substantial work needs to be done in the area of passivation in order to be able to interpret the results in terms of a detailed model of the effect of hydrogenation of dangling bonds in silicon dislocations.

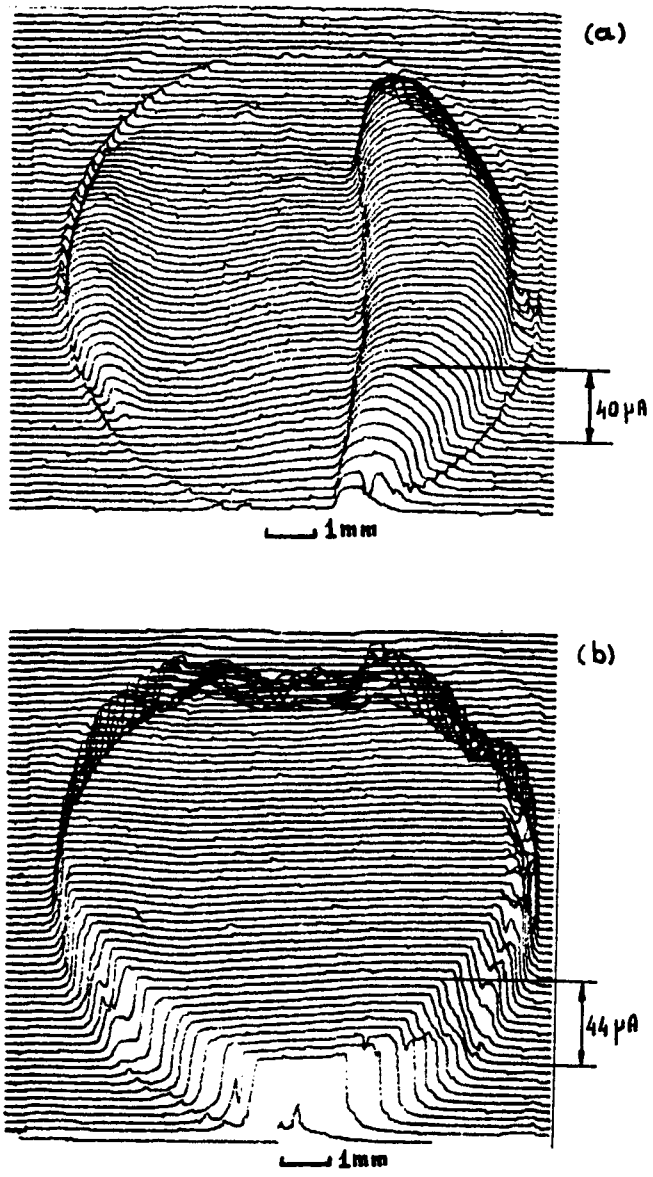

Fig.5-1 Scanning Laser Light Spot (SLS) maps at two different bias voltages on a single sample, half of which was damaged with 0.3 μm diameter alumina.
(a) slightly cathodic at -1 V (vs. SSE)
(b) highly cathodic at -1.95 V (vs. SSE).
Electrolyte composition: 0.25 M NH_4F + 0.1 M $K_4Fe(CN)_6$ + 0.01 M $K_3Fe(CN)_6$ in H_2O.

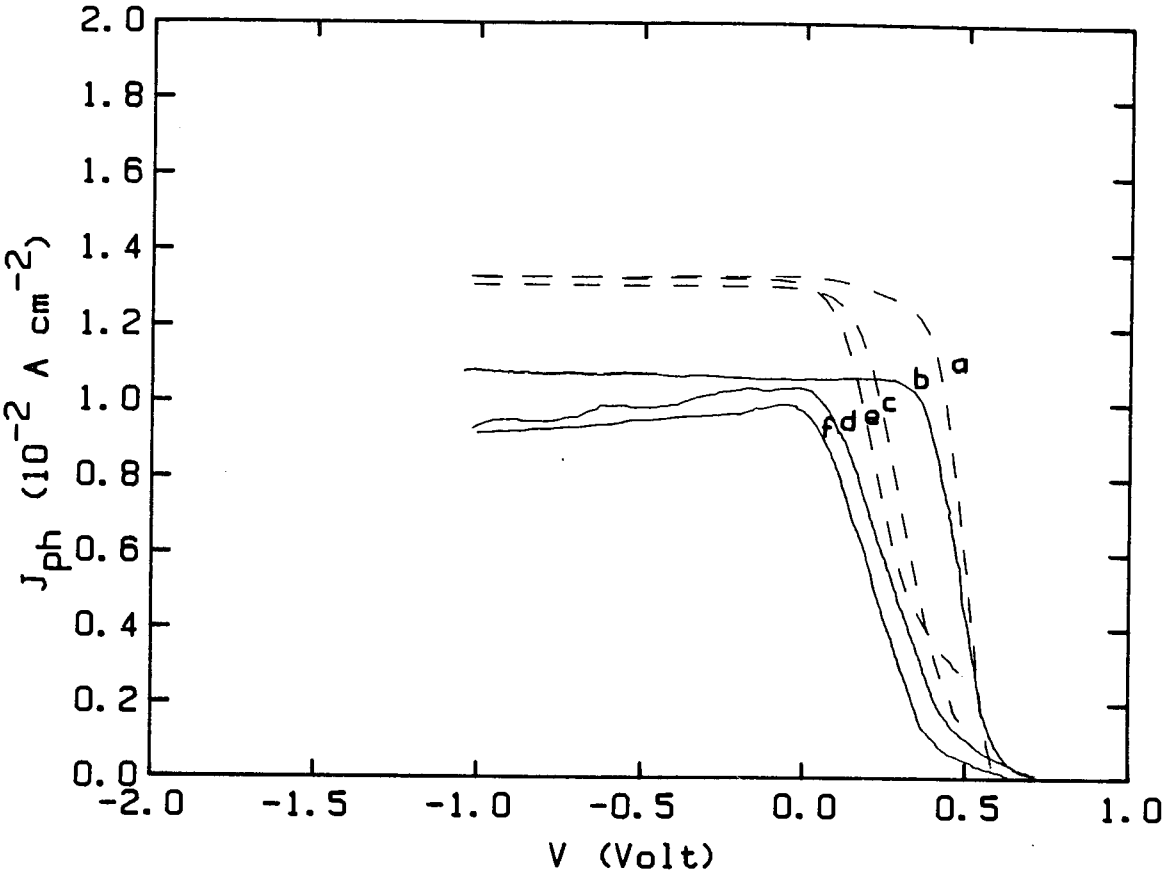

Fig.5-2 The net photocurrent, Jph vs. voltage, V for both the PEC and the MIS solar cells on damaged as well as undamaged samples (V = 0 position of PEC data is adjusted so that the the decrease in photocurrent in the undamaged cells start at the same voltage).

MIS (dashed lines): (a) undamaged (c) 0.05 μm (e) 0.1 μm
PEC (solid lines) : (b) undamaged (d) 0.05 μm (f) 0.1 μm

Electrolyte composition: 0.25 M NH_4F + 0.01 M $K_4Fe(CN)_6$ + 0.01 M $K_3Fe(CN)_6$ in H_2O.

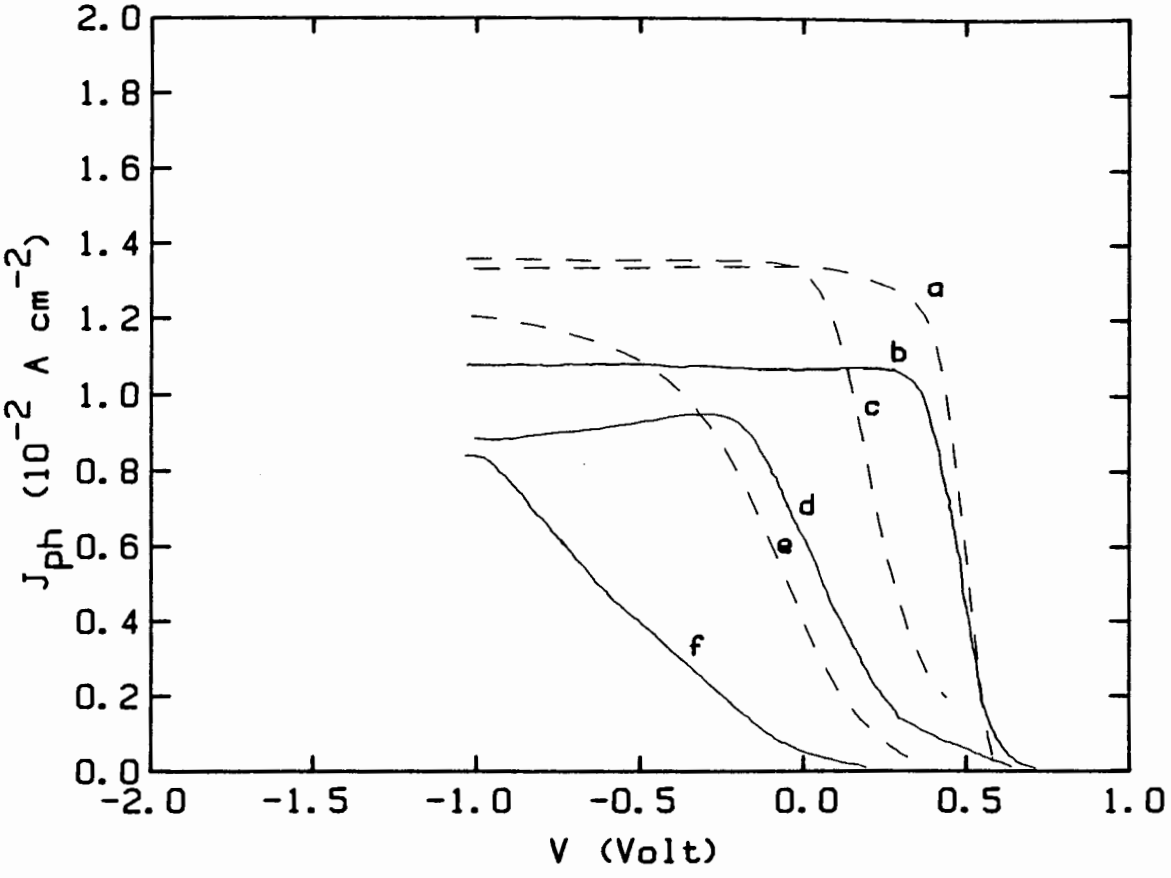

Fig.5-3 The net photocurrent, Jph vs. voltage, V for both the PEC and the MIS solar cells on damaged as well as undamaged samples (V = 0 position of PEC data is adjusted so that the decrease in photocurrent in the undamaged cells start at the same place).

MIS (dashed lines): (a) undamaged (c) 0.3 μm (e) 1 μm
PEC (solid lines : (b) undamaged (d) 0.3 μm (f) 1 μm

Electrolyte composition: 0.25 M NH_4F + 0.01 M $K_4Fe(CN)_6$ + 0.01 M $K_3Fe(CN)_6$ in H_2O.

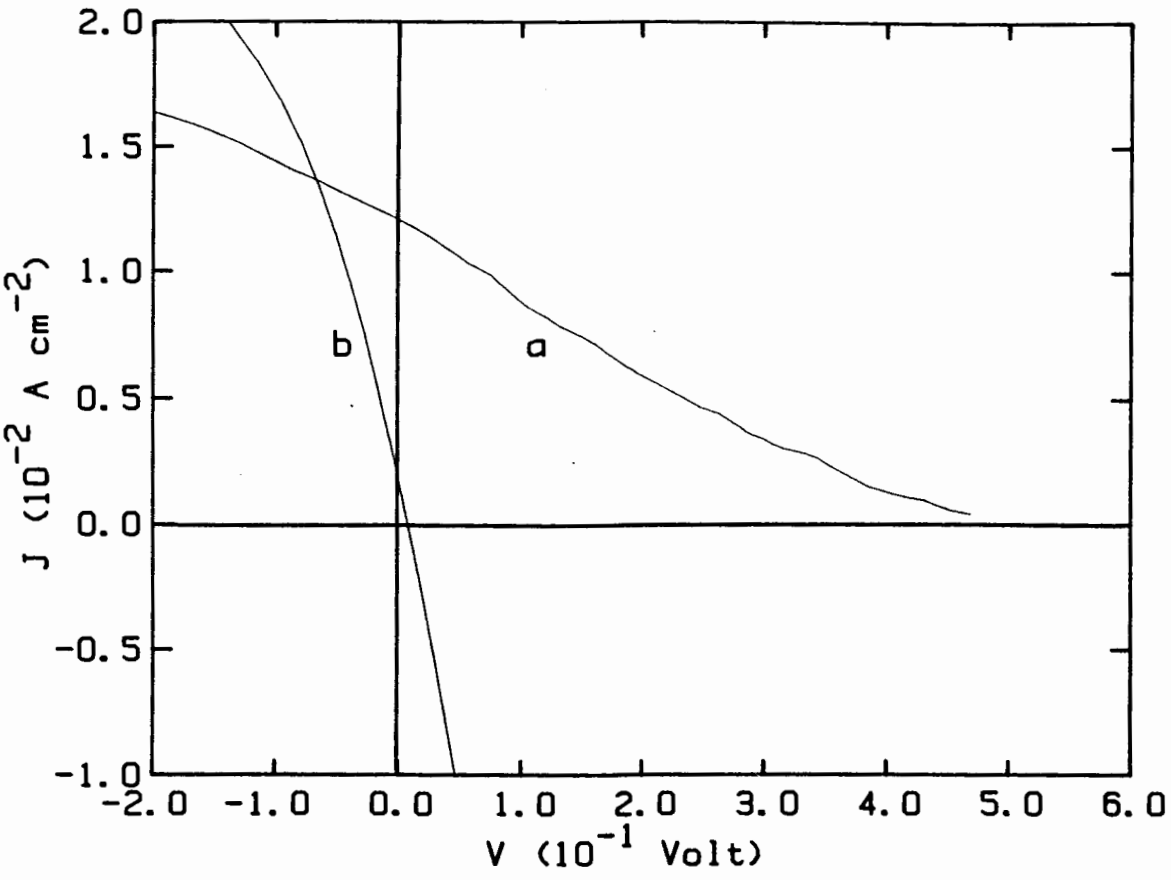

Fig.5-4 Illuminated J-V characteristics of (a) a PEC and (b) an MIS solar cell fabricated on 1 μm damaged Si samples which were given a HF rinse prior to measurement for removing the surface oxide layer. The voltage axis was adjusted for the PEC curves by shifting the zero (vs. SSE) the same way as for Figs. 5-2 and 5-3.

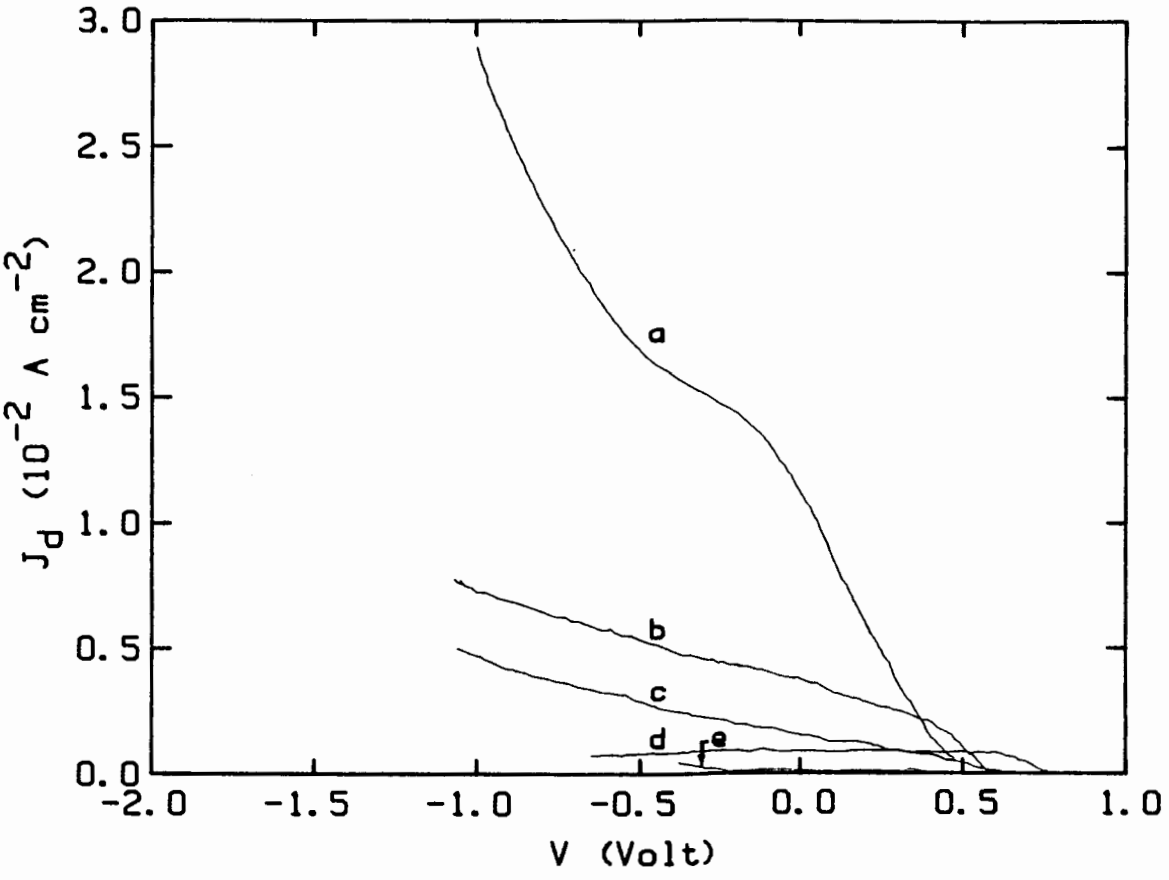

Fig.5-5 The dark J-V curves for the PEC cells with various lengths of dislocations showing that the dark current is due to hole injection by $Fe(CN)_6^{-3}$.

(a) 1 μm with $K_3Fe(CN)_6$

(b) 0.3μm with $K_3Fe(CN)_6$

(c) 0.05 μm with $K_3Fe(CN)_6$

(d) undamaged with $K_3Fe(CN)_6$

(e) 1 μm without $K_3Fe(CN)_6$

Electrolyte composition for (a), (b), (c) and (d): 0.25 M NH_4F + 0.01 M $K_4Fe(CN)_6$ + 0.01 M $K_3Fe(CN)_6$ in H_2O.

Electrolyte composition for (e): 0.25M NH_4F in H_2O.

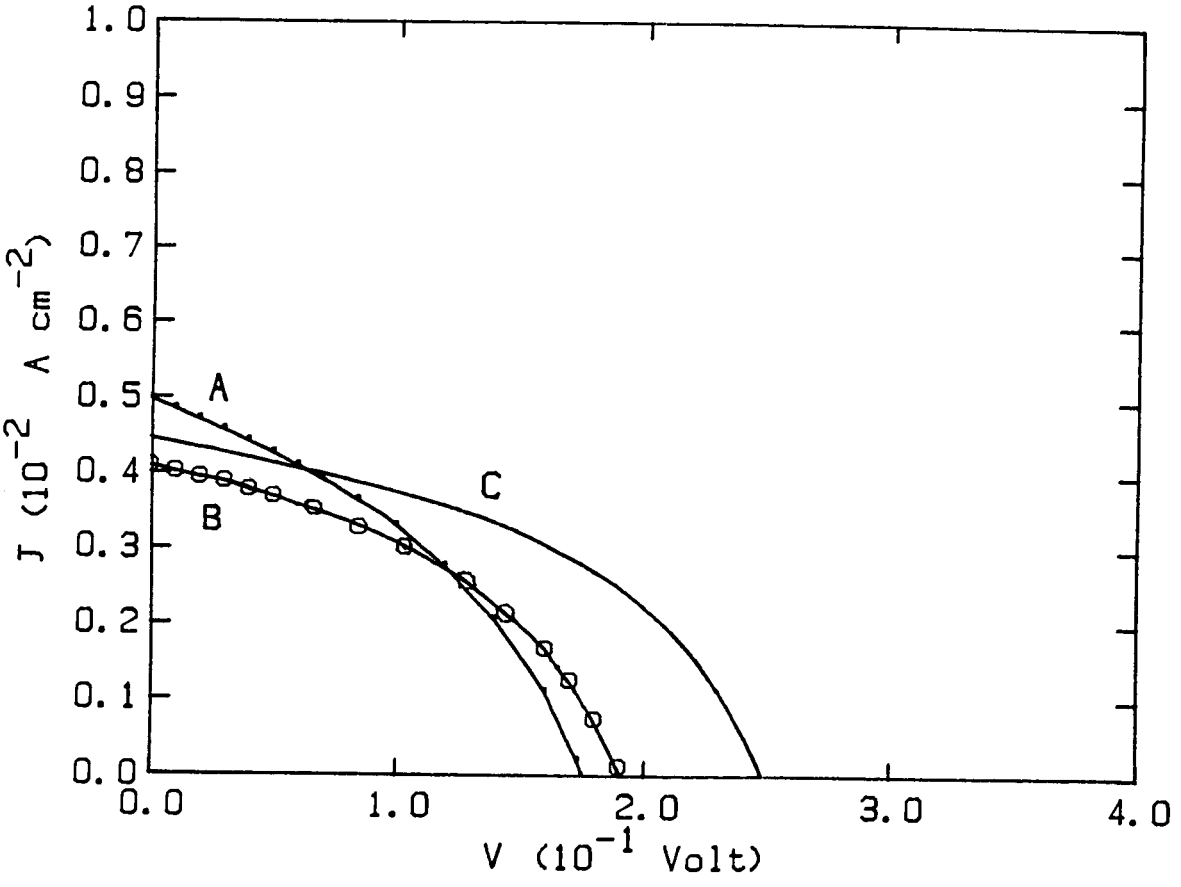

Fig.5-6 Calculated J-V characteristics according to dislocation conductivity (DLC) model. With s = dislocation conductivity, p_u = linear density of dislocation states (recombination centers),

(A) $s = 1 \times 10^{-15}$ cm ohm^{-1}, $p_u = 3 \times 10^{7}$ cm^{-1}.

(B) $s = 5 \times 10^{-16}$ cm ohm^{-1}, $p_u = 3 \times 10^{7}$ cm^{-1}.

(C) $s = 5 \times 10^{-16}$ cm ohm^{-1}, $p_u = 3 \times 10^{6}$ cm^{-1}.

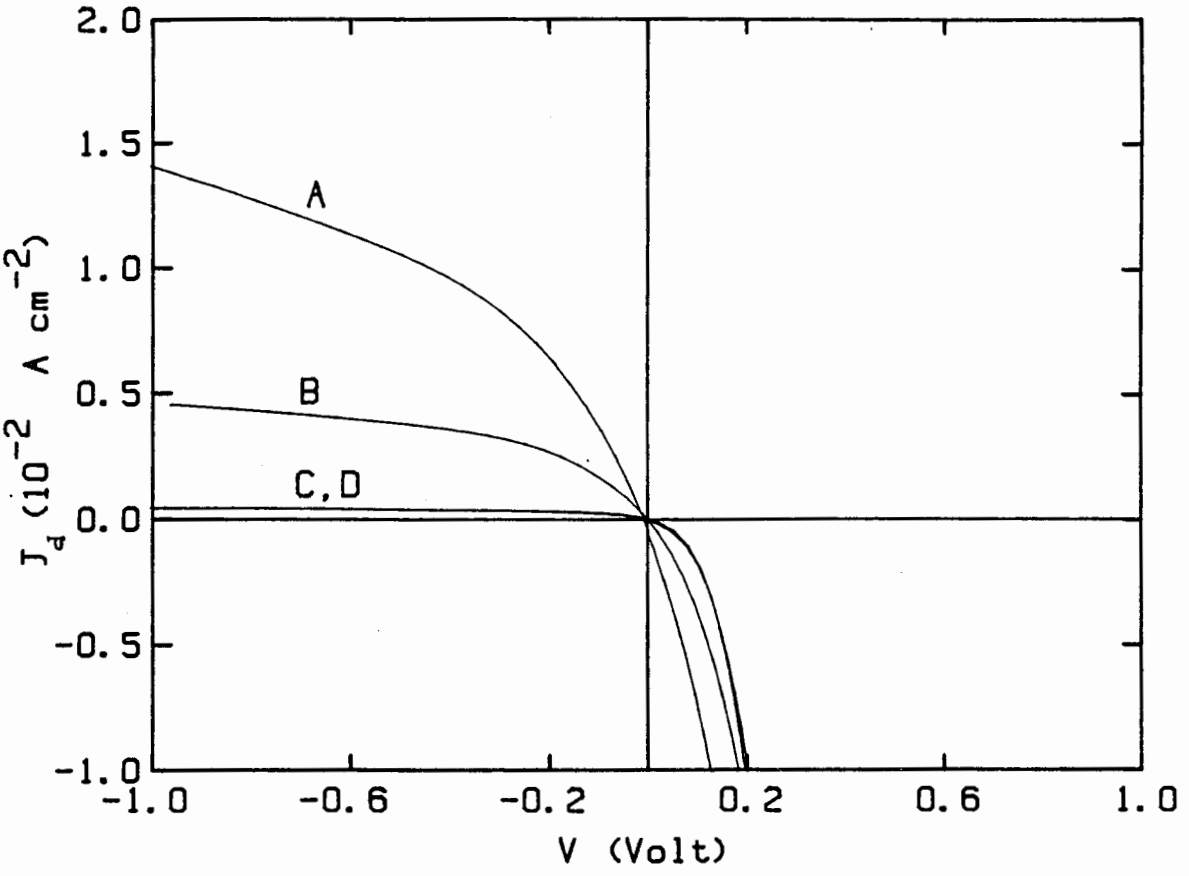

Fig.5-7 Dark J-V characteristics of MIS cells with 1 μm damage.

(A) unpassivated

(B) passivated for 3 hr. at room temperature

(C) passivated for 3 hr. at 450°C

(D) passivated for 3 hr. at 525°C.

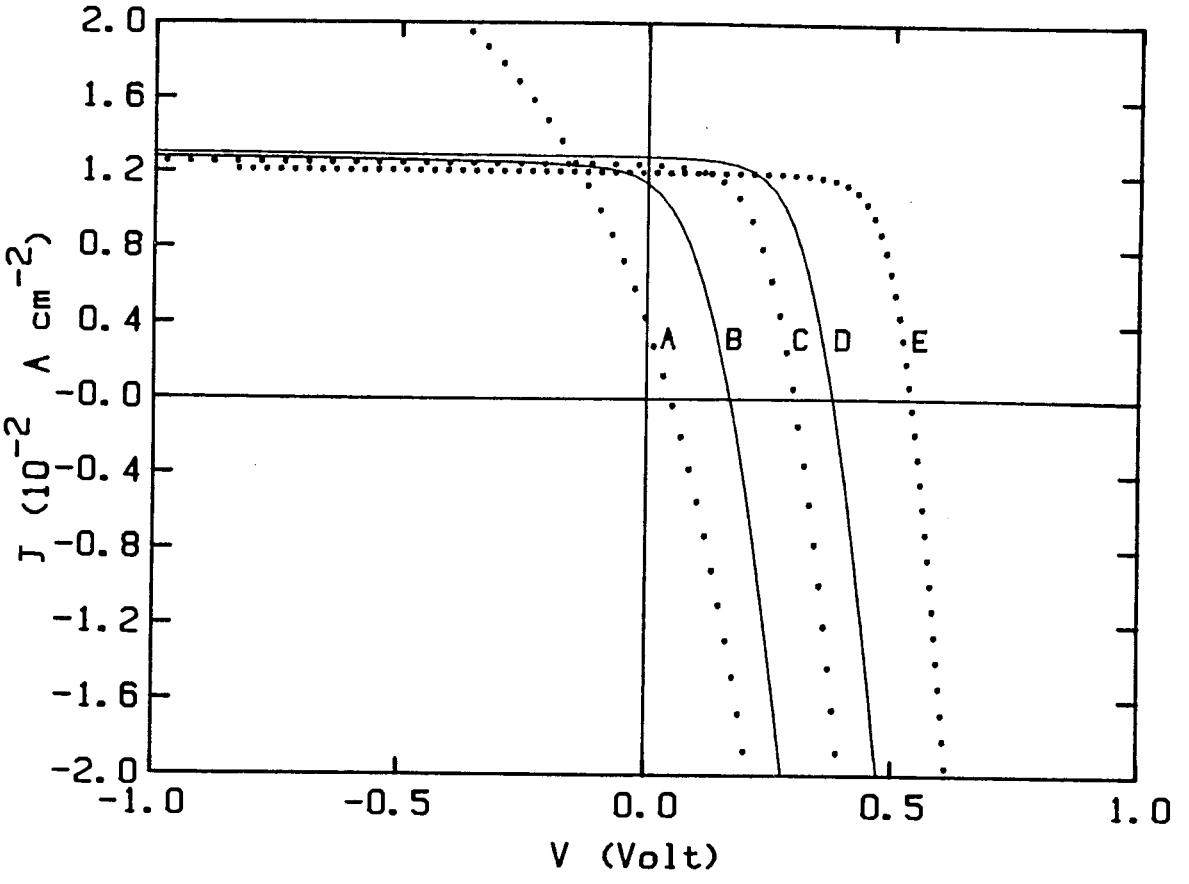

Fig.5-8 Illuminated J-V characteristics of MIS solar cells with various damage and the effect of passivation.
AM2 illumination set at 100 mW cm^{-2}.

Unpassivated samples (dotted lines):

(A) 1 μm damage

(C) 0.1 μm damage

(E) undamaged sample

Passivated samples (solid lines):

(B) 1 μm damage + passivated at 525 ^{o}C

(D) 0.1 μm + passivated at 525^{o}C

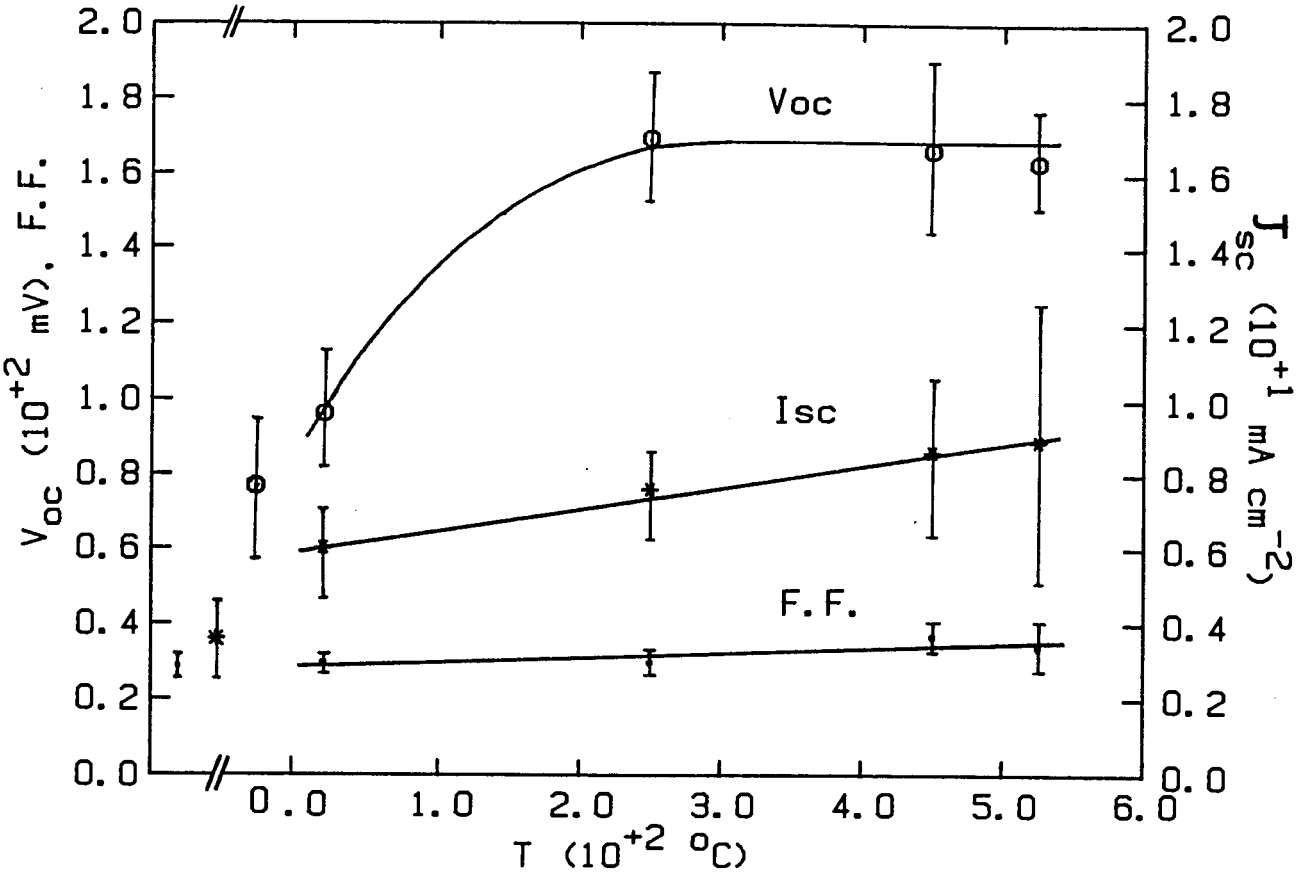

Fig.5-9 The effect of passivating 1 μm damaged MIS cells at different temperatures. At the extreme left of the plot, the cell parameters (open circuit voltage Voc, short circuit current Jsc, and fill factor FF) of the unpassivated cells are shown for comparison.

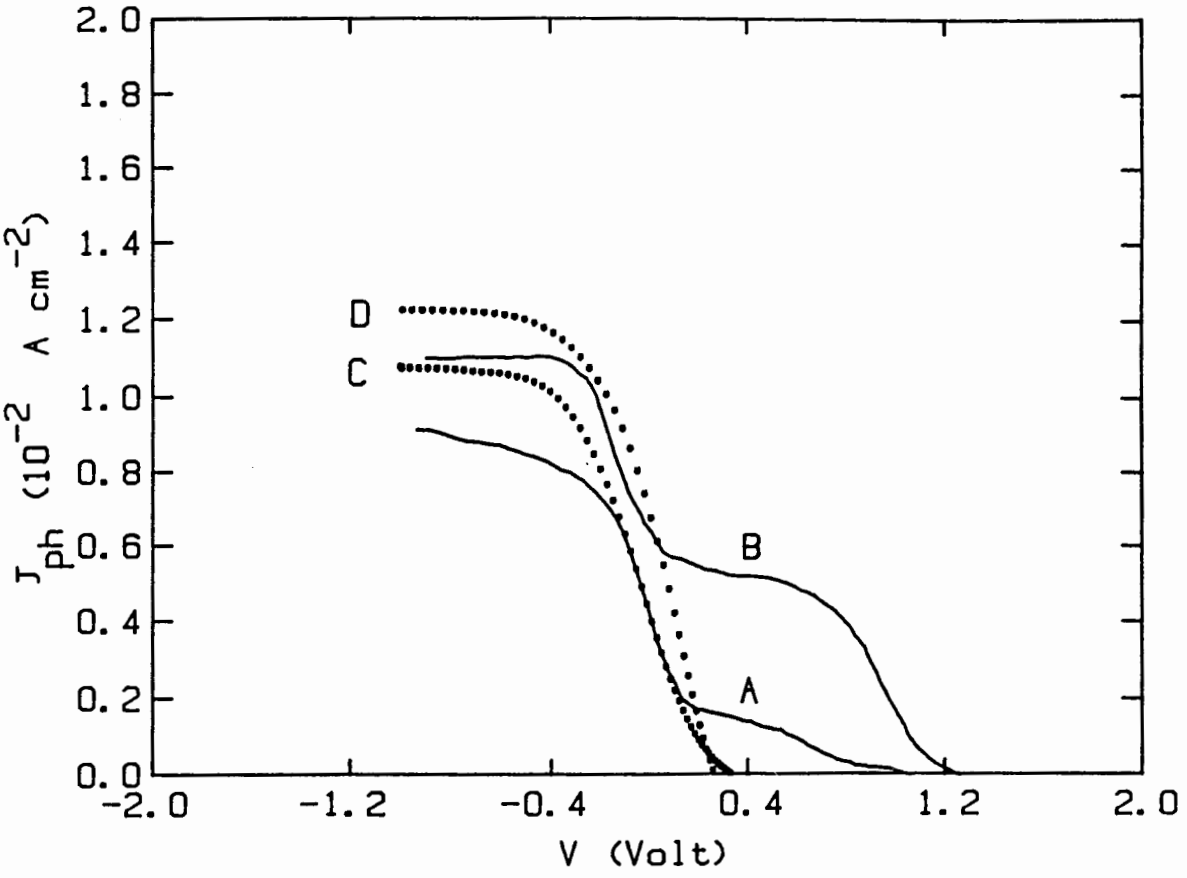

Fig.5-10 The net photocurrent vs. voltage of MIS and PEC cells fabricated from unpassivated and passivated Si samples.

PEC cells (solid lines):

(A) 1 μm damaged

(B) 1 μm damaged after passivating at 450°C

MIS cells (dotted lines):

(C) 1 μm damaged

(D) 1 μm damaged after passivating at 450°C

Electrolyte composition: 0.25 M NH_4F + 0.1 M $K_4Fe(CN)_6$ + 0.01 M $K_3Fe(CN)_6$ in H_2O.

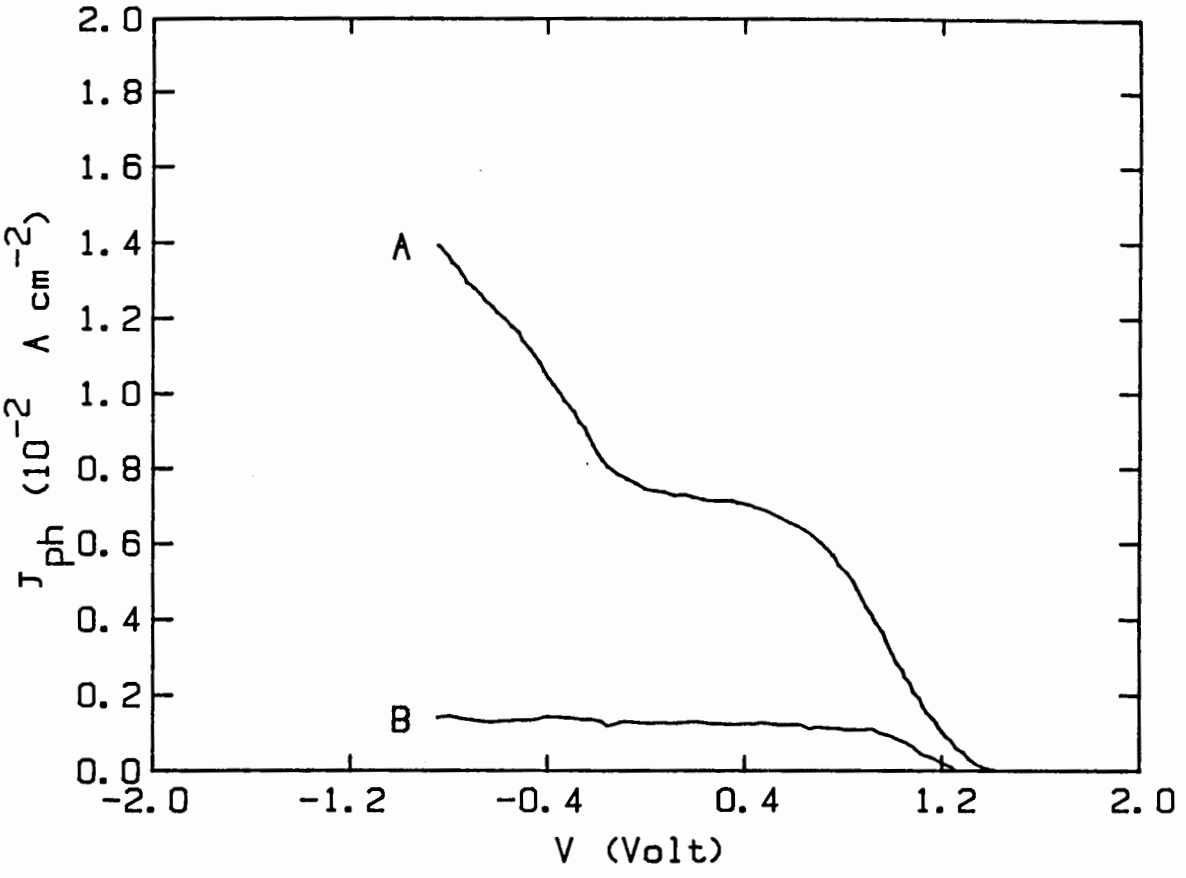

Fig.5-11 The dark current of PEC cells with 1 μm damage.
(A) unpassivated
(B) passivated at 450°C.
Electrolyte composition: 0.25 M NH_4F + 0.1 M $K_4Fe(CN)_6$ + 0.01 M $K_3Fe(CN)_6$ in H_2O.

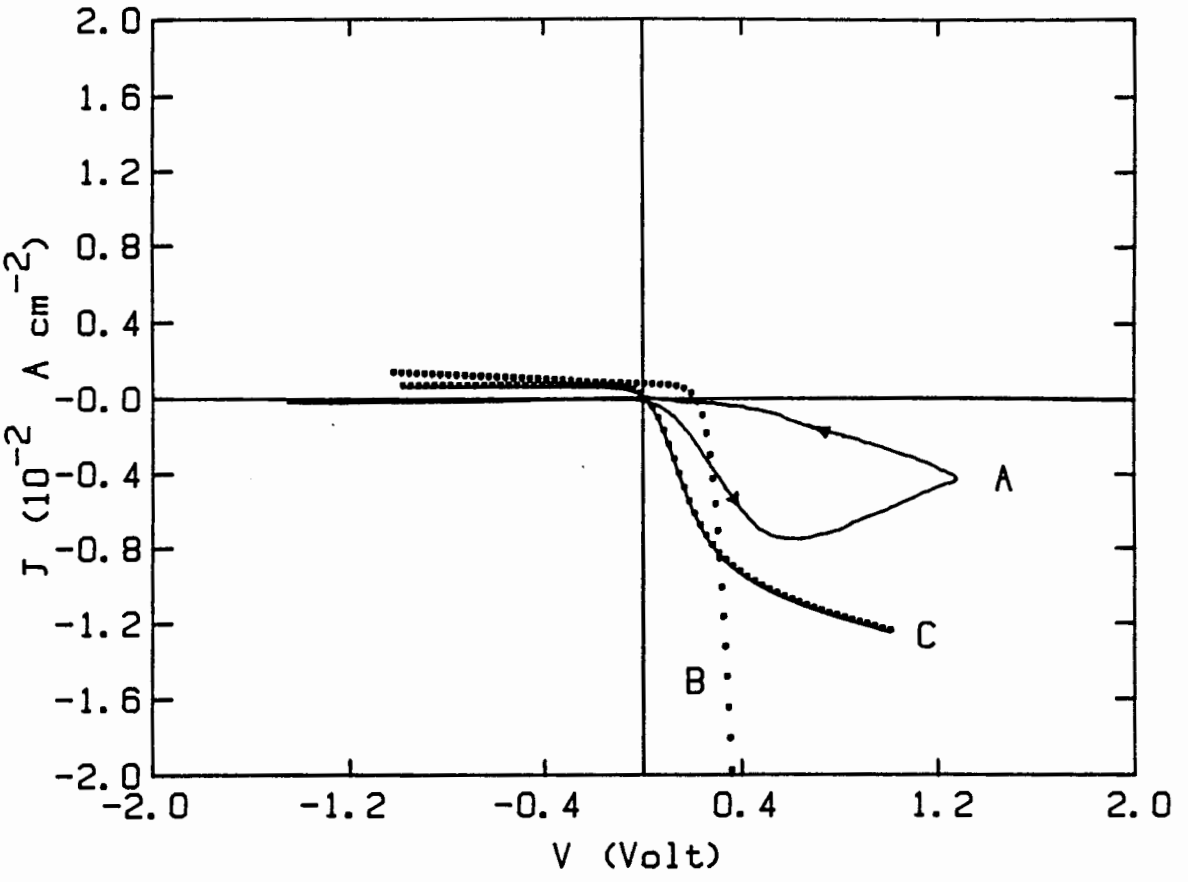

Fig.5-12 The anomalous J-V characteristics of passivated samples.

(A) The net photocurrent of 0.3 μm damaged PEC cell

(B) The total J-V of MIS cell made from the same sample in (A)

(C) MIS cell (1 μm damaged) with a pronounced anomaly

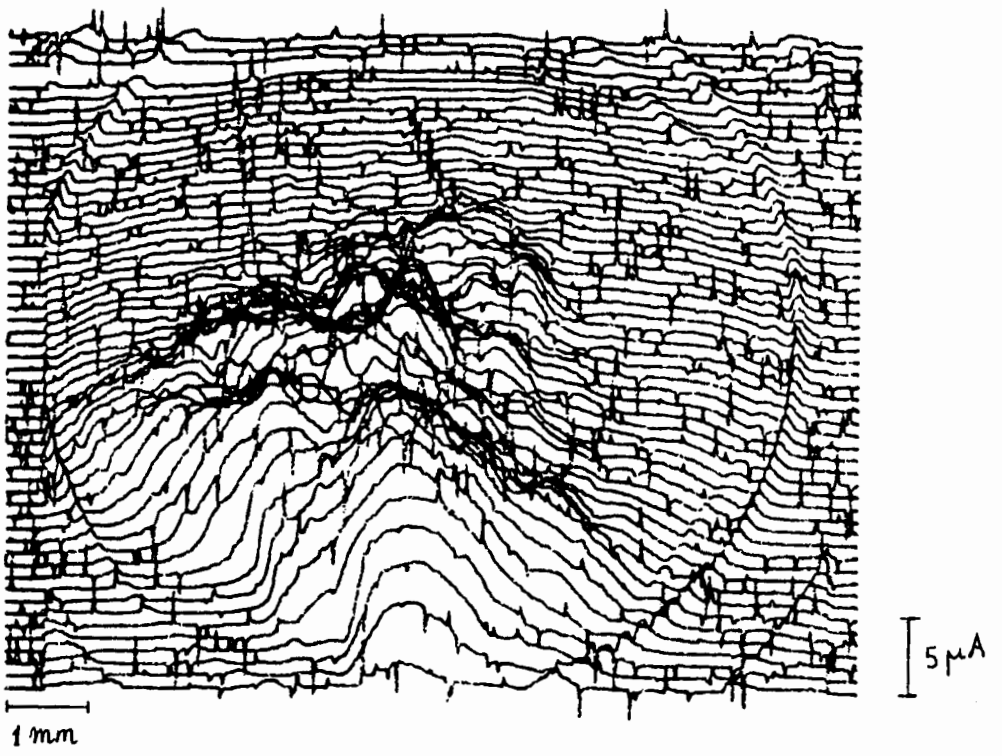

Fig.5-13 The scanning laser spot (SLS) map of a damaged (0.3 μm) sample showing heterogeneity. The sample is held at -1.5 V (vs. SSE).

Electrolyte composition: 0.25 M NH_4F + 0.1 M $K_4Fe(CN)_6$ + 0.01 M $K_3Fe(CN)_6$ in H_2O.

CHAPTER VI

TEMPERATURE DEPENDENCE OF CELL PARAMETERS

6.1 MIS structure as an n^+p junction

As discussed in Chapter 2, Al-SiO_x-pSi structure resembles a n^+p junction due to the inversion of the semiconductor surface owing to the low work function of Al. The dominance of minority carriers over the transport properties of this structure has been experimentally established by Tarr and Pulfrey[123]. In view of this evidence it would appear that the dependence of the solar cell parameters under illumination with temperature of this structure should also be similar to that of a n^+p junction.

6.1.1 Results and Discussion

To verify this, dark and illuminated characteristics were recorded for several MIS structures (undamaged) at different temperatures in the range 100 - 300 K. The cells were measured by mounting them on a Cu finger in a cryostat designed for illuminating through a quartz window where the cell temperature could be controlled using liquid N_2. A xenon arc lamp along with AM2 (Oriel) filters were used as the light source. All the cells measured showed a similar behavior, and results for a representative sample will be presented. All low temperature measurements were conducted at an AM2 illumination intensity of 50 mW cm^{-2}.

Fig.6-1 shows the dark J-V characteristics of a

typical cell (P100) at different temperatures. As well known for MIS diode characteristics[124], three distinct regions are apparent, one at low bias (region A), one at mid bias (region B), and one at high bias (region C). All three regions are clearly seen at all temperatures. More importantly, the interesting region for solar cell operation, i.e., the mid bias region which is dominated by the diffusion component of the current, shows a linear behavior in the semilogarithmic plot enabling one to extract the diode parameters (ideality factor, n and reverse saturation current, J_o). Table 6-1 show the parameters obtained.

The temperature variation of V_{oc}, J_{sc}, FF and η of the MIS cell are shown in Fig.6-2. The general behavior is quite similar to that of a conventional pn junction cell[125]. The V_{oc} and the J_{sc} vary linearly with T while the FF and the η become sublinear at very low T. However, we can define temperature coefficients for all parameters in their linear regions by

$$M = M_o + a_m T \qquad (6-1)$$

where M is the measured parameter (= V_{oc}, J_{sc}, FF or η), M_o is the value of the parameter at 0 K obtained by linear extrapolation, a_m is the temperature coefficient for the measured parameter, and T is the temperature in K.

Experimentally, it was found that the $a_{V_{oc}} = -2.03 \pm 0.18$ mV K^{-1}. This value compares very well with that for a

pn junction cell[117], which is about - 2 to - 3 mV K^{-1}. The reported value[126] for a Schottky barrier cell where a carefully prepared insulator is absent is 2.3 mV K^{-1}. The open circuit voltage can be given by (see Eqn.2-9)

$$V_{oc} = n(kT/q) \ln (J_{sc}/J_o). \qquad (6-2)$$

In Eqn.(6-2) n, J_{sc} and J_o all vary with temperature. However, one can use Eqn.(6-2) to calculate V_{oc} as a function of temperature with the experimentally obtained values of other parameters. This was carried out and the result is shown as the dashed line in Fig.6-2 indicating an excellent fit to the V_{oc} data. The value for $a_{V_{oc}}$ obtained from Eqn.(6-2) is 2.07 +/- 0.15 mV K^{-1}. It is well known[125] in pn junction work that the effect of the illumination intensity on the temperature dependence of most of the cell parameters should not have a much significance within certain limits, and the temperature dependence of V_{oc} is largely determined by the variation of the intrinsic carrier density n_i with temperature.

We measure $a_{J_{sc}}$ = .011 ± .001 mA cm^{-2} K^{-1}, a_{FF} = - 0.0007 ± .0002 K^{-1} and a_η = - 0.01 ± .002 $\%K^{-1}$. The latter two parameters are for near room temperature region. Table 6-2 shows the corresponding values for a n^+p silicon solar cell for comparison, obtained from Ref.125 where results for various illumination intensities are reported for n^+p structures with similar base resistivity as the p-Si used in this study. It can be seen that the

temperature coefficients for the two types of cells are quite similar.

As it has been shown previously, for a Schottky barrier cell[127], the positive temperature coefficient of J_{sc} must be mainly due to the decrease in the absorption coefficient with temperature. The negative temperature coefficient of the silicon band gap[128] may also contribute by reducing the useful wavelength range by 0.04 um when T is lowered to 100 K from 300 K.

Since, η = FF $V_{oc}J_{sc}/P_{in}$ where P_{in} is the input power density, we can write

$$a_{\eta} = (FFV_{oc}a_{J_{sc}} + FFJ_{sc}a_{V_{oc}} + V_{oc}J_{sc}a_{FF})/P_{in} \qquad (6-3)$$

Eqn.(6-3) shows that a_{η} depends on all three other coefficients. The temperature coefficient of the FF is negative and very small while that of η is also negative and less than the lowest published value for a silicon cell[125]. Krawyczyk et. al.[129], have found a_{η} to be -0.05 to -0.1 $\%K^{-1}$ for an MIS structure with the insulator thickness > 20 Å, while, the lowest value reported to date for a silicon pn junction cell is -0.060 - 0.064 $\%K^{-1}$ [125,129]. In this sense the MIS structures we have studied can almost be considered as constant efficiency devices[130].

6.2 Effect of Temperature on Damaged Cells

When similar measurements were carried out on MIS cells with damage, a peculiar difference in their current-voltage characteristics was observed. The behavior of the slope of the dark or illuminated characteristics at high forward biasses was seen to be different (Fig.6-3). Fig.6-4 shows the temperature variation of other cell parameters for a 1 μm damaged MIS cell(P111A). The analysis of temperature variation of these parameters is complicated because of the many variables involved. However, by considering a less obvious behavior one can draw some conclusions about the current along dislocations at high forward voltages.

By defining a parameter called the differential resistance, r_d as the inverse slope of the current-voltage data at higher ($>> V_{oc}$) forward bias and plotting this with temperature for both undamaged and damaged cells, the effect of the dislocations could readily be seen (Fig.6-5). It is seen that for the undamaged cell r_d is almost a constant while for the damaged sample it increases with decreasing temperature.

By differentiating Eqn.4-19 with respect to V_o using Eqn.4-12, for $V_o >> V_{oc}$ where C is neglected compared to the exponential term and rearranging, we obtain

$$J_{d1} = (2kT/qD_{DL})(1/ r^{d}_{d}(T) - a/ r^{u}_{d}(T)) \qquad (6-4)$$

where r^{d}_{d} and r^{u}_{d} are the experimentally determined

differential resistances of damaged and undamaged cells, respectively. Eqn.(6-4) allows one to determine the behavior of J_{d1} with temperature. With data in Fig.6-5 and using Eqn.6-4 the variation of J_{d1} with T can be obtained, and this is plotted in Fig.6-6. This shows that the magnitude of the current along dislocations in high forward bias increases with temperature. This behavior is not surprising since the number of holes activating to the DL states will be lower at lower temperatures leading to a lower current.

Comparing Eqn.6-4 with Eqn.4-12 one might see an apparent inconsistency in temperature dependence of J_{d1}. However, when one realizes that the constant B in Eqn.4-12 has a term which is exponentially dependent on T, in addition to other terms, and that the $\exp(qV_o/kT)$ term alone does not determine the temperature behavior of J_{d1} this apparent inconsistency is removed.

The mechanism via which the carriers are conducted along the dislocations is also of importance. Thermally activated hopping along the dislocation states or tunneling from one occupied state to the next unoccupied state or a combination thereof could give rise to a d.c. conductivity. Presumably, the barrier between two states does not depend on the temperature. Hence it is quite likely that the tunnel current along the line defect is not very sensitive to temperature. However if the conduction arises predominantly due to hopping one would expect a larger temperature sensitivity. Experimentally J_{DL} is observed to be

temperature dependent. If we assume the carrier density is constant this would suggest that the carrier transport along dislocation states is predominantly due to hopping conduction.

6.3 Sensitivity of MIS to humidity

In the course of observations it was found that the reverse current of the MIS cells respond to the variation of humidity. More interestingly, it was observed that the response depends, and in fact, increases with the damage in the cells almost by an order of magnitude. Fig.6-7 shows the reverse current of a series of cells subjected to a sequence of evacuating the air in the sample holder and then exposing the sample to room air where the reverse bias was held constant at - 4.0 V. Introduction of dry Ar or N_2 did not produce any such variation. Moreover, a thermocouple kept in contact with the sample did not show any significant decrease of temperature when the system was pumped out by a rotary pump. Hence, it can be concluded that the shown variations are in fact due to the presence or absence of moisture.

Fig.6-8 shows the the response obtained by a 1 μm damaged sample kept in a rig used for measuring the response of gas sensors with a flow of N_2 bubbled through water to vary the humidity inside the chamber. The relative humidity, RH% at each measurement was measured separately using a digital hygrometer (Cole Palmer 3309-50).

Conventional humidity sensors have

humidity absorbing dielectrics which yield a good variation of the capacitance or conductance of the structure[132]. However, in the case of damaged samples the improved response indicate a mechanism that involves dislocations as well. Temporary reversible passivation by protons could give rise to such a behavior as indicated by the illuminated characteristics for four cycles of exposing and removing moisture from the chamber although other[133] explanations are also quite possible. This result is analogous, although very much at a lower scale, to what was observed in hydrogen passivation studies (see Fig.5-8).

6.4 Passivation in the presence of CO

Another interesting observation made during the experimentation was that if CO was used instead of H_2, the improvements obtained in passivating the damaged MIS cells were almost identical to those from H_2 passivation (see section 5.2).

Since CO alone cannot saturate the dangling bonds in the dislocations (due to its relatively large molecular size), this apparent passivation by CO can be brought about by the production of H_2 via the chemical reaction of CO with moisture as,

$$CO + H_2O = CO_2 + H_2.$$

To establish this mechanism, an attempt was made to remove moisture from the quartz tube by baking it at 525°C for one hour while pumping. A liquid nitrogen cold trap also was incorporated into the passivation apparatus. However,

this did not produce any noticeable effect on the results.

This indcates either, water is not completely removed from the walls of the quartz tube or, the oxidation takes place predominantly on the sample surface itself, where the native oxide (SiO_2) is known to be hygroscopic. Further studies have to be made to establish a satisfactory mechanism for the observations.

6.5 Conclusions

To conclude, we have shown that the silicon MIS (Al-SiO_2-pSi) solar cells with a carefully prepared thin insulator (< 20 A) layer have a similar temperature dependence as the conventional n^+p junction cells in the range 100 - 300 K. This supports the claim[61,84] that the above two classes of structures are electronically equivalent. By analysing the temperature variation of current-voltage characteristics of damaged samples it is shown that the current along dislocations at high forward voltages increase with temperature.

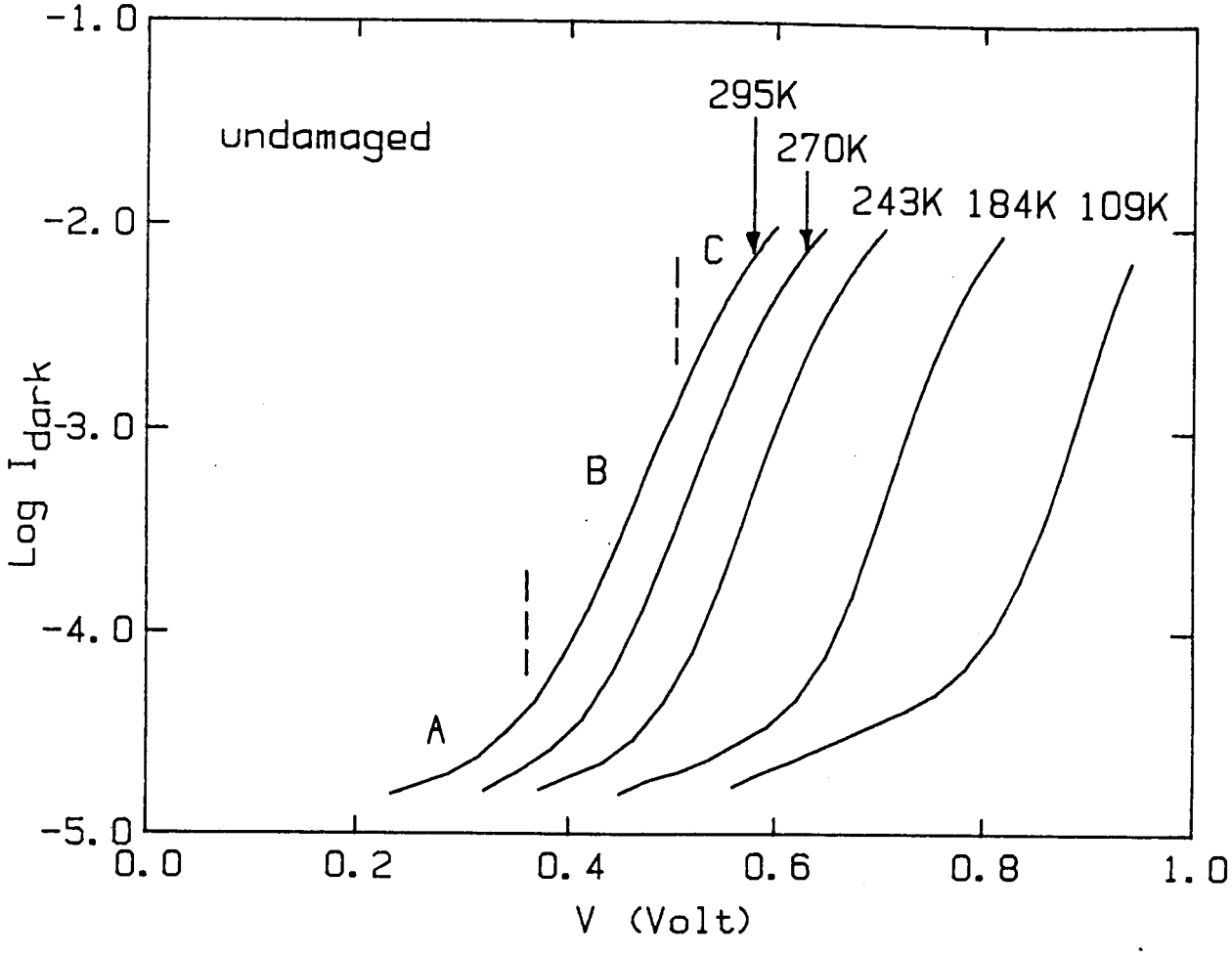

Fig.6-1 The dark current-voltage curves of an MIS cell (P100) at different temperatures. Three distinct regions (A,B and C) are indicated for this undamaged cell at 295 K.

TABLE 6-2

Cell type	a_{Voc} 10^{-3} V K^{-1}	a_{Jsc} 10^{-5} Acm^{-2} K^{-1}	a_{FF} [b] 10^{-4} K^{-1}	a_{η} [b] 10^{-2} % K^{-1}
n-p Si [a]	-2.2	1.3	-8	-4
MIS [c]	-(2.03 ± 0.18)	(1.1 ± 0.1)	-(7 ± 2)	-(1.0 ± 0.2)

a) From Ref.125: for cells with similar base resistivity, and at same illumination intensity as present work.

b) For room temperature region.

c) Al-SiO_x-pSi cells: effective area 0.376 cm^2.

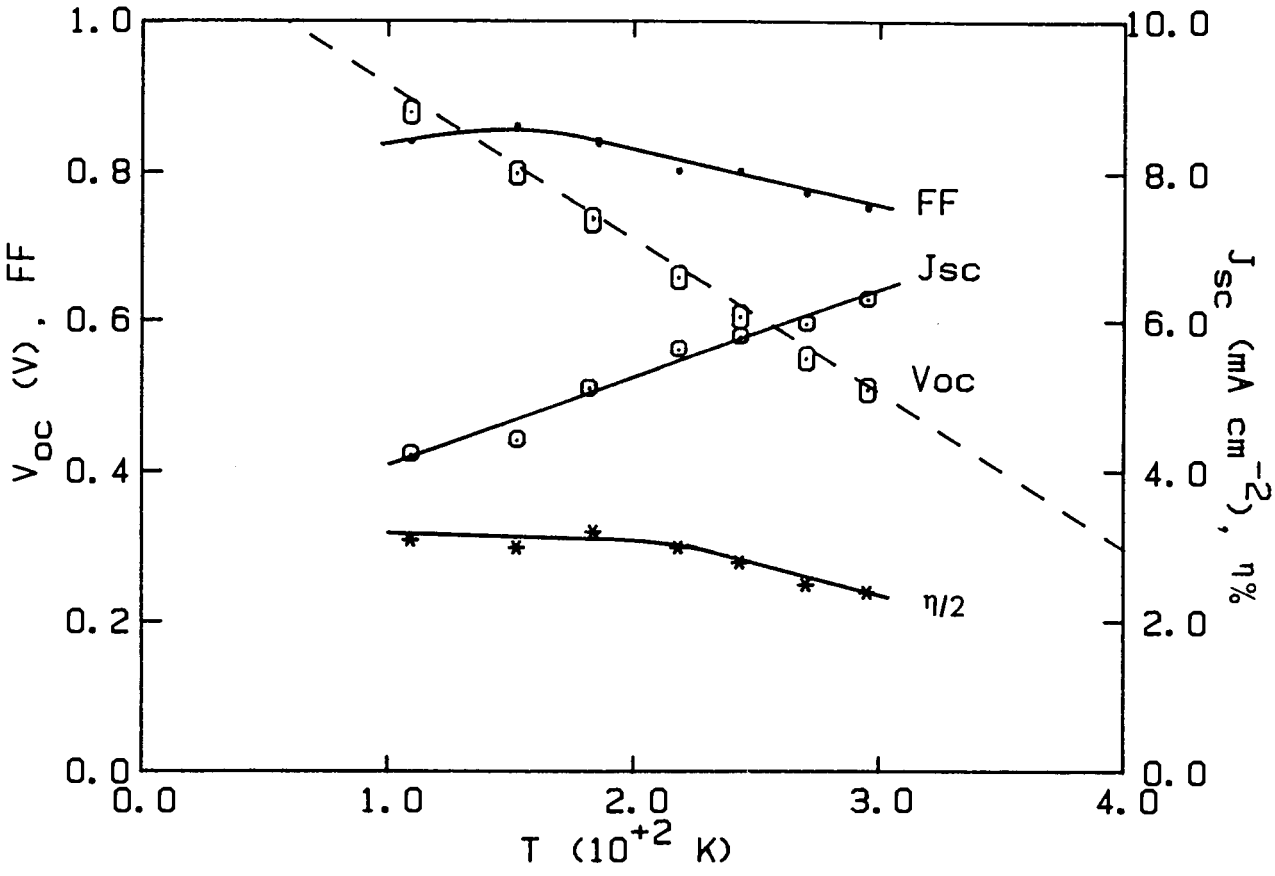

Fig.6-2 The variation of the open circuit voltage Voc, the short circuit current Jsc, the fill factor FF, and the efficiency η of an umdamaged MIS solar cell with temperature.

The dashed line is calculated using,

$$V_{oc} = n(kT/q)\ \ln(J_{sc}/J_o).$$

TABLE 6-1

T	n [a]	J_o [a]	J_{SC}	V_{OC}
K		A cm^{-2}	mA cm^{-2}	mV
295	1.22	3.4×10^{-10}	6.3	508
270	1.20	1.1×10^{-11}	6.0	550
243	1.22	1.8×10^{-13}	5.6	606
184	1.46	6.1×10^{-17}	5.8	736
109	2.59	3.9×10^{-19}	4.2	881

a) These parameters are obtained from dark J(V) after correcting for the series resistance as $J(V) - IR_s$.

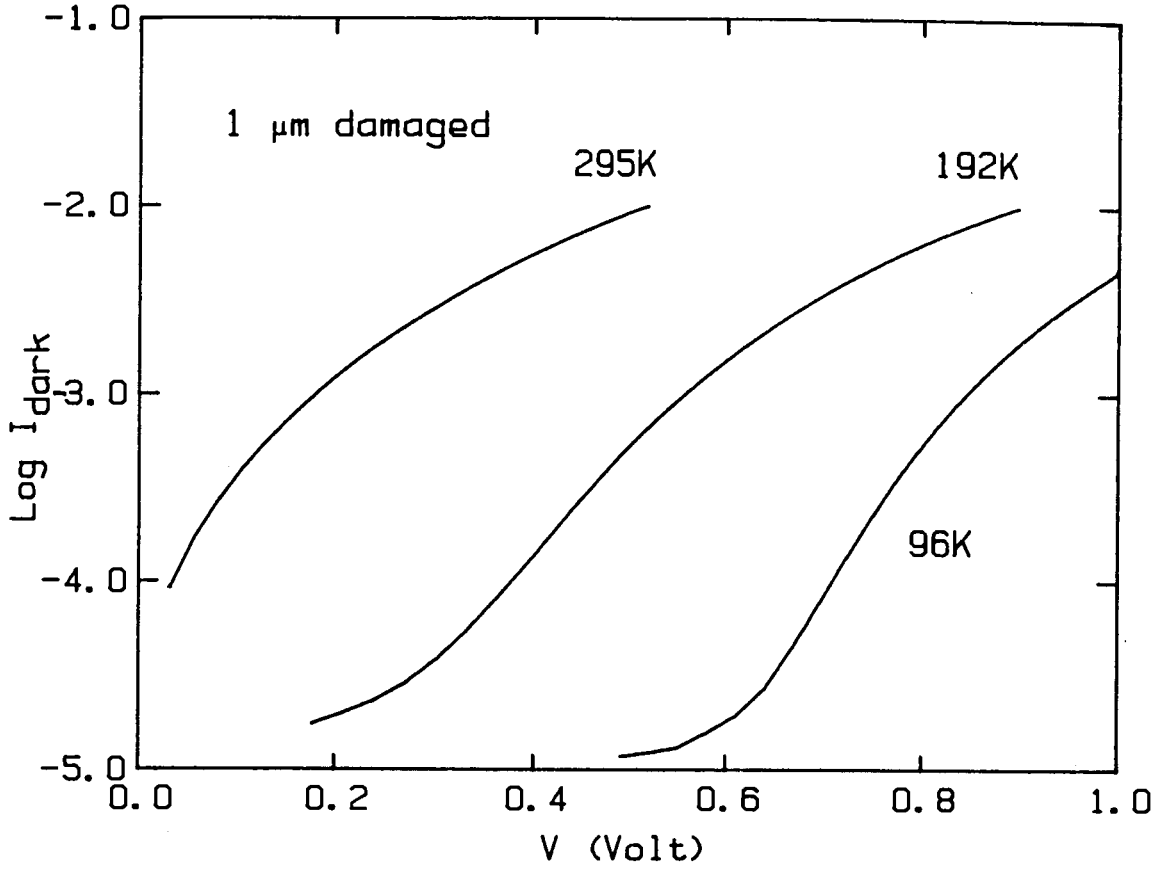

Fig.6-3 The dark current-voltage curves of a 1 μm damaged MIS cell (P111A) at different temperatures.

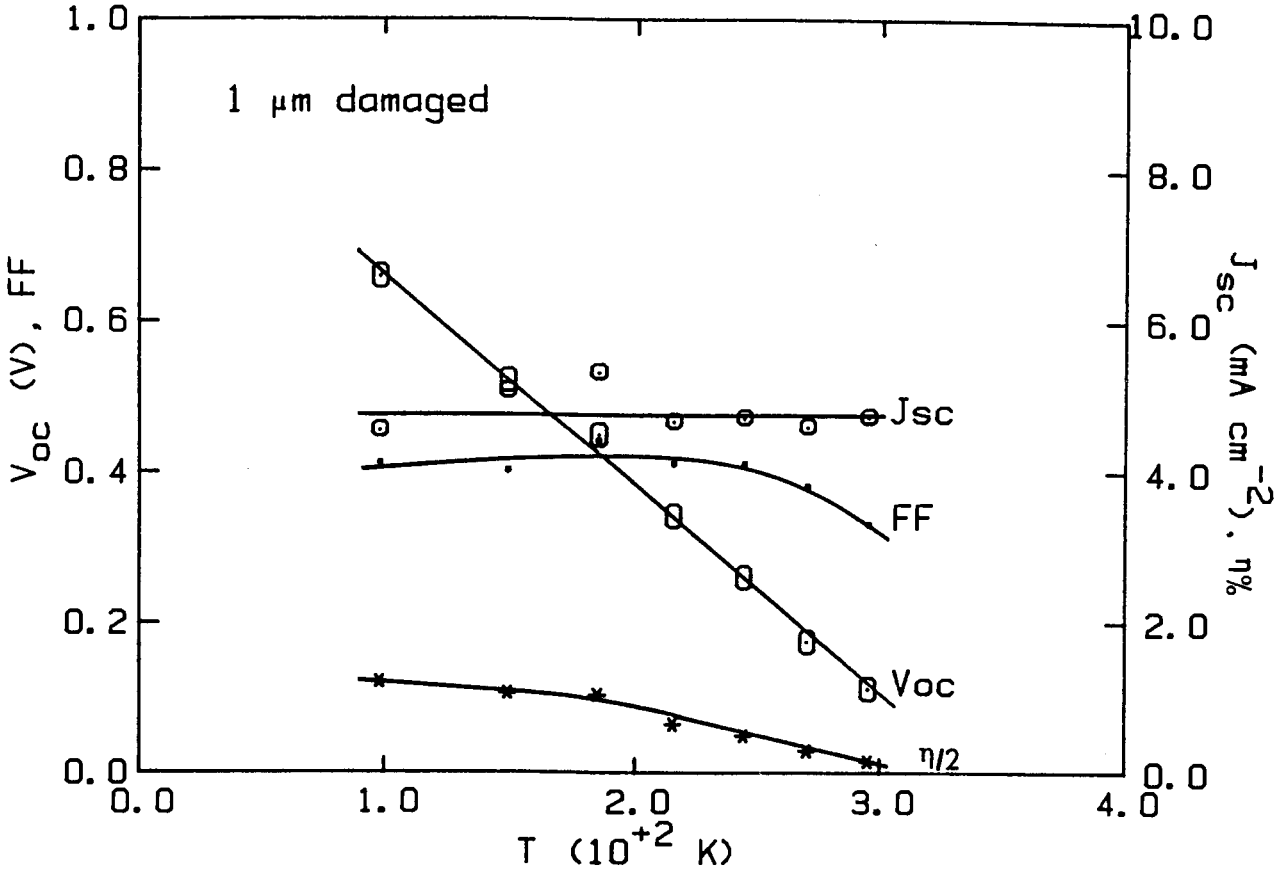

Fig.6-4 The variation of the open circuit voltage Voc, the short circuit current Jsc, the fill factor FF, and the efficiency η of a 1 μm damaged MIS solar cell with temperature.

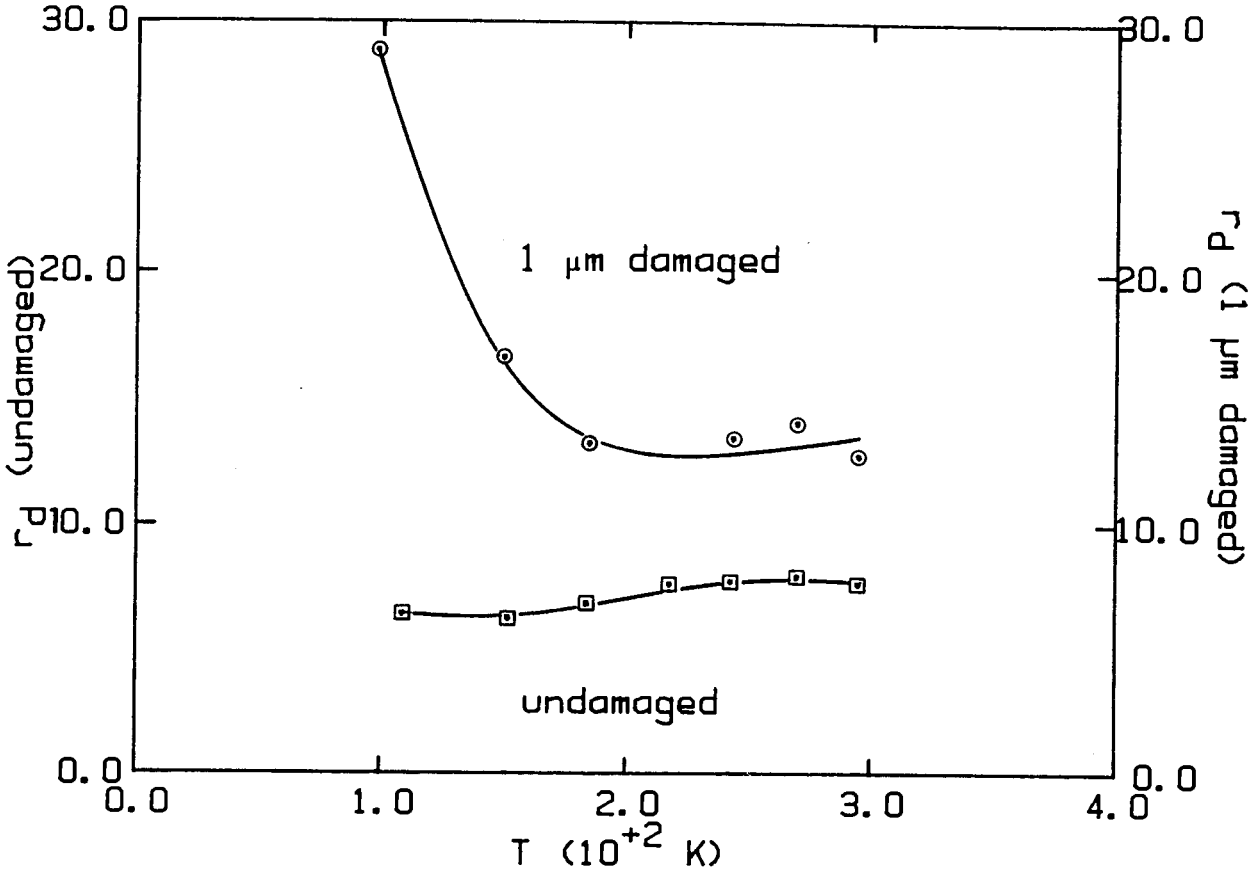

Fig.6-5 The temperature variation of the differential resistance, r_d of an undamaged and a damaged MIS cells.

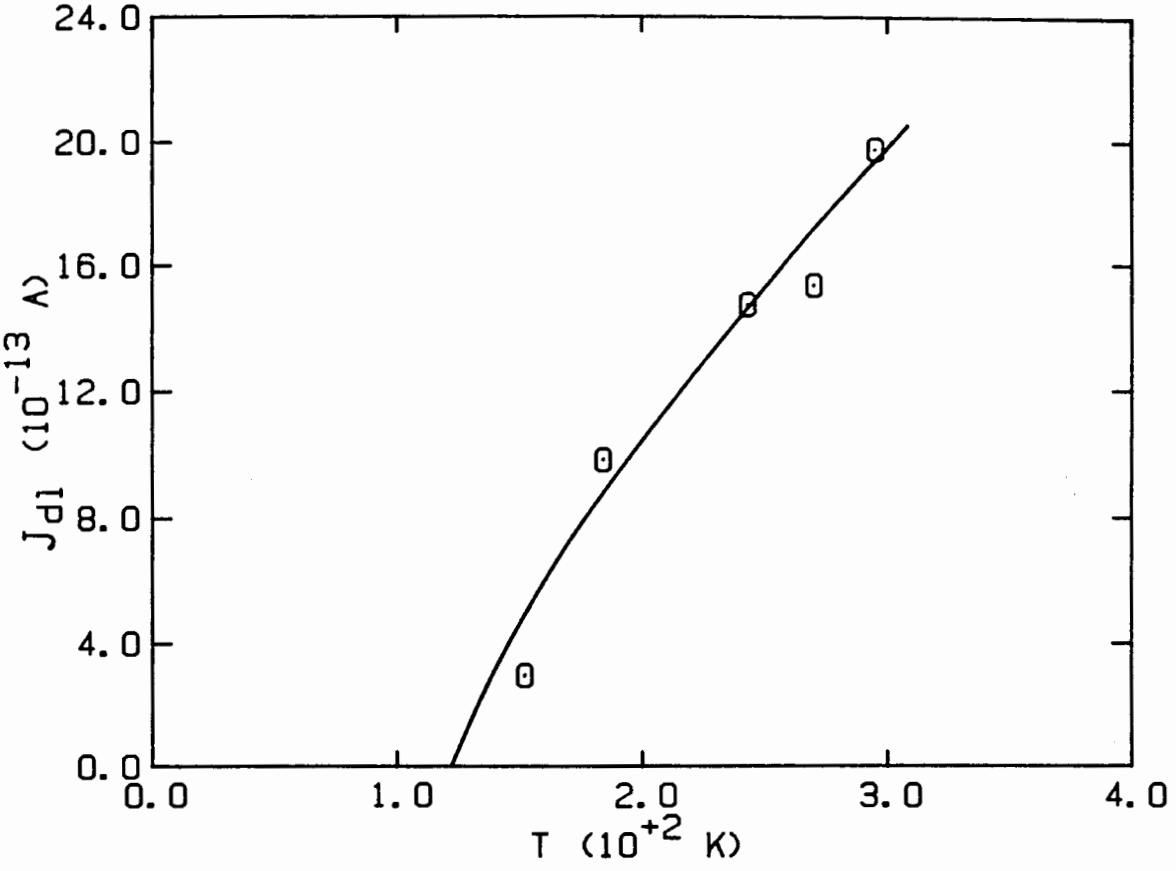

Fig.6-6 The calculated variation of the current along a dislocation at V$\gg$Voc, with temperature.

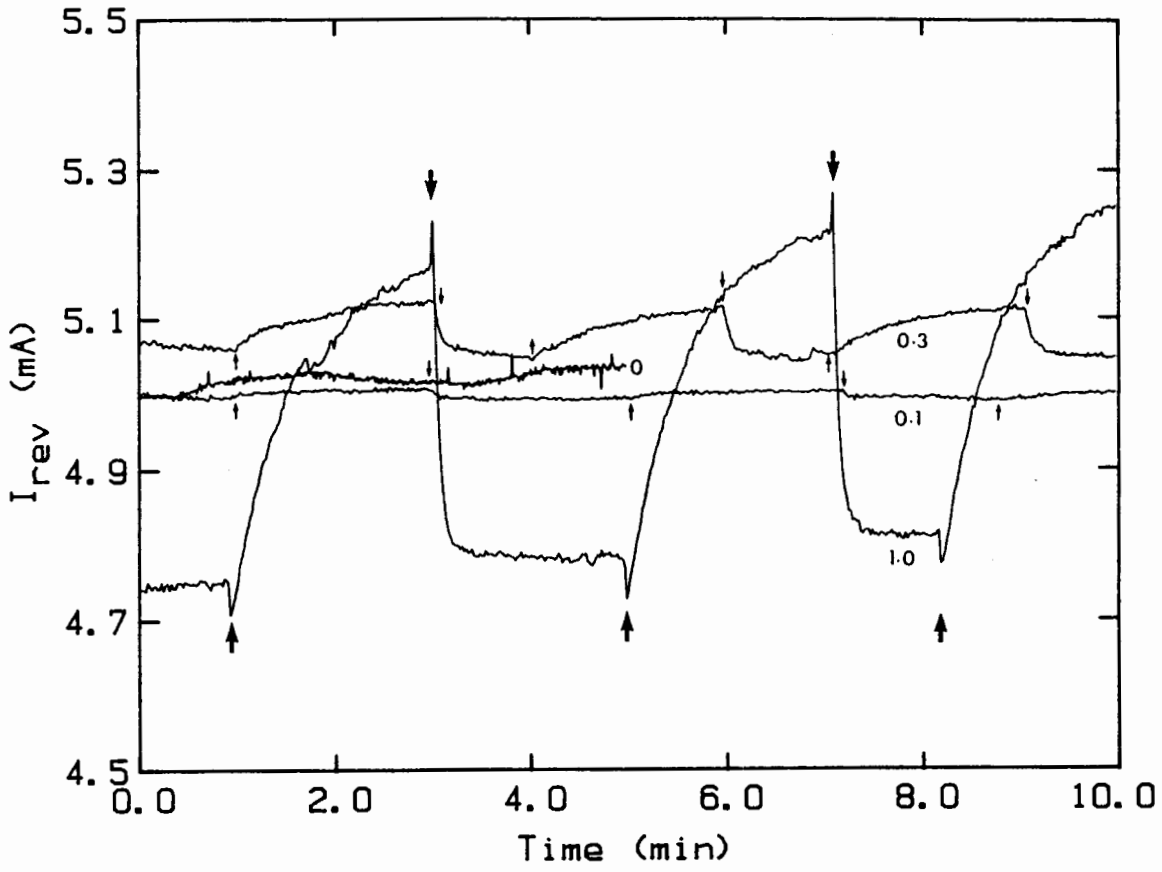

Fig.6-7 The variation of the reverse current of undamaged and damaged cells at a constant bias (at -4.00 V) for a series of exposures to room air (R_H = 13%) after evacuating the sample container.

The depth of damage in each sample is indicated in μm below the curve. The arrows pointing up (↑) indicate the starting time of evacuation of the container and the arrows pointing down (↓) indicate the exposure of the sample to room air. All the curves except that of 1 μm have been offset by various amounts along Irev axis to show them in one scale.

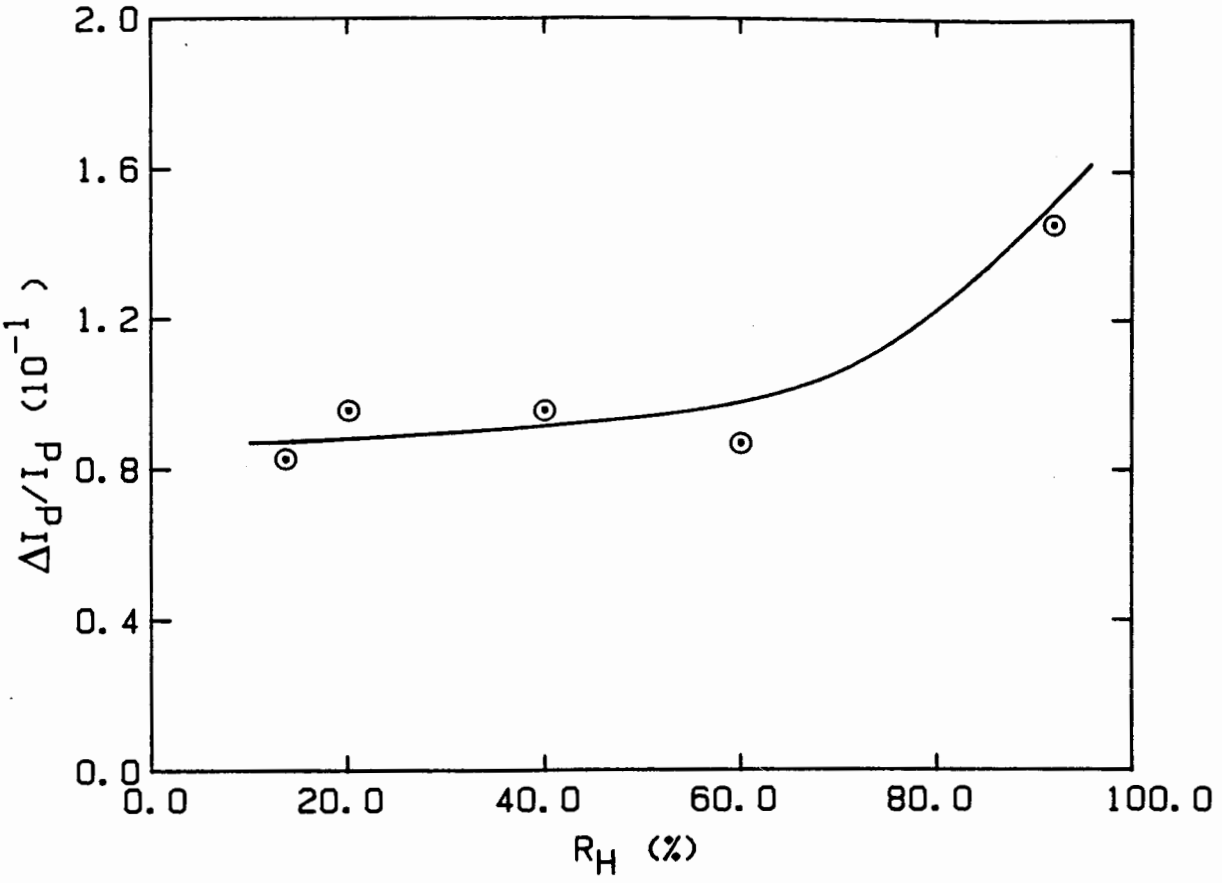

Fig.6-8 The response (the change in the reverse dark current) of a 1 μm damaged sample vs. the relative humidity, R_H.
Air was bubbled through water to change the R_H inside the container.

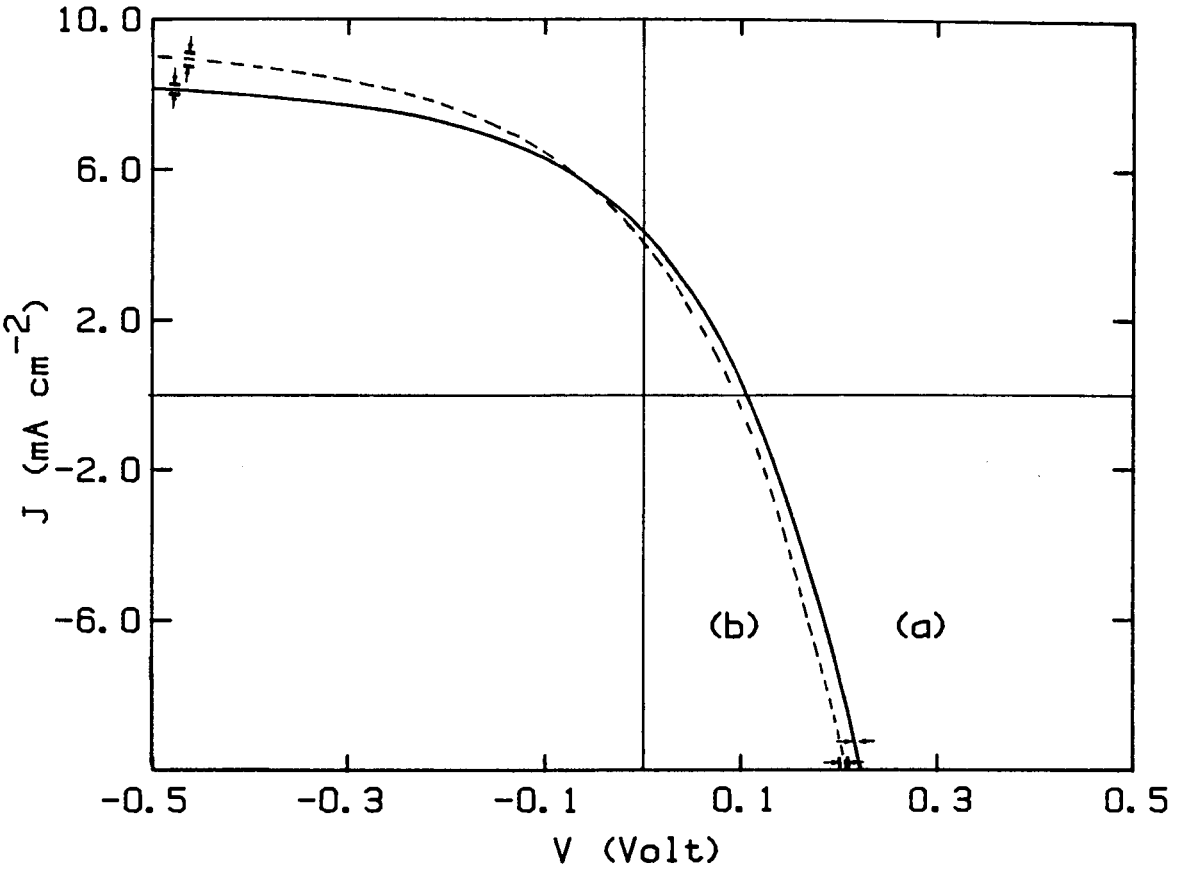

Fig.6-9 The illuminated J-V curves of a 1 μm damaged sample that has undergone several cycles of evacuation and exposure to room air.

(a) At equilibrium with room air (exposed - wet)

(b) Under vacuum (30 milli Torr - dry)

The arrows indicate the variation of the curves obtained at the end of each cycle.

CHAPTER VII

CONCLUSIONS

The experimental results obtained in this thesis suggest the possibility of a d.c. conductivity along dislocations in addition to simple recombination of carriers at them.

A model that accounts for the effect of the dislocation space charge region in carrier capture at the defects was developed assuming captured carriers can be conducted along the line defects. The model successfully explains the current-voltage data we have observed for the damaged MIS cells whereas the assumption of recombination at the defects alone is shown to be inadequate for clarifying the data. Furthermore, the parallel photoelectrochemical measurements carried out elsewhere on our samples, where it was found that holes were injected into the dislocation levels by ferricyanide ions in solution lend strong support to the hypothesis of carrier conduction along dislocations. In view of the above evidence it is concluded that there is a d.c. conductivity associated with dislocations in Si. From comparison of theory and experiment we estimate that their specific conductance (i.e., resistance per unit length) to be in the order of 10^{-15} cm ohm^{-1}. This value is very low, but high enough to be an effective "shunt" across a junction. The dislocation current was shown to vary exponentially with the applied voltage which makes it experimentally difficult to isolate it from the well known

recombination current that has a very similar dependence.

Passivation of dislocations by atomic hydrogen was measured and shown, generally, to improve the characteristics of the damaged MIS cells. From the model it could be concluded that passivation causes a lowering of either the density of recombination centers or the d.c. conductivity of the dislocations, and probably both. However, it was not possible to separate the specific contributions of the two variables due to the complications introduced by acceptor neutralization.

The undamaged MIS ($Al-SiO_x-pSi$) cells were shown to be very similar to corresponding n^+p junction cells in studies of the temperature dependence of the solar cell parameters in the range of 100 to 300 K. The effect of temperature on the damaged cells were also studied. These allowed one to obtain the temperature dependence of the current along dislocations. The variation observed seems to suggest a hopping mechanism but further studies are necessary to clarify the true mechanism of the observed dislocation conductivity.

APPENDIX I

A1. The photocurrent calculated by SNS theory

As shown in Fig. A1 the semiconductor in the MIS diode can be considered to have two different regions characterized by two different minority carrier life times (and two corresponding diffusion lengths) when mechanical damage is present. The life times (and diffusion lengths) are denoted by t_d (L_d) and t_o (L_o) for the damaged and the undamaged regions, respectively. The above life times are related to the diffusion lengths by

$$L_{d,o} = (D_n t_{d,o})^{1/2} \qquad (A1)$$

where D_n is the minority carrier diffusion coefficient. Since the mobilities of the two regions are not significantly different from each other at room temperature one can use the same D_n for both cases. For simplicity of calculations emphasizing the effect of recombination on photocurrent the MIS structure is represented as a one-sided-barrier. The insulator is assumed to be thin enough such that it pose no significant hindrance to carrier flow. The effect of the surface states is also ignored. The estimated value of the surface recombination current J_s according to Eqn.2-4 is in the order of 10^{-13} A cm^{-2} with a high density of surface states, $N_t = 10^{13}$ cm^{-2}. Since the presence of the oxide layer will tend to reduce the density of surface states their contribution to the recombination current can be neglected as well.

The current under illumination is conveniently

separated into several components, namely, the current due to a) the photogenerated minority carriers (electrons) diffusing from the bulk (or quasi-neutral region) (J_{nd}), b) the photogenerated carriers (J^{p}_{SCR}) in the space charge region, and c) the thermally generated carriers (J^{t}_{SCR}) in the SCR. It is assumed, as usual, that all the minority carrier diffusing through the quasi-neutral region to the edge of the SCR are swept away by the electric field present. Then the total photocurrent density J_{ph} can be written as

$$J_{ph} = J_{nd} + J^{p}_{SCR} + J^{t}_{SCR} \qquad (A2).$$

The SCR photogeneration current is simply given by

$$J^{p}_{SCR} = qGW_{SCR} \qquad (A3)$$

where W_{SCR} is the width of the space charge region and G is the photogeneration rate which is assumed to be a constant for simplicity. The SCR thermal generation current is given by the SNS theory[82] as

$$J^{t}_{SCR} = qn_i W_{SCR}/2t_d \qquad (A4)$$

where n_i is the intrinsic carrier density of Si at room temperature, and W_{SCR} is given by

$$W_{SCR} = ((2\epsilon_s/qN_A)(V_{bi} - V))^{1/2} \qquad (A5)$$

which is the same as the Eqn.2-18.

The diffusion component J_{nd} can be calculated by solving the current equation and the minority carrier continuity equation in one dimension[85] as follows.

Current equation:

$$J_{nd} = qD_n(dn/dx) \qquad (A6)$$

Continuity equation:

$$(1/q)(dJ_{nd}/dx) + G - U = 0 \qquad (A7)$$

where U is the carrier recombination rate, which can be expressed as

$$U = (n - n_o)/t \qquad (A8)$$

using an appropriate minority carrier life time t.
In (A8) n is the density of electrons in the sample under illumination and n_o is that at thermal equilibrium.
$t = t_o$ in the bulk ($x < -\ell$) and $t = t_d$ in the damaged region ($-\ell < x < -W_{SCR}$).

The second-order differential equation resulting from combining (A6) with (A7) is solved subject to the following boundary conditions: considering the two regions a) $x < -\ell$ and b) $-\ell < x < -W_{SCR}$.

I. $n(x)$ is continuous across $x = -\ell$.

II. $J_{nd}(x)$ is continuous across $x = -\ell$.

III. $n(x = -W_{SCR}) = n_o(x = -W_{SCR}) \exp(qV/kT)$.

The third condition is the one corresponding to the standard low-injection assumption which is valid even under AMO illumination.

After some algebraic manipulations one obtains

$$J_{nd} = (qD_n/L_d)\ (F1 - F2F3)\ /\ F4 \qquad (A9)$$

where

$F1 = G(t_o - t_d)L_d$

$F2 = n_o(\exp(qV/kT) - 1) - Gt_d$

$F3 = L_d\cosh y - L_d\sinh y$

$F4 = L_o\cosh y - L_o\sinh y$ and

$y = (\ell - W_{SCR})/L_d$.

It is to be noted that by changing the parameters appropriately in (A9) one can recover the conventional expression for one-sided-junction[85]. Setting $\ell = -W_{SCR}$, $t_o = t_d = t$ and $L_o = L_d = L$ in (A9) results

$$J_{nd} = qL_oG - J_o(\exp(qV/kT - 1) \qquad \text{(A10)}$$

where $J_o = (qD_n/L)$.

The total photocurrent of the damaged cell is then given by (A2) with (A9), (A3) and (A4), and the photocurrent of an undamaged cell is obtained using (A10) instead of (A9). t_d was found to be 2.6×10^{-11} s by fitting Eqn.(A4), which describes the generation current due to the defect levels, to dark J-V data of 1 um damaged sample.

Following parameters were used in the calculations shown in Fig. 4-9:

ℓ = 1 μm

L_o = 100 μm

V_{bi} = 0.85 eV[87]

G = 8.1×10^{18} s^{-1} cm^{-3} (for J_{ph} = 13 mA cm^{-2})

D_n = 33.8 cm s^{-2} and

$N_A = 3 \times 10^{15}$ cm^{-3}.

The above calculation is for a constant volume rate of electron-hole pair generation, G (cm^{-3} s^{-1}) and it is given by $J_{ph} = qGL_o$. If the quantum efficiency is assumed to be unity, $J_{ph} = qN_{ph}$ where N_{ph} ($2 \times 10^{17} cm^{-2}$ s^{-1}) is the usable photon flux per second ($E > E_g$) in AM2 illumination. Then we have $GL_o = N_{ph}$ which is roughly the case for the above value of G.

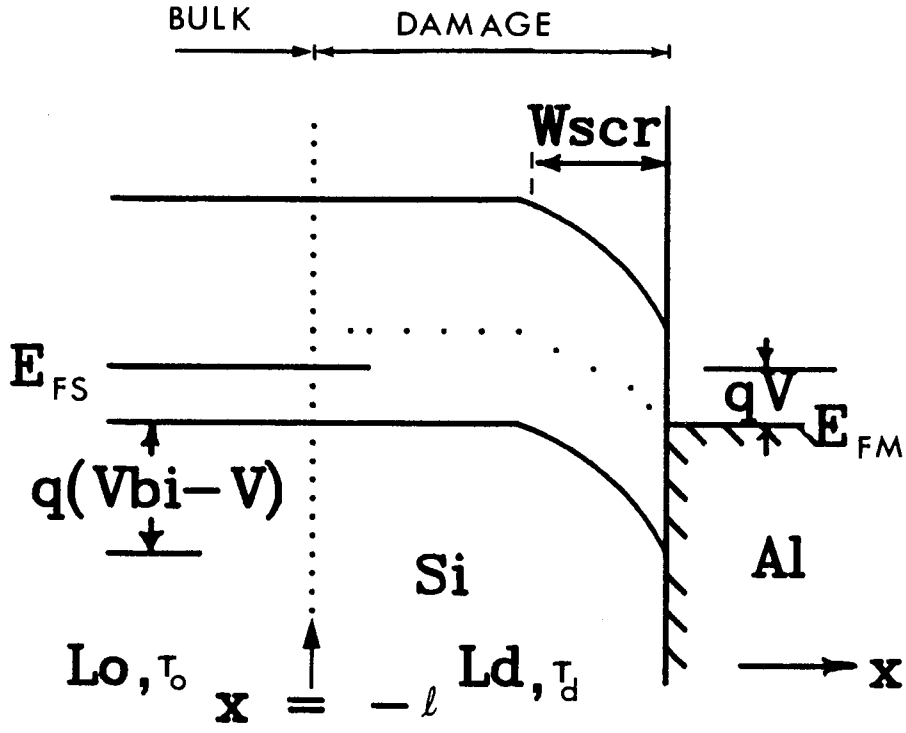

Fig.A-1 The band diagram of the MIS cell in one-sided-junction approximation. The damaged region extending a length ℓ from the surface can be characterized by a minority carrier life time τ_d while that of the undisturbed bulk material beyond ℓ, is τ_o ($\tau_d << \tau_o$). The case where $\ell > W_{scr}$, the width of the space charge region, is considered.

BIBLIOGRAHPY

1. D. Hull, *Introduction to Dislocations*, Pergamon Press, p.12 (1965).

2. G.I. Taylor, Proc. Roy. Soc., A145, 362 (1934).

3. E. Orowan, Z. Phys. 89, 614 (1934).

4. G. Polanyi, Z. Phys. 89, 660 (1934)

5. W. Hayden, W.G. Moffatt and J. Wulf, *Structure and Properties of Materials*, Vol. III, Mechanical Behavior, John Willey and Sons Inc, New York, (1965).

6. N.W. Ashcroft and N.D. Mermin, *Solid State Physics*, Sanders College, Philadelphia, p.634 (1976).

7. W.T. Read, *Dislocations in Crystals*, McGraw Hill Book Co. Inc. New York, p.32 (1953).

8. B. Mutaftschiev, in *Dislocations in Solids*, V.5, F.R.N. Nabarro (Ed), North Holland Pub. Co. Amsterdam, (1980).

9. W.E. Dash, J. Appl. Phys. 27, 1193 (1956).

10. W. Shockley, Phys. Rev. 91, 228 (1953).

11. L. Pauling, *The Nature of the Chemical Bond*, Cornell University Press, (1960).

12. J.M. Fairchild and G.H. Schwutte, J. Electrochem. Soc, 113, 1229 (1966).

13. R. Labusch, Physica, 117B, 203 (1983).

14. S.R. Morrison, J. Electron. Mat. 11, 21 (1982).

15. R. Nitecki and B. Pohoryles, Appl. Phys. A36, 55 (1985).

16. W.T. Read, Phil. Mag. 45, 775 (1954).

17. W.T. Read, Phil. Mag. 45, 1119 (1954).

18. W.T. Read, Phil. Mag. 46, 111 (1955).

19. R.H. Glaenzer and A.G. Jordan, Solid State Electron. 12, 247 (1969).

20. H.F. Matare and C.W. Laakso, J. Appl. Phys. 40, 476 (1969).

21. W. Shockley and W.T. Read, Phys. Rev. 87, 835 (1952).

22. R.N. Hall, Phys. Rev. 87, 387 (1952).

23. S.R. Morrison, Phys. Rev. 99, 1904 (1955).

24. S.R. Morrison, Phys. Rev. 104, 619 (1956).

25. K.K. Yu, A.G. Jordan and R.L. Longini, J. Appl. Phys. 38, 572 (1967).

26. T. Figelski, Solid State Electron. 569,1403 (1978).

27. S. Milshtein and A. Senderishin, Phys. Stat. Sol. (b). 109, 429 (1982).

28. W. Schroter and R. Labusch, Phys. Stat. Sol. 36, 539 (1969).

29. R. Labusch and W. Schroter, in *Dislocations in Solids*, V.5, F.R.N. Nabarro (Ed), North Holland Pub. Co. Amsterdam, p. 127 (1980).

30. A. Ourmazd, Contemp. Phys. 25, 251 (1980).

31. W. Schroter, Phys. Stat. Sol. 31, 177 (1969).

32. V.A. Grazhulis, V.V. Kveder and V. Yu. Mukhina, Phys. Stat. Sol. (a). 43, 407 (1977).

33. V.A. Grazhulis, V.V. Kveder and V. Yu. Mukhina, Phys. Stat. Sol. (a). 44, 107 (1977).

34. V.A. Grazhulis, V.V. Kveder, V. Yu. Mukhina and Yu. A. Osip'yan, JETP Lett., 24, 142 (1976).

35. Yu. A. Osip'yan, J. Phys. (Paris). C4, 103 (1983).

36. C. Elbaum, Phys. Rev. Lett. 32, 376 (1974).

37. S. Mantovani and U.D. Pennino, Phys. Stat. Sol. (a). 30, 747 (1975).

38. S.R. Morrison and B.H. Loo (unpublished).

39. W.M. Sears, J. Appl. Phys. 57, 2051 (1985).

40. B.K. Miremadi and S.R. Morrison, J. Appl. Phys. 55, 3658 (1984).

41. C.H. Seager and T.G. Castner, J. Appl. Phys. 49, 3879 (1978).

42. M. Taniguchi, M. Hirosi, Y. Osaka, S. Hasegawa and T. Shimizu, Japan. J. Appl. Phys. 19, 665 (1980).

43. B. Read, O.A. Weinreich and H.F. Matare, Phys. Rev. 113, 454 (1959).

44. R.K. Mueller and K.N. Maffitt, J. Appl. Phys. 35, 734 (1965).

45. H.F. Matare, J. Appl. Phys. 56, 2605 (1984).

46. H.F. Matare, J. Appl. Phys. 59, 97 (1986).

47. A.D. Kurtz, S.A. Kulin and B.L. Averbach, Phys. Rev. 101, 1285 (1956).

48. G.K. Wertheim and G.L. Pearson, Phys. Rev. 107, 694 (1957).

49. R.J. Rodel, A.R. von Neida, R. Caruso and L.R. Dawson, *Extended Abstracts*, Electrochemical Society, Princeton, New Jersey, 77-2, 857 (1977).

50. M. Lax, J. Appl. Phys. 4, 2796 (1978).

51. G.R. Booker, A. Ourmazd and D.B. Darby, J. Phys. (Paris). C6, 19 (1979).

52. M. Yamaguchi and C. Amano, J. Appl. Phys. 58, 3601 (1985).

53. M. Yamaguchi, A. Yamamoto and Y. Itoh, J. Appl. Phys. 59, 1751 (1986).

54. A. G. Chynoweth and G.L. Pearson, J. Appl. Phys. 29, 1103 (1958).

55. A. Goetzberger and R.H. Finch, Solid State Electron. 7, 543 (1964).

56. M.V. Whelan, Solid State Electron. 12, 963 (1969).

57. L.E. Murr and O.T. Inal, in *Solar Material Science*, L.E. Murr (Ed), Academic Press, New York, p. 53, (1980).

58. J.E. Lawrence, J. Electrochem. Soc. 115, 860 (1968).

59. D.B. Holt, J. Phys. (Pars). C6, 189 (1979).

60. S.R. Morrison, in *Grain Boundaries in Semiconductors*, Elsevier Science Pub. Co. Inc. G.E. Pike, C.H. Seager (Eds), p.193 (1982).

61. M.A. Green, F.D. King and J. Shewchun, Solid State Electron. 17, 551 (1974).

62. J. Shewchun, M.A. Green and F.D. King, Solid State Electron. 17, 563 (1974).

63. D.L. Pulfrey, IEEE Trans. Electron. Devices. ED-25, 1308 (1978).

64. H.C. Card, Solid State Electron. 20, 971 (1977).

65. M.A. Green and J. Shewchun, Solid State Electron. 17, 349 (1974).

66. O. Engstrom and A. Carllon-Gylemo, IEEE Trans. Electron. Devices. ED-32, 2438 (1985).

67. T.Y. Yamamoto, K. Kawamura and H. Shimizu, Solid State Electron, 19, 701 (1976).

68. P.F. Ruths, S. Ahsok, S.J. Fonash and J.M. Ruths, IEEE Trans. Electron Devices. ED-28, 1003 (1981).

69. K. Dobos, M. Armgarth, G. Zimmer and I. Lundstrom, IEEE Trans. Electron Devices. ED-31, 508 (1984).

70. M.A. Green and R.B. Godfrey, Appl. Phys. Lett. 29, 610 (1976).

71. L.B. Freeman and W.E. Dahlke, Solid State Electron, 13, 1483 (1970).

72. P. Viktorovitch and G. Kamarinos, J. Appl. Phys. 48, 3060 (1977).

73. M.A. Green, Appl. Phys. Lett. 33, 178 (1978).

74. D.L. Pulfrey, IEEE Trans. Electron Devices. ED-25, 587 (1976).

75. C.M. Klimpe and P.T. Landsberg, Solid State Electron. 21, 1539 (1978).

76. R. Childs, F. Fortuna, J. Geneczko and S.J. Fonash, in Proceedings of 13th Photovoltaic Specialists Conference, Luxembourg, p.862 (1977).

77. N.G. Tarr, D.L. Pulfrey and P.A. Illes, Appl. Phys. Lett. 35, 258 (1979).

78. K.K. Ng and H.C. Card, IEEE Trans. Electron Devices. ED-27, 716 (1980).

79. S.A. Asimov, D.A. Aronov, D.K. Isamukhamedova and Yu.M. Yuabov, Phys. Stat. Sol. (a). 73, K1 79 (1982).

80. H.C. Card and E.H. hoderick, J. Phys. D. 4, 1589 (1971).

81. H.C. Card and E.H. hoderick, J. Phys. D. 4, 1602

(1971).

82. C.T. Sah, R.N. Noyce and W. Shockley, Proc. of IRE. 45, 1228 (1957).

83. R.B. Godfrey and M.A. Green, IEEE Trans. Electron Devices. ED-27, 4,737 (1980).

84. N.G. Tarr and D.L. Pulfrey, Solid State Electron. 22, 265 (1979).

85. S.M. Sze, *Physics of Semiconductor Devices*, John Wiley and Sons, N.Y. p.249 (1981).

86. S.R. Morrison, *Electrochemistry at Semiconductor and Oxidized Metal Electrodes*, Plenum Press, N.Y. p.127 (1980).

87. E.J. Charlson and J.C. Lien, J. Appl. Phys. 46, 3982 (1975).

88. Reference 85. p. 369.

89. S.R. Morrison, *The Chemical Physics of Surfaces*, Plenum Press, N.Y. p. 38 (1977).

90. R.A. Logan, G.L. Pearson and D.A. Kleinman, J. Appl. Phys. 30, 885 (1959).

91. P.F. Kane and G.B. Larrabee, *Characterization of Semiconductor materials*, McGraw Hill Book Co. Inc. New York, p.191 (1970).

92. Reference 1. p. 20.

93. E.N. Pugh and L.E. Samuels, J. Electrochem. Soc. 109, 409 (1962).

94. R. Stickler and G.R. Booker, Phil. Mag. 8, 859 (1963).

95. V.H. Gerischer, F. Hein, M. Lubke, E. Meyer, B. Pettinger and H.-R. Schoppel, Bunsen-Gesellschaft, 77 284 (1973).

96. C.E. Jones and A.R. Hitton, J. Electrochem. Soc. 112, 908 (1965).

97. A. Praet, F. Vanden Kerchove, W.P. Gomes and F. Cardon, Sol. Energy Mat. 7, 481 (1983).

98. Reference 1. pp. 27-28.

99. R.M.A. Azzam and N.M. Bashara, *Ellipsometry and Polarized Light*, North Holland Pub. Co. Amsterdam. (1977).

100.R.J. Archer, J. Optic. Soc. of Am. 52, 970 (1962).

101.L.C. Olsen, D.L. Barton, W. Miller, J.E. Garnier and R.P. Turcotte, J. Appl. Phys. 51, 6393 (1980).

102.C.H. Seager and D.S. Ginley, J. Appl. Phys. 52, 1050 (1981).

103.K.E. Bean, IEEE Trans. Electron Devices, ED-25, 1185 (1978).

104.Personal communication with B.K. Miremadi.

105.W.M.R. Divigalpitiya and S.R. Morrison, J. Appl. Phys. 60, 406 (1986).

106.H.B. Serreze, J.C. Swartz, G. Entine and K.V. Ravi, Mat. Res. Bull. 9, 1421 (1974).

107.D.G. Canfield and S.R. Morrison, Appl. Surf. Sci. 10, 493 (1982).

108.M.J. Madou, K.W. Freese and S.R. Morrison, J. Phys. Chem. 84, 3423 (1980).

109.A. Praet, G. Vercryuse, W.P. Gomes, W.M.R. Divigalpitiya and S.R. Morrison, Sol. Energy Mat. 14, 61 (1986).

110.J.I. Pankove, M.A. Lampert and M.L. Tang, Appl. Phys. Lett. 32, 439 (1978).

111.C.H. Seager and G.N. Ginley, Appl. Phys. Lett. 34, 337 (1979).

112.P.H. Robinson and R.V. D'Aiello, Appl. Phys. Lett. 39. 63 (1981).

113.J.I. Hanoka, C.H. Seager, D.J. Sharp and J.K.G. Panitz, Appl. Phys, Lett. 42, 618 (1983).

114.Y.S. Tsuo and R.B. Milstein, J. Appl. Phys. 57, 5523 (1985).

115.B. Pohoryles. Phys. Stat. Sol. (a). 67, K75 (1981).

116.B. Pohoryles. J. Phys. (Paris) Colloq. 44, C4-359 (1983).

117.H.J. Hovel, in proceedings of the 10th IEEE Photovoltaic Specialists Conference, Palo Alto, California, IEEE N.Y. p. 34 (1973).

118.N.M. Johnson, Phys. Rev. B. 31, 5525 (1985).

119.W.M.R. Divigalpitiya, S.R. Morrison, A. Praet, G. Vercryuse, and W.P. Gomes, Sol. Energy Mat. (in press) 15, (1987).

120.C.T. Sah, J.Y. Sun and J.T. Tzuo, Appl. Phys. Lett. 43, 204 (1983).

121.J.I. Pankove, D.E. Carlson, J.E. Berkeyheiser and R.D. Wance, Phys. Rev. Lett. 51, 2224 (1983).

122.M.L. Thewalt, E.C. Lightowlers and J.I. Pankove, Appl. Phys. Lett. 46, 689 (1985).

123.N.G. Tarr and D.L. Pulfrey, Appl. Phys. Lett. 34, 295 (1979).

124.J.Shewchun, R. Singh, D.Burk and F. Scholz, Appl. Phys. Lett. 35, 416 (1979).

125.H.J. Hovel, *Semiconductors and Semimetals*, Vol. 11, Academic Press, New York, p. 166 (1975).

126.S.M. Vernon and W.A. Anderson, Appl. Phys. Lett. 26, 707 (1975).

127.B.Bhaumik and R. Sharan, Appl. Phys. Lett. 29, 257 (1976).

128.H.W. Wolf, *Silicon Semiconductor Data*, Pergamon Press, pp. 24 - 26 (1969).

129.M.A. Green, A.W. Blakers and C.R. Osterwald, J. Appl. Phys. 58, 4402 (1985).

130.W.M.R. Divigalpitiya (submitted to Solar Cells).

131.T. Seiyama, N. Yamazoe and H. Arai, Sensors and Actuators, 4, 85 (1983).

132.L. Westcott and G. Rogers, J. Phys. E, 18, 572 (1985).

133.W. Shockley, W.W. Hooper, H.J. Queisser and W. Schroen, Surf. Sci. 2, 277 (1964).